Universiteit
Leiden
The Netherlands

Absorption, luminescence and scattering of single nano-objects

Yorulmaz, M.

Citation

Yorulmaz, M. (2013, June 26). *Absorption, luminescence and scattering of single nano-objects*. *Casimir PhD Series*. Retrieved from https://hdl.handle.net/1887/21018

Version:	Not Applicable (or Unknown)
License:	Licence agreement concerning inclusion of doctoral thesis in the Institutional Repository of the University of Leiden
Downloaded from:	https://hdl.handle.net/1887/21018

Note: To cite this publication please use the final published version (if applicable).

Cover Page

Universiteit Leiden

The handle http://hdl.handle.net/1887/21018 holds various files of this Leiden University dissertation

Author: Yorulmaz, Mustafa
Title: Absorption, luminescence, and scattering of single nano-objects
Issue Date: 2013-06-26

Absorption, Luminescence, and Scattering of Single Nano-Objects

Mustafa Yorulmaz

Absorption, Luminescence, and Scattering of Single Nano-Objects

PROEFSCHRIFT

ter verkrijging van
de graad van Doctor aan de Universiteit Leiden,
op gezag van Rector Magnificus prof. mr. C. J. J. M. Stolker,
volgens besluit van het College voor Promoties
te verdedigen op woensdag 26 juni 2013
klokke 15:00 uur

door

Mustafa Yorulmaz
geboren te Nevsehir, Turkije
op 26 augustus 1984

Promotor:	Prof. dr. M. A. G. J. Orrit	Universiteit Leiden
Co-promotor:	Dr. A. Gaiduk	Carl Zeiss Microscopy GmbH, Jena
Overige Leden:	Prof. dr. F. Cichos	Universität Leipzig
	Prof. dr. A. F. Koenderink	Universiteit van Amsterdam
	Prof. dr. E. R. Eliel	Universiteit Leiden
	Dr. M. P. van Exter	Universiteit Leiden
	Prof. dr. E. J. J. Groenen	Universiteit Leiden
	Dr. ir. S. J. T. van Noort	Universiteit Leiden

The work reported in this thesis was carried out at the 'Leids Instituut voor Onderzoek in de Natuurkunde' (LION). This work is a part of the research programme of the 'Stichting voor Fundamenteel Onderzoek der Materie' (FOM), which is financially supported by the Netherlands Organization for Scientific Research (NWO). We acknowledge financial support by the European Research Council (Advanced Grant SiMoSoMa).

An electronic version of this dissertation is available at the Leiden University Repository (https://openaccess.leidenuniv.nl).

Printed by: Proefschriftmaken.nl || Uitgeverij BOXPress

Casimir PhD series, Delft-Leiden 2013-17
ISBN: 978-90-8593-157-7

to Elif Sena, Çiğdem, and my parents

Contents

1 Introduction **1**
- 1.1 Single nano-objects . . . 1
- 1.2 Advantages of single nano-object studies . . . 2
- 1.3 Optical properties of single nano-objects . . . 4
- 1.4 Optical detection of single nano-objects . . . 7
  - 1.4.1 Correlation of absorption, luminescence and scattering 12
- 1.5 Plasmon resonance of a single gold nanorod near a dielectric interface . . . 12
- 1.6 Outline of this thesis . . . 14

2 Room-temperature detection of a single molecule's absorption by photothermal contrast **17**
- 2.1 Introduction . . . 18
- 2.2 Photothermal detection . . . 20
- 2.3 Optimizing the SNR in photothermal detection . . . 22
- 2.4 Experiment . . . 23
  - 2.4.1 Samples . . . 23
  - 2.4.2 Photothermal microscopy setup . . . 25
- 2.5 Characterization of photothermal detection sensitivity on gold nanoparticles . . . 27
  - 2.5.1 Minimum detectable dissipated power . . . 29
- 2.6 Detecting a single molecule by its absorption . . . 30
  - 2.6.1 Single BHQ1-10T-BHQ1 constructs . . . 30
  - 2.6.2 Single BHQ1-Amine molecules . . . 33
- 2.7 Conclusions . . . 33

3 Absorption, luminescence and sizing of organic dye nanoparticles **35**

3.1 Introduction 36
3.2 Experimental section 37
3.2.1 Combined photothermal and fluorescence microscopy 37
3.2.2 Atomic force microscopy 39
3.2.3 Organic nanoparticles preparation 40
3.2.4 Sample preparation for optical microscopy 40
3.3 Result and discussion 41
3.3.1 Optical microscopy of organic nanoparticles 41
3.3.2 Submonolayers and labyrinth structures formed by organic molecules 45
3.4 Conclusions 47

4 Correlated absorption and photoluminescence of single gold nanospheres 49
4.1 Introduction 50
4.2 Experimental section 51
4.2.1 Absorption (photothermal) and fluorescence microscopy 51
4.2.2 Atomic force microscopy (AFM) 52
4.2.3 Sample preparation 52
4.3 Results and discussion 53
4.3.1 AFM characterization of gold NPs 53
4.3.2 Correlation of AFM and optical microscopy results on gold NPs 54
4.3.3 Correlation of absorption and luminescence of individual gold NPs 55
4.3.4 Laser-induced enhancement of luminescence from gold nanospheres 60
4.4 Conclusions 65

5 Luminescence quantum yield of single gold nanorods 67
5.1 Introduction 68
5.2 Experimental 70
5.2.1 Sample preparation 70
5.2.2 Optical microscopy 71
5.3 Results and discussion 72
5.4 Conclusions 81

6 Influence of an approaching dielectric interface on the plasmon resonance of a gold nanorod **83**
6.1 Introduction 84
6.2 Methods and materials 87
6.2.1 Fluorescence spectroscopy and white-light interferences 87
6.2.2 Variable-distance cell 89
6.2.3 Samples 91
6.3 Results and discussions 92
6.3.1 Newton's rings and distance measurement 92
6.3.2 Plasmon resonance as a distance ruler 95
6.4 Conclusions 100

A The dissipated power for some common chromophores **103**

B Organic dye nanoparticles **107**

C Single gold nanospheres **115**

D Single gold nanorods **117**

Bibliography **129**

Summary **149**

Samenvatting **153**

Curriculum vitae **157**

List of publications **159**

Acknowledgements **161**

CHAPTER 1

Introduction

In this thesis, we study radiative (luminescence, scattering) and nonradiative (absorption) properties of single nano-objects, in particular single molecules, organic dye nanoparticles, and gold nanoparticles. We gain insight into the effect of physical structure and composition on the optical properties of a single nano-object by means of correlated absorption, luminescence, and scattering signals. In this introduction, we give a brief overview of single nano-objects, we describe their optical properties, and provide a short description of the methods for optical detection of individual nano-objects. We also discuss the advantages of studying single particles and point out the specific requirements and advantages of each detection method. At the end, we provide the contents of the following chapters of the thesis.

1.1 Single nano-objects

Nano-objects, with dimensions between atomic scale and bulk, include isolated molecules, semiconductor nanocrystals, organic dye nanoparticles, metal colloids, etc. They exhibit novel material properties that differ from bulk properties, e.g., the optical properties of nano-objects depend on their chemical structure, composition, size, shape, and local environment. A variety of nano-objects with tunable optical properties can be synthesized. In order to use nano-objects for their applications, it is of fundamental interest to understand how the optical properties change as functions of physical properties and local environmental conditions . After the optical properties

are characterized, nano-objects find novel scientific and technological applications. For example, organic nanoparticles have become building blocks of organic light-emitting diodes, thin-film transistors and photovoltaic solar energy collectors.[1,2] Semiconductor nanocrystals and single molecules serve as microscopic single-photon sources[3–5] and they pave the way for quantum information processing.[6–8] Gold nanoparticles provide very stable optical signals and they serve as contrast agents in microscopy.[9–12] They are also convenient tools for optical sensing[13–16], because their optical properties are very sensitive to changes in their local environment. Depending on the experimental conditions, they can be nontoxic and be used for biomedical applications.[17] Their potential use as novel agents for cancer therapy was reported.[18–21] Gold nanoparticles also have potential for applications in data storage media, since they can increase the capacity of standard DVDs by several thousand times.[22] Additionally, nano-objects have found applications for technological advances in our daily lives. For instance, harmful effects of sun's ultraviolet radiation are diminished by coating glasses with nanoparticles which reflect ultraviolet rays. Antibacterial protections in refrigerators and dishwashers are made by covering the inner walls with metal nanoparticles. The number of examples of these applications is increasing everyday. Scientific and technological developments continue to benefit from fundamental insights into materials' intrinsic properties at the nanoscale. This thesis contributes to understanding the intrinsic properties of single nano-objects and further extends the potential of nano-objects for intriguing applications.

1.2 Advantages of single nano-object studies

Investigations of material properties of nano-objects have mostly relied on measurements from ensembles. Even with the best synthesis method, however, it is almost impossible to obtain nano-objects with the same size and shape. The distribution of material properties causes an inhomogeneous broadening of observed signals. The details are usually not accessible and the observations suffer from averaging. Furthermore, signals which are obtained from ensembles of nano-objects are liable to error because of heterogeneity. For instance, scattering signals quickly decay for metal nanoparticles with sizes smaller than 30 nm. In a suspension of nanoparticles, aggregated

nanoparticles may be present and they have much stronger scattering signals than single particles. Thereby, the ensemble average diameter, which is measured by scattering methods, can be biased towards larger sizes. Despite their known drawbacks, ensemble methods remain irreplaceable because the obtained data from optical signals still carry a wealth of information. Moreover, the experiments can be performed in a relatively simple way (both from equipment and sample preparation points of view).

Although experimental studies on single nano-objects are more challenging, they have significant advantages over measurements on ensembles:

1. It is inevitable to have a distribution of sizes and shapes even with the best synthesis methods. Distribution of variables in a sample is only accessible by measuring properties at the single-particle level. In addition, several optical properties of the same nano-object can be correlated. Fundamental understanding and novel insight into the effect of size and shape on the optical properties become accessible by combining optical and electron microscopy on the same particles.[23]

2. Single nano-objects can be used to probe their nano-environment and they can serve as sensitive optical sensors. Optical signals may vary due to spectral or orientational changes of nano-objects. Fluctuations of the optical signal from a single nano-object can be directly observed. They can be followed to study nanoscale environmental changes, such as refractive index, viscosity, etc.[24] The sensitivity of optical properties to local changes is also enhanced since the inhomogeneous broadening is eliminated. For instance, the red-shift in the plasmon resonance of a gold nanorod related to an increase in the effective refractive index of the medium is sensitive enough to detect the binding of single non-absorbing molecules.[25]

3. Optical signals from single nano-objects can be localized and used to determine positions of nano-objects. Single-molecule trajectories can be determined by precise determination of a molecule's position as a function of time. Their quantitative analysis can be applied to learn about intracellular transport.[26,27] It is also possible to obtain 2-dimensional[28] and 3-dimensional[29,30] trajectories of single gold nanoparticles, which are diffusing in living cells to obtain information about biological events.

4. With single-particle measurements one can select and study rare cases of objects which would be very difficult to extract from ensembles, e.g., pairs of gold nanoparticles.[31,32]

5. Single nano-objects can be harnessed as nano-sized tools. For example, they can be used as local heat sources for cancer therapy.[21]

1.3 Optical properties of single nano-objects

The first far-field optical detection of single molecules at low temperature[33] opened the way for new experiments which could only be performed in ensembles previously. Later, far-field optical methods became more advanced with modern optics and detectors[34–37] and in parallel single molecule fluorescence studies have been extended to detection and spectroscopy of different nano-emitters and nano-absorbers.[38–44] Nano-objects of different sizes, shapes and compositions exhibit a large variety of optical properties.

Single molecules are small (a few nanometers) quantum systems. A molecule can be excited with a few μWs of an excitation light within its absorption band. Fluorescent molecules release the absorbed energy mostly by emitting photons at longer wavelengths than their excitation. The fluorescence signal is then easily separated from the excitation light. Fluorescent molecules are used as valuable tools for a variety of applications ranging from biophysics to soft-matter studies.[24,45–48] They can serve as labels to tag non-fluorescent molecules (protein, DNA, etc.). For instance, kinesin, a molecular motor, was tagged with a fluorescent Cy3 molecule to understand its movement along microtubules. This way, new insight into cellular functions such as cellular cargo transport was gained.[49] Another example is dynamics of polymers near the glass transition temperature. Orientational and translational diffusion of a molecule which was embedded in a polymer matrix were studied to understand the heterogeneity of polymer above and close to glass transition temperatures.[50] For fluorescence detection of single molecules, it is more advantageous to use a molecule which has short fluorescence life-time, high quantum yield, strong one-photon absorption and high photostability. However, these characteristic properties are difficult to obtain and a large number of synthesized molecules do not meet requirements for fluorescence detection. Blinking[51,52] and photobleaching[53] of sin-

gle molecules usually limit the overall experimental process by reducing the time over which the sample can be observed. Moreover, there are many naturally created important molecules (such as DNA) which do not emit photons efficiently. For these reasons, absorption-based detection methods can be complementary to fluorescence-based methods for investigation of molecules which efficiently absorb light but are not necessarily fluorescent (see Chapter 2). These methods would open up new perspectives for a wide range of molecules.

Organic dye nanoparticles are solid particles that are composed of organic compounds. Reprecipitation has been widely employed for preparation of organic nanoparticles due to its simplicity and its ability to control sizes.[54,55] Sizes of organic dye nanoparticles range from tens of nm to micrometer and their morphology is different from inorganic particles such as semiconductor and metal nanoparticles.[54]. Organic dye nanoparticles consist of many molecules, because the molecules are usually compactly packed in the nanoparticle.[55,56] Van der Waals intermolecular interactions and coverage of nanoparticles surfaces with molecules can, in principle, complicate their investigation.[57,58] For instance, fluorescence quenching can occur due to formation of dark $\pi - \pi$ stacked complexes. Fortunately, quenching is usually precluded by introducing bulky or twisted groups to the dye such that these groups restrict intramolecular aggregation of dyes in the nanoparticle.[55,57,59] Moreover, molecules with weakly overlapping absorption and luminescence spectra are usually selected for the formation of dye nanoparticle to minimize the reabsorption of the emitted light within the nanoparticle.[55,57] Thus, organic nanoparticles can produce high fluorescence signals for their detection. In addition to their luminescence, absorption signals can also be used for the detection of dye nanoparticles, which exhibit significant radiationless deactivations through efficient vibrational processes (see Chapter 3).[56] These particles have found diverse applications over the past decades in bioimaging[55,60] and biotechnology studies.[61] For instance, the use of organic nanoparticles as drug delivery systems was recently reported.[61]

In addition, organic nanoparticles can form dewetting-induced short (several microns) or long range (several millimeters) ordered patterns on their thin films.[56,62–64] These thin films could serve as building blocks of organic transistors, organic light emitting diodes, etc.[2,65] However, revealing single morphological domains among patterns with complex 3D structures

can be difficult. For instance, near-field scanning optical microscopy (NSOM) is in principle very useful for morphological and optical correlations.[66] However, the depth of field of NSOM can be limited for studying patterns with different heights compared to that of conventional optical methods. Recent investigations of single organic nanoparticles and their patterns due to the aforementioned difficulties were performed by single-particle spectroscopy. These studies have led to novel discoveries about the photophysical properties of organic dye nanoparticles and of their patterns.[43,56]

Gold nanoparticles are complex many-electron systems. Electromagnetic resonances due to collective oscillations of conduction electrons, called surface plasmons, give fascinating properties to gold nanoparticles. The resonant nature of the surface plasmon makes gold nanoparticles very efficient absorbers and scatterers of light, and their detection by optical methods turns out to be relatively easy. The photoluminescence quantum yield of individual gold nanoparticles can be as high as 10^{-5}.[67] Although the quantum yield of gold nanoparticles is much smaller than the quantum yield of single molecules, gold nanoparticles are still easily imaged by their photoluminescence since they absorb many more photons than single molecules (see Chapter 4 and 5). Unless nanoparticles exhibit any high temperature mediated shape transformation[68,69], their optical signals are perfectly photostable making them suitable candidates for numerous applications where high photostability and brightness are required.[11,70,71] Thus, gold nanoparticles provide advantages over common optical probes such as single fluorophores and quantum dots, which usually suffer from intermittency or loss of fluorescence signal.[51]

The optical properties of gold nanoparticles depend on their size, shape and local environment. The amount of absorbed and scattered light by gold nanospheres at a given wavelength in a homogeneous medium can be calculated analytically from Mie theory.[72] For gold nanospheres, the resonance occurs at a frequency which corresponds to green light. For this reason, a suspension of gold nanospheres appears red in transmission and greenish in scattering.

In the case of gold nanorods, there are two resonant modes, which are due to collective oscillation of conduction electrons along the long and the short axis of the nanorod. These modes are called longitudinal and transverse plasmon resonances, respectively. It is interesting that the longitudinal plasmon

resonance can be tuned from visible ($\sim$ 600 nm) to near-infrared (850 nm) by changing the aspect ratio of the nanorod from 2 to 4.[73] In addition, optical signals of gold nanorods depend on the relative orientation of the nanorod with respect to the excitation polarization.[74–76] The tunable and polarization-dependent optical properties of a gold nanorod can find applications as local sensors at the nanoscale.[71,77]

The surface plasmon resonance of gold nanorods are also sensitive to the changes in their local dielectric environment. For instance, the plasmon resonance wavelength shifts to longer wavelengths when the refractive index of the medium is increased. The sensitivity to refractive index changes is higher for nanorods with a larger aspect-ratio.[78] This sensitivity is exploited in a wide range of applications, such as gas-sensing or molecular binding.[15,79–81]

1.4 Optical detection of single nano-objects

Investigating optical and physical properties of nano-objects on an individual basis requires sensitive methods. Technological developments combined with increasing interest in scientific and technological applications of single nano-objects have led to recent advances in methods to study properties of nano-objects at the single-particle level. Compared to scanning probe microscopy methods, optical techniques are much less invasive and relatively easy to adapt. Optical methods can access individual nano-objects in very complex environments (i.e. cell) or in thick specimens (i.e. polymer film).

Single-particle spectroscopy is applied to nano-objects by studying only one nano-object per laser spot. Nano-objects are separated by distances larger than the size of a laser spot (a few hundred nanometers) in order to inhibit interactions between individual nano-objects ensuring the investigation of at most one particle at a time.

Fluorescence microscopy is a commonly used technique and is capable of detecting luminescent single nano-objects with high sensitivity. When luminescence is too weak to be detected, scattering or absorption methods can be used to detect single nano-objects. The dark-field scattering signal can be an option for plasmonic particles with sizes larger than 30 nm in diameter. For nano-objects that are smaller in size and very weakly luminescent, absorption detection methods can be employed since they are sensitive to very small sizes[38] (of the order of a molecule's size[82]). Moreover, absorption methods

can be applied to any nano-object that absorbs light efficiently.[38,39,82,83] If it is possible to access both radiative (fluorescence, scattering) and nonradiative (absorption) signals, it is also interesting to correlate different signals of the same nano-object. In the following section, we describe the above-mentioned complementary techniques that we have used for the investigation of single nano-objects.

Fluorescence spectroscopy

Fluorescence microscopy has been extensively utilized for detection of single fluorescent nano-objects since the first single-molecule fluorescence detection by Orrit and Bernard in 1990.[33] It provides a broad range of methods for sensitive fluorescence detection of organic or inorganic substances.[84] The luminescence signal is obtained after the nano-object is excited with light in its absorption band. The signal can easily be isolated from background scattering of excitation light using proper filters. Thus, a very high signal-to-noise ratio can be achieved.

Wide-field as well as confocal techniques can be utilized for fluorescence detection of single nano-objects. In wide-field luminescence microscopy, a collimated beam (a few tens of micrometers in diameter) is used to illuminate the sample making it possible to simultaneously detect and follow all luminescent nano-objects distributed over the illuminated area using a CCD or an image-intensifier. In this technique a background signal that originates from emissions away from the focal plane reduces the image contrast. Alternatively, a total internal reflection configuration can be used to largely reduce the out-of-focus signals. In this configuration, an excitation beam is incident on a sample at an angle larger than the critical angle. An evanescent wave is formed on the surface at the light-reflection interface, and the intensity of this wave decays exponentially away from the surface. Only a thin layer ($\sim$100 nm) above the sample is illuminated, therefore the background signal is largely reduced.

In the confocal method, an area ($\sim 10^5$ nm^2) of the size of a diffraction limited spot on the sample is excited. The fluorescence signal is imaged onto a photodetector through a pinhole which is placed in the imaging plane of the detection path. Images with better contrast can be obtained since the luminescence from out-of focus planes of embedding medium is rejected sup-

pressing the fluorescence background. It is also possible to record 3D images with this method by moving the sample or the pinhole in 3D.

Although fluorescence microscopy is very sensitive and has a variety of applications, it can only be applied to luminescent nano-objects. In addition, blinking or bleaching of single molecules or semiconductor nanocrystals decreases their observation time. In order to detect nonluminescent nano-objects, alternative methods are required.

Scattering spectroscopy

Light that is scattered off nano-objects can be used as an alternative signal to fluorescence. The suitability of scattering methods for detection of tiny particles, with sizes below the wavelength of light, was first demonstrated around 1900.[85] The technique has become useful for characterization of spectral and polarization properties of single nano-objects (e.g. silver nanoparticles, gold nanoparticles, quantum dots).[9,77,86–88] In order to detect single nano-objects with this technique, which is mostly applied for detection of plasmonic nanoparticles, either the scattered light alone or the interference of the scattered wave with a reference wave can be used. In dark-field microscopy, light that is directly scattered from a particle is detected on a dark background.[9,89] The advantage of dark-field methods is that it is relatively easy to implement and requires only a standard microscope equipped with low-cost objectives. Wide-field images are recorded in which several hundreds of nanoparticles are visualized simultaneously. Gold nanoparticles as small as 30 nm can be detected using this technique. However, the directly-scattered light intensity varies with the sixth power of the radius of particles and decreases steeply for particles with diameters smaller than 30 nm. The background signal from other scattering objects dominates and nanoparticles can no longer be distinguished.[71]

Nanoparticles with diameters smaller than 30 nm can be detected through bright-field illumination, exploiting the interference of the scattered field ($E_s = sE_i$) with a reference field ($E_r = rE_i$). The detected intensity is the square modulus of the sum of the reference field and the scattered field $I_d = |E_r + E_s|^2 = E_i^2 \left(r^2 + |s|^2 - 2r|s|\cos\theta\right)$, where E_i is the incident wave and θ is the phase difference between the two fields. In bright-field experiments, direct scattering signal $|s|^2$ is negligible for small nanoparticles. The

signal has to be detected against a background signal $|r|^2$ and scales with the interference term $-2r\,|s|\cos\theta$. The interference signal scales with the amplitude of the scattered field. Therefore, the interference signal varies with the third power of the radius of the nanoparticle and is more sensitive to small nanoparticles than the dark-field signal. However, this method lacks specificity for the scattering signals which can also be generated from other scatterers such as impurities, roughness, or local refractive index inhomogeneities. There is a background signal against which the interference signal should be distinguished. Therefore, the scattering signals derived from the interference are usually sensitive to particles down to 10 nm in diameter.[86,87] For detection of individual nanoparticles smaller than 10 nm, absorption based methods, which can create an image contrast only for absorbing objects and suppress background signal from other impurities or interfaces, can be advantageous.[90]

Photothermal (absorption) microscopy

Only a few existing methods have been proved able to directly detect absorption of individual molecules and other nano-objects at room temperature.[42,82,88,91–94]. Photothermal (absorption) microscopy is one of these.[38,39,82,83,90,95–98] In this method, a heating beam is chosen in the absorption band of nano-objects and its intensity is modulated. After a nano-object is excited by the heating beam, the absorbed energy is released as heat. As a consequence, an inhomogeneous refractive index profile builds up around the nano-object, i.e., a time-dependent thermal lens. The thermal lens scatters a probe beam, which is often tuned in a transparency region of the nano-object. The incident wave itself or the reflection of the incident wave from glass-medium interface can be used as the reference field.[95] Interference of the scattered field with the reference field creates small modulated changes in the detected intensity of the probe light. The photothermal signal is obtained by isolating the small modulated component from the detected probe intensity using a lock-in amplifier. In this method, the probe intensity can be very high and the photon noise on the probe beam is considerably reduced. Moreover, the signal is proportional to the nano-object's absorption cross section which scales as the volume of nanoparticles and the background signal from impurities or interfaces is suppressed. Thus, nano-objects with very

small sizes can be detected with this technique.[38] For instance, the photothermal technique is capable of detecting gold nanoparticles with sizes down to 1.4 nm[38] and its sensitivity is not limited to gold nanoparticles.[39,83,96,99]. Moreover, the recent advancements in absorption methods have led to push the sensitivity of absorption-based detection methods to the single-molecule level.

Detection of a single molecule by its absorption used to be a challenging task which could be achieved only by low-temperature experiments until very recently.[100–103] These experiments were favored by the fact that the peak absorption cross section of a molecule is increased by a factor of about 10^6 compared to room temperature values. At ambient conditions, the absorption cross section of a single molecule is very small compared to the diffraction-limited area of a focused laser light. Only one photon in ten millions is absorbed by a molecule which has absorption cross section of ~ 1 Å^2 and is excited with a diffraction-limited laser spot. In addition, rejection of background is not as easy as in fluorescence microscopy methods in which the background is largely removed by proper interference filters.

In 2010, three different groups have independently applied three different methods that allowed the detection of single molecules by their absorption at room temperature. Recently, we have improved the sensitivity of photothermal detection method enabling us to detect single organic molecules by their absorption with a signal-to-noise ratio of 10 in an integration time of 300 ms at room temperature (see Chapter 2).[82] These methods open up new perspectives for utilization of a wide range of molecules, which efficiently absorb light but do not necessarily fluoresce.

After our work, two papers reported single-molecule sensitivity in absorption. Sunney Xie's group has used a ground state depletion microscopy which employs two lasers on resonance with the absorption of a molecule. The first (pump) beam was modulated at 1.75 MHz. It depleted the ground state of the molecule giving rise to a modulation of the absorption of the second (probe) laser at a nearby frequency. The absorption signal was obtained by separating the high frequency fluctuations of the probe laser.[91] This technique is similar to photothermal microscopy in that it detects cross-talk between two beams at different frequencies, but relies on an electronic nonlinearity instead of a thermal one. Repeated line scans are followed to detect absorption of a single molecule and relatively high excitation powers are re-

quired for repeated saturation of the molecule. It is still a challenge to detect dyes with lifetimes of the order of picoseconds or shorter with this method.

Sandoghdar's group utilized a direct extinction method in which the attenuation of the light beam was observed in transmission by direct absorption of a molecule. The sensitivity of this conventional technique was improved by using a balanced photodetector to compensate for the laser noise and by an index matched sample geometry to suppress background scattering.[92,104] Inhomogeneities, e.g. topographic or refractive-index variations, in the sample give rise to background fluctuations which reduce the image contrast. This technique requires averaging of several tens of images to create a contrast for attenuation of light through single-molecule absorption which limits its time resolution. This technique also requires index-matching conditions and minimizing surface roughnesses. Measurements in heterogeneous samples are challenging with this approach.

1.4.1 Correlation of absorption, luminescence and scattering

Simultaneous insight into absorption and luminescence properties further opens new perspectives on the photophysics of labels. Combining different signals of the same label can also expand the observation time and tracking capabilities if labels blink or bleach.

We correlate absorption, luminescence, and scattering signals of the same individual nano-objects. This allows us to

1. specifically determine the quantum yields of single nano-objects (see Chapter 3, 4, 5).
2. estimate the number of molecules per nanoparticle if the nanoparticle is formed of many dyes (see Chapter 3).
3. provide a better description and understanding of photoluminescence of single nano-objects (see Chapter 4, 5).

1.5 Plasmon resonance of a single gold nanorod near a dielectric interface

The influence of surface roughness on intermolecular and surface forces between stationary and sliding solid-solid interfaces is of fundamental interest

for scientific and technological applications.[105–108] Most surfaces in nature are rough[109]. When two solid surfaces are brought together, the contact area between two surfaces can be much smaller than the apparent contact area.[109,110] The real contact area depends on the roughness of the two surfaces and on the normal force between the two surfaces.[111,112] For this reason, sensitive techniques are utilized to study the complex heterogeneity at the contact interfaces. Mostly scanning probe methods such as atomic force microscopy have been utilized. However, the area probed using these methods is usually limited by the size of the tip and the topography images can be affected by the tip shape.[113] Moreover, the deformations under and around the tip can be very different from deformations at distant locations. Optical microscopy techniques can be utilized to extend the observation area and to perform sensitive topography measurements. With the large field of view of optical techniques, the coupling between asperity points over large areas can be directly viewed.

The plasmon resonance of a gold nanoparticle is very sensitive to the changes of local refractive index. Moreover, it was found that the sensitivity of the plasmon resonance is highly distance-dependent because the amplitude of the EM field decays rapidly away from the surface of the gold nanoparticles.[114–117] The effect of the distance between two nanorods, and their relative orientation on their plasmon resonance were studied.[31] In coupling studies of gold nanoparticles, a red-shift in the plasmon resonance was observed while two nanoparticles were brought closer to each other.[118] The sensitivity of plasmons to the coupling distance was used in some of applications.[79,119] For example, DNA hybridization was visualized by the observed blue-shift in the plasmon resonance of the dimers as nanoparticles were brought apart during hybridization.[120] Although coupling of gold nanoparticles with different sizes, shapes, and orientation have been extensively studied,[31,114–117] the effect of the distance between a glass substrate and a gold nanorod on the plasmon resonance of the nanorod has not been measured yet.

For gold nanorods that are immobilized at a glass-medium interface, there is no analytical solution to describe the effect of the substrate on optical properties. Usually, the average of the glass and medium refractive indices is taken as an effective refractive index of the medium. This approximation, however, does not work well in different geometrical configurations of a

nanoparticle in a medium, i.e. different embedding ratios of nanotriangles in PVA.[121] Thus, it is interesting to study the plasmon resonance of a gold nanorod at varying nanorod - dielectric interface distances. In chapter 6 we study plasmon resonances of gold nanorods with respect to an approaching glass substrate. Studies about contact and friction can benefit from the distance-dependent plasmon resonance of gold nanorods.

1.6 Outline of this thesis

In this thesis, we will explore the optical properties of single nano-objects that are immobilized on a glass substrate by using single-particle detection tools. A common theme of this thesis is the absorption measurement and its correlation with luminescence and scattering measurements. We will get insight into the optical properties of nano-objects for their further utilization. In the following, we provide a short overview of the contents of each chapter mainly discussing the important aspects and results of each study.

Chapter 2 We explore different ways (e.g. index matching, using a liquid with high photothermal strength, careful compensation of chromatic aberrations, etc.) to optimize the sensitivity of photothermal imaging and demonstrate that this method can detect a few nW of dissipated power (in an integration time of 10 ms), which corresponds to the power dissipated by a molecule. The achieved improvement has allowed us to detect a single organic dye molecule by its absorption at room temperature with a signal to noise ratio as high as 10. This remained a challenge for two decades.

Chapter 3 We perform simultaneous measurements of absorption and luminescence from the same individual organic dye nanoparticles to characterize their optical properties and sizes. These nanoparticles are prepared by reprecipitation of a dye solution in acetone in water. They show excellent properties for simultaneous measurement of both absorption and luminescence signals. Particularly, the nanoparticles' emission is highly red-shifted from their absorption band which suppresses re-absorption. Moreover, efficient vibrational energy relaxation processes allow the detection of dye nanoparticles in absorption measurements. We quantified the number of molecules in individual dye

nanoparticles. We used 3 independent methods which were absorption microscopy, luminescence microscopy and AFM. These methods revealed consistent results illustrating the potential of correlated absorption and luminescence studies for characterization of complex systems.

Chapter 4 We study the absorption and luminescence properties of single gold nanospheres. Most of the energy absorbed by gold nanoparticles is released as heat and a very small part of it is released by emitting photons. Simultaneous detection of absorption and luminescence allows us to estimate the luminescence quantum yield of gold nanoparticles directly at the single-particle level, which was not possible before. Although the observed luminescence quantum yield is very low, the ability of gold nanoparticles to efficiently absorb light makes them detectable in luminescence measurements. We also found that the luminescence quantum yield of single gold nanospheres does not depend on their size due to the combination of two effects, which are the radiative coupling and the screening factor. Additionally, we describe a laser induced mechanism that can be employed to enhance the luminescence of 20 nm diameter by a factor of 3 to 4.

Chapter 5 We investigate luminescence properties of single gold nanorods to further reveal the effect of the particle shape on the observed luminescence and to investigate the mechanism of luminescence from gold nanoparticles. We studied absorption and luminescence properties of single gold nanorods with aspect ratios ranging from 1 (sphere) to 3.5 by correlating absorption, luminescence and scattering signals at the single-particle level. We found that a quantum yield as high as 10^{-5} can be obtained from nanorods that have a plasmon resonance at about 650 nm. Furthermore, we confirmed the plasmonic influence on the luminescence and observed a weak component (around 500 nm), which contributes to this luminescence. We analyze these spectral components by correlating luminescence and scattering spectra of individual nanorods with different plasmon resonances and performing polarization sensitive measurements on a single gold nanorod.

Chapter 6 It is interesting to investigate the sensitivity of plasmon reso-

nances of individual gold nanorods to the proximity of a dielectric surface. Gold nanorods are very sensitive to the changes in their dielectric environment and can be useful in the study of contact mechanics. We experimentally study the influence of a nearby dielectric interface on the longitudinal plasmon resonance of a gold nanorod. We recorded the luminescence spectrum of a single gold nanorod that is localized on a glass substrate at varying distances. For distances shorter than 400 nm between the nanorod and the glass substrate, we observed significant changes in the plasmon resonance of a gold nanorod and the observed changes are reversible. The obtained results, although preliminary, are promising for application of single gold nanorods as a plasmonic distance sensor.

CHAPTER 2

Room-temperature detection of a single molecule's absorption by photothermal contrast

So far, single-molecule imaging has predominantly relied on fluorescence detection. We imaged single nonfluorescent azo dye molecules in room-temperature glycerol by the refractive effect of the heat that they release in their environment upon intense illumination. This photothermal technique provides contrast for the absorbing objects only, irrespective of scattering by defects or roughness, with a signal-to-noise ratio of $\sim$10 for a single molecule in an integration time of 300 milliseconds. In the absence of oxygen, virtually no bleaching event was observed, even after more than 10 minutes of illumination. In a solution saturated with oxygen, the average bleaching time was of the order of 1 minute. No blinking was observed in the absorption signal. On the basis of bleaching steps, we obtained an average absorption cross section of 4 $Å^2$ for a single chromophore.

The contents of this chapter are based on:
A. Gaiduk, M. Yorulmaz, P. V. Ruijgrok, and M. Orrit, "Room-temperature detection of a single molecule's absorption by photothermal contrast", Science **330**, 353-356 (2010) and A. Gaiduk, P. V. Ruijgrok, M. Yorulmaz, and M. Orrit, "Detection limits in photothermal microscopy", Chem. Sci. **1**, 343-350 (2010)

2.1 Introduction

Single-molecule optical detection[47] has become an indispensable tool in molecular biology and materials science. For the past 20 years, optical single-molecule detection has relied on fluorescence[33,122] because of the low background of this technique. However, monitoring optical absorption more directly would have definite advantages. Fluorescence requires an efficient pathway for populating the emitting state and also the near absence of nonradiative relaxation to the ground state or to intermediate dark states. The fluorescent state is easily destroyed or quenched by photochemical reactions, often involving electron or proton transfer. Indeed, only a very small fraction of all absorbing molecules (called chromophores) are strongly fluorescent (then called fluorophores). Nonfluorescent chromophores include certain metal complexes and many conjugated molecules, for example, DNA bases, that are important in biology. Such molecules could become more natural labels than fluorophores.

The first single-molecule optical detection experiment, by Kador and Moerner, was achieved by absorption[100] but relied on favorable cryogenic conditions, under which the absorption cross section of the narrowest molecular transition was extremely large. Their doubly modulated absorption technique was later improved on with modern optics and detectors,[101–103] but the absorption signal still appears on a strong background of unabsorbed photons, resulting in a lower signal-to-noise ratio than fluorescence. Detecting the absorption of a single molecule at ambient conditions is much more challenging than at low temperature because of the reduction by 5 to 6 orders of magnitude of the cross section, essentially because of fast dephasing by thermal fluctuations. A method for the detection of single-molecule absorption at room temperature must thus solve two different problems.

First, the absorption cross section of a typical chromophore at room temperature is only of the order of 10^{-2} nm^2. The number of the absorption events varies as the ratio of the absorption cross section to the area of a diffraction-limited light beam. This ratio is about 10^{-7} for a laser spot diameter of 300 nm. Because statistical fluctuations in a number N of photons are of order $\sqrt{N}$, a change in transmitted signal of 10^{-7} requires more than 10^{14} photons to be detected. Of those, at least 10^7 have to be absorbed by the molecule. The detection of such small signals therefore requires many

absorption events, which may conflict with the poor photostability of many fluorescent molecules at ambient conditions.

Second, in a direct extinction measurement, where only missing photons are identified, a molecule's absorption appears on a background of scattering by any inhomogeneities in refractive index, arising for instance from roughness of the interfaces. Therefore, for practical applications, it is vital to be able to discriminate true absorption from scattering.

Three main routes have been pursued in the past 10 years toward surmounting these obstacles.

Photothermal contrast relies on the intensity change of a probe beam caused by a modulated heating beam of a different color. Kitamori and coworkers[97] have detected sub-yoctomole concentrations of absorbers in solution with integration times of several seconds, that is, in conditions under which many diffusing molecules contributed in turn to the signal. Boyer et al.[38] applied a similar method to detect single immobilized gold nanoparticles down to 5 nm in diameter, a performance that was later substantially improved by Berciaud et al.[39,95] and has led to a number of applications in recent years.

Alternatively, various sensitive optical techniques have been applied either in interferometers[93] or in a reflection or transmission geometry[40,123] to detect some tens of molecules,[93] small particles,[40] or quantum dots.[88] In the latter two cases, however, the use of ultraclean and stable conditions was essential to ensure the absence of scattering background.

Most recently, Xie and co-workers have explored stimulated emission to distinguish absorption from scattering.[94] Indeed, because stimulated photons can only arise from the excited state of molecules, this method efficiently rejects scattering and fulfills the second requirement. With a modulated stimulating beam, they were able to image absorption in cells down to a few tens of molecules.

In this chapter, we push the sensitivity of photothermal detection to the single-molecule limit. We first discuss the photothermal method and examine the factors influencing the signal and the noise in photothermal detection. We then discuss the ways of improving the signal-to-noise ratio in photothermal microscopy experiments. Finally we demonstrate the detection of nonfluorescent molecules (BHQ1-10T-BHQ1 and BHQ1-Amine) by their absorption with a signal-to-noise ratio of about 10 with reasonable integration times

of 100 to 300 ms.

2.2 Photothermal detection

Photothermal detection is sensitive to the amount of energy absorbed by a nanoobject and dissipated as heat into its local environment. We define as the dissipated power P_{diss} the power provided by the heating beam (with power P_{heat}), which is dissipated as heat by the absorber. The heating-beam intensity is modulated at an angular frequency Ω. Therefore, we call P_{diss} the maximum instantaneous value of this power during the modulation period and the time-averaged dissipated power is $P_{\text{diss}}/2$.

The dissipated power results in a temperature profile $\Delta T(r,t)$ around the nanoabsorber in its embedded medium with thermal conductivity κ and heat capacity per unit volume C_{p}. This temperature profile $\Delta T(r,t)$ in steady conditions with sinusoidal modulation, is given by:[38]

$$\Delta T(r,t) = \frac{P_{\text{diss}}}{4\pi\kappa r}[1 + exp(-r/r_{\text{th}}) \times \cos(\Omega t - r/r_{\text{th}})] \tag{2.1}$$

where r is the distance from the center of the nanoabsorber and $r_{\text{th}} = \sqrt{2\kappa/\Omega C_{\text{p}}}$ is the length characterizing the damping of the heat waves in the medium.

Assuming the response to be instantaneous, this temperature profile in turn causes a refractive index profile $\Delta n(r,t) = \Delta T(r,t) \times \partial n/\partial T$ in the medium, acting as a modulated thermal nanolens.[98] A probe beam is used to detect that nanolens. In the usual photothermal geometry[39,97,98] the scattered probe field $E_{\text{sc}}(\text{t})$ interferes with a reference probe field E_{ref} (usually the transmitted beam or a reflection), and the resulting intensity $I_{\text{det}} \propto |\mathbf{E}_{\text{ref}} + \mathbf{E}_{\text{sc}}|^2$ is detected. In this discussion, we neglect the difference in spatial modes of the two fields, which are supposed to be similar. The lock-in amplifier isolates the weak contribution of the interference signal $2\text{Re}\left[E^*_{\text{ref}} E_{\text{sc}}(t)\right]$ modulated at the same frequency as the heating beam. The contribution of the modulated scattered intensity $|\mathbf{E}_{\text{sc}}|^2$ is neglected for small particles (typically < 60 nm).[42] For larger particles, a non-negligible static scattered field acts as an additional in-phase reference field. Its contribution to the interference intensity I_{det} is reported in photothermal correlation spectroscopy experiments for 80 nm gold particles.[124]

The photothermal signal S is proportional to the field scattered by an effective volume V where the refractive index is modulated. The refractive index change Δn depends on the absorption cross section σ_{abs} of the nano-object and the heating beam with intensity I_{heat} focused into a diffraction-limited spot with area A. Δn is proportional to the power dissipated by the nano-object $P_{\text{diss}} = I_{\text{heat}}\sigma_{\text{abs}} = \sigma_{\text{abs}}P_{\text{heat}}/A$. The field scattered by the thermal lens can be approximated by that of an equivalent dipole $|\mathbf{p}| \approx 2n\Delta n \cdot V \cdot \left|\mathbf{E}_{probe}\right|$, where $\Delta n \cdot V$ stands for the volume integral of the position-dependent refractive index change of the lens. The scattered field is radiated by this dipole: $|\mathbf{E}_{\text{sc}}(t)| \approx \frac{1}{4\pi\varepsilon_0\omega_0\lambda^2}|\mathbf{p}|$, and the photothermal signal can then be written as an optical power:

$$S \approx \frac{1}{\pi\omega_0} n \frac{\partial n}{\partial T} \frac{1}{C_p \lambda^2 \Omega} \frac{\sigma_{abs}}{A} P_{heat} P_{probe} \Delta t \tag{2.2}$$

where ω_0 is the probe beam focal radius (beam waist), C_p is the heat capacity per unit volume of the photothermal medium (for example, C_p for glycerol is 2.6×10^6 $\text{Jm}^{-3}\text{K}^{-1}$), λ and P_{probe} are the wavelength and power of the probe beam, and Δt is the integration time of the lock-in amplifier. We assume the thermal conductivity of metal nanoparticles to be much larger than that of the surrounding media (for example, $\kappa_{\text{gold}} = 310$ $\text{Wm}^{-1}\text{K}^{-1}$, $\kappa_{\text{water}} = 0.56$ $\text{Wm}^{-1}\text{K}^{-1}$).

The noise in actual experiments arises from the detector, from fluctuations of the probe laser power, and from photon noise of the detected optical power. In practice, the experimental noise is always larger than the photon noise, but can be close to it for an optimized setup. Here, assuming an ideal detector and a shot-noise limited detection, the noise N_s on the photothermal signal S would be:

$$N_s \propto \sqrt{\frac{P_{probe}\Delta t}{h\nu}} \tag{2.3}$$

Combining the expressions for the signal and the noise, we see that the signal-to-noise ratio SNR for the shot-noise-limited photothermal detection is given by:

$$SNR \approx \frac{1}{\pi\omega_0\lambda^2\Omega} n \frac{\partial n}{\partial T} \frac{1}{C_p} \frac{\sigma_{abs}}{A} P_{heat} \sqrt{\frac{P_{probe}\Delta t}{h\nu}} \tag{2.4}$$

2.3 Optimizing the SNR in photothermal detection

Here, we discuss how the SNR can be optimized by tuning all factors in Eq. 2.4, and we point out the practical limits to the optimization.

1. Increase the dissipated power up to the allowed maximum, usually fixed by saturation. For gold nanoparticles, the applicable powers are very high (the bulk melting temperature of gold is about 1300 K, and the temperature rise to reshape gold nanorods, although significantly lower[68,69,125] is still some hundreds of K). The allowed temperatures in biological samples, however, will be much lower. The melting intensity for a spherical particle with diameter 20 nm in water is around 20 MW/cm^2 at 514 nm (about 20 mW focused on a diffraction limited spot), and scales with R^{-2}. For a non-fluorescent molecule, the saturation intensity is determined mostly by the excited state lifetime τ, typically 0.1 ns, which leads to a dissipated power of a few nW.
2. Increase P_{probe} as much as possible. Practical limits are set by the maximum available laser power and by residual absorption of the probe beam by the sample. For example, the probe intensity can be increased until the probe-induced and pump-induced heating are comparable. For small gold NPs in glycerol, for example, we can use up to 125 times more probe intensity at 800 nm than heating intensity at 514 nm, as given by the ratio of the absorption cross sections.
3. Match the heat diffusion length r_{th} with the spot size, by choosing the right modulation frequency.[38,95] A lower modulation frequency generally leads to a higher photothermal signal, until the thermal lens exceeds the size of the focused probe beam. The optimal value of the modulation frequency also depends on the experimental noise spectrum.
4. Optimize the optical and thermal properties of the photothermal medium, including refractive index, its derivative with respect to temperature, heat capacity and conductivity.
5. Reduce the reflected intensity to reduce the laser noise by matching the indices of the substrate and the photothermal medium. (Only in reflection geometry.)

6. Increase the integration time of the lock-in amplifier. This parameter can be increased arbitrarily, provided the mechanical stability of the experimental setup and the photostability of the sample allow it.

2.4 Experiment

2.4.1 Samples

In this section we discuss how the samples were prepared for photothermal microscopy experiments. We firstly describe how we cleaned the glass slides. Then we explain how we prepared samples with single gold nanoparticles and single azo dyes.

Glass coverslides cleaning

Cleanliness of substrates and liquid is very important. There are many more absorbing molecules than fluorescent ones. The background problems become severe unless enough attention is paid to obtain a sample free from impurities.

Glass coverslides (Menzel, Germany) were cleaned in several successive sonication steps of 20 min in each of the following liquids: 2 % Hellmanex water solution, acetone, ethanol (AR grade), and Milli-Q water. Experiments were performed in a fluid cell (approx. $50 - 150$ μL volume) made from a rubber o-ring or a top of plastic Eppendorf tube attached to the coverslip. Clean glycerol ($> 99.5\%$, spectrophotometric grade) and hexane (AR grade) were used for experiments.

Gold nanoparticles

We used gold nanoparticles to characterize the sensitivity of our setup in absorption measurements. Gold nanoparticles provide good photostability and do not show saturation effects.

Samples of gold nanoparticles with diameters of 20, 10 and 5 nm (British Biocell International, EM.GC20) were prepared by dilution in ultra-pure water at volume ratios of 1:4, 1:20 and 1:25 respectively. Approximately 50 μL of the suspension were deposited on the surface of cleaned glass immediately after the filtration through a 450 nm porous membrane and spin coated at

2000 rpm for 5 s, followed by drying at 4000 rpm for 90 sec.

Black-Hole-Quenchers®

We selected a non-fluorescent azo dye which has a low quantum yield and a large dissipated power at saturation for photothermal detection.

Constructs of DNA with Black-Hole-Quenchers® (BHQ) were purchased from Eurogentech. Two BHQ1 molecules (BHQ1-10T-BHQ1) are about 3 − 4 nm apart as defined by the length of single-stranded DNA (ssDNA) primer (10T = 10 thymine nucleobases). The BHQ1-10T-BHQ1 construct shows maximum absorption at 520 nm in water and at about 530 nm in glycerol (see Fig. 2.1). The absorption of the construct at 514 nm is 1.6 times higher in glycerol than in water.

In order to prepare samples of DNA constructs for optical microscopy experiments, we spin-coated approximately 50 μL of the 10 nM aqueous solution of DNA constructs on the surface of clean glass slides at 2000 rpm for 5 s which was followed by drying at 4000 rpm for 90 s.

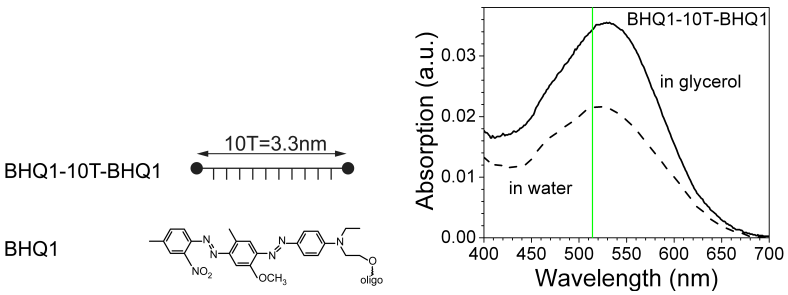

Figure 2.1: (Left) Schematic representation of the DNA construct (BHQ1-10T-BHQ1) and chemical structure of Black-Hole-Quencher (BHQ1) molecule. (Right) Absorption spectra of BHQ1-10T-BHQ1 construct in water (dashed) and in glycerol (solid) showing maximum absorption at 520 nm and at about 530 nm, respectively.

A batch of Black-Hole-Quencher® (BHQ1-Amine, $C_{24}H_{29}N_7O_3$, M_w = 475 Da) was purchased from Biosearch technologies, Inc. The absorption spectra of BHQ1-Amine molecules in water and in glycerol are shown in Fig. 2.2. For single-molecule absorption measurements, BHQ1-Amine molecules were deposited on the clean glass surface in the same way as DNA constructs sample.

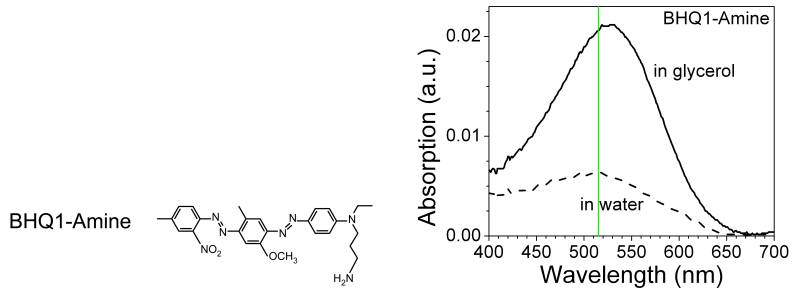

Figure 2.2: (Left) Schematic representation of the BHQ1-Amine molecule. (Right) Absorption spectra of BHQ1-Amine molecules in water (dashed) and in glycerol (solid) showing maximum absorption at 520 nm and at about 530 nm, respectively.

A chromophore that efficiently absorbs light and converts the absorbed energy efficiently into heat would be a good candidate for demonstration of room-temperature detection of a single molecule's absorption. In addition, the photochemical stability of the molecule is important and the molecule should resist bleaching for a long period.

The extinction coefficient of BHQ1 at the absorption maximum ($\sim$ 520 nm) in water is 34000 $M^{-1}cm^{-1}$. We assume the fluorescence lifetime of BHQ1 is 50 ps or less. The fluorescence lifetime of similar azo dyes was measured to be about 2 ps in various solvents[126] and several tens of ps in a polymer matrix[127].

2.4.2 Photothermal microscopy setup

The experimental setup is based on an inverted optical microscope, Olympus IX71, equipped with Olympus 60$\times$ oil immersion objective (NA = 1.45). The schematic of the setup is shown in Fig. 2.3. The heating beam is provided by an Ar-ion laser (Coherent Innova 300) and passes the acousto-optical modulator with a typical modulation frequency of about 1 MHz. The absorbed power provided by the heating beam gives rise to a temperature gradient (see Eq. 2.1) with an amplitude $\Delta T_{surf} = \frac{\sigma_{abs} I_{heat}}{4\pi\kappa R}$ at the surface of the source, assumed to be spherical: σ_{abs} is the absorption cross section of the absorber, I_{heat} the pump intensity, κ the thermal conductivity of the medium, and R the radius of the heat source. The probe beam at 800 nm is produced by a Ti:sapphire laser (S3900s, Spectra Physics) pumped with the Ar-ion laser.

Sets of spatial filters and telescopes expand initial beams to $\sim$ 20 mm to overfill the entrance pupil of the microscope objective ($\sim$ 10 mm). The beams are overlapped at a dichroic mirror and sent towards the objective. The photothermal signal is collected in the back-scattered mode and detected by a Si photodiode with an adjustable gain (DHPCA-100-F, Femto) and fed into the lock-in amplifier. The experiment is controlled with a home-written LabView software, and the data are collected by an acquisition card (ADWin Gold). The raster scanning of the samples is performed with a 3-axis piezostage (MARS II, Physik Instrumente).

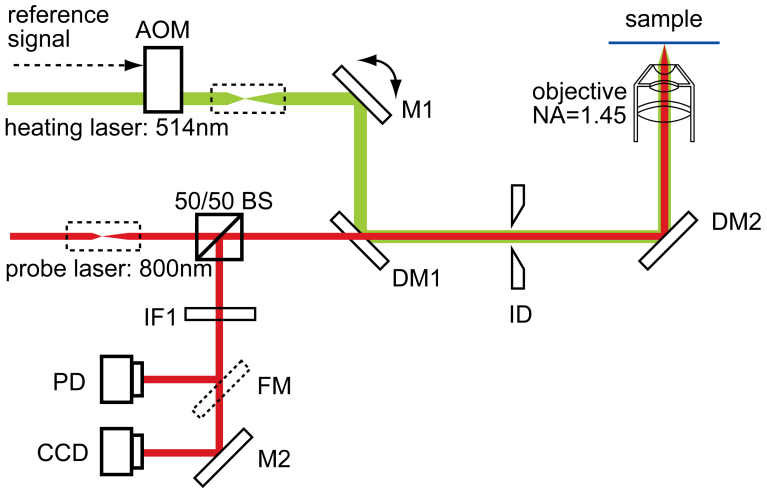

Figure 2.3: Scheme of the experimental setup for simultaneous photothermal detection. AOM - acousto-optical modulator, M - mirrors (scanning M1 is used for the control of the transversal alignment of the heating and probe beams), FM - flip mirrors, BS - beam splitter, DM - dichroic mirrors, ID - iris diaphragm, IF - interference filters, PD - photodiode, CCD - video cameras. Positions of beam-expanding telescopes are indicated with dashed boxes. Spatial filters are not shown in this schematic representation.

The photothermal signal is proportional to both the heating and probe powers. We modulate the heating beam at rather high frequency (around 1 MHz) to reject mechanical, electronic, and laser noise. In addition, we have chosen the reflection geometry with index matching to adapt the probe signal to the characteristics of our fast low-noise detector (maximum detected intensity 18 μW). A weak reflection of about 10^{-4} was obtained by using glycerol as the photothermal liquid ($n_{glyc.} = 1.47$) on top of a substrate of

cover glass ($n_{subs.} = 1.52$). With this near index match, very high probe intensities become applicable and the photon noise on the probe beam is therefore considerably reduced.

A near overlap of the two tightly focused beams with different colors that would yield maximum photothermal signal is also very critical. The photothermal signal was maximized by careful compensation of chromatic aberrations with the help of separate telescopes for different colors (dashed boxes in Fig. 2.3). A fast steering mirror (M1 in Fig. 2.3) was also used for transversal movement of the heating beam to check for the transversal overlap of the heating and probe beams.

2.5 Characterization of photothermal detection sensitivity on gold nanoparticles

We used our photothermal microscopy setup to improve the photothermal detection approach of Berciaud et al.[39,95]. We see that the choice of the transducing fluid is crucial to enhance the sensitivity (see Section 2.3). In addition, careful optimization of foci for the two different wavelengths to compensate for geometric and chromatic aberrations is very important to create and detect the maximum allowable signal from the nanoabsorber. We first characterized the sensitivity of our setup with gold nanoparticles used as calibration for estimating absorption cross sections. Their size and shape are well-known. For specific size, shape and local environment, the absorption cross sections of gold nanoparticles are calculated and match measured values.[42,72,128]

Figure 2.4 A shows an image of a sample containing 10 nm and 5 nm diameter gold spheres immersed in glycerol on glass surface. We measured photothermal signals by heating at 514 nm and probing at 800 nm. The signals from different diameters differ by a factor of about 8, as expected from the volume ratio. The elongated shape of the photothermal spots in this image (210 nm and 370 nm principal half-maximum widths) arose from the shape of the pump beam, because spatial filtering was weak in this experiment. Stronger spatial filtering yielded a much better shape (see Fig. 2.4 C and D).

We measured the photothermal detection volume by scanning a 20-nm

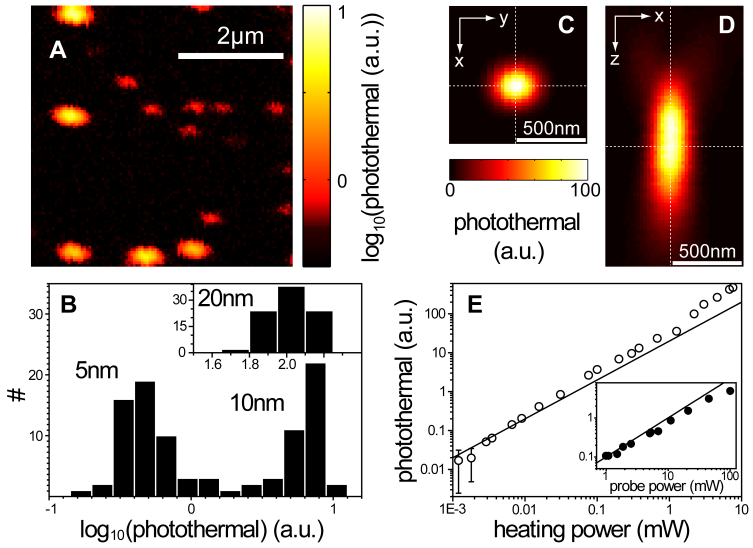

Figure 2.4: Photothermal images of gold nanospheres illustrate the large dynamic range of the method and its low background. (A) A raster scan image of a sample containing 10-nm (yellow) and 5-nm (red) diameter gold particles in glycerol: heating power is 0.43 mW; probe power, 21 mW; integration time per pixel, 3 ms. The FWHMs of the photothermal spots are 210 nm and 370 nm. a.u., arbitrary units. (B) Histogram of the photothermal signals for 94 gold particles of 5-nm or 10-nm diameter. (Inset) Histogram of signals for 88 gold particles of 20-nm diameter in the same conditions. As expected, the photothermal signal roughly scales as the volume of the particles. (C and D) In the case of strong spatial filtering, the point-spread function (PSF) of the photothermal signal is well fitted by a Gaussian with $\sigma_x = 220\ nm$, $\sigma_y = 250\ nm$, and $\sigma_z = 670\ nm$, as mapped by scanning a 20-nm-diameter gold particle in three dimensions. Note the two weak lobes of the PSF in the x, z image, also observed in confocal fluorescence microscopy. (E) Linear scaling of the photothermal signal of a 20-nm gold particle with heating and probe (inset) powers. Solid lines show linear fits at low heating and probe powers. Error bars indicate standard deviation values. For most of the data, they are smaller than the symbol size.

gold sphere in three dimensions.[90] The full widths at half maximum (FWHM, determined by a Gaussian fit) across x, y, and z are 220 nm, 250 nm, and 670 nm, respectively. These data are represented in Fig. 2.4 C and D. Last, we verified the linear relationships between pump and probe powers and photothermal signal by varying the heating power over 4 orders of magnitude

(1 μW to 10 mW) and the probe power over 2 orders of magnitude (1 mW to 100 mW). Slight deviations from linear behavior at high power may be due to variations of spectral or thermal characteristics of the materials in the broad range of temperature changes explored (from 0.05 K up to about 500 K).

2.5.1 Minimum detectable dissipated power

To ascertain the possibility of detecting a single organic molecule in photothermal microscopy, we only need to compare the smallest detectable power over a given integration time to the power dissipated by a single molecule.

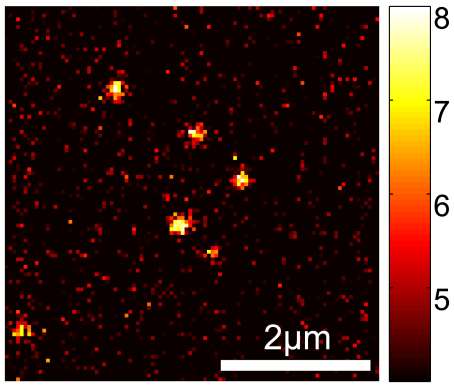

Figure 2.5: Photothermal image of 20 nm gold nanoparticles in glycerol with $P_{heat} = 1$ μW, $P_{probe} = 68$ mW, $\Delta t = 10$ ms. The color scale of photothermal image shows the SNR.

We probe the limits of photothermal detection on 20 nm diameter gold nanoparticles by reducing the dissipated powers as far as possible while having a reasonable SNR of the spots in the image. The result of this experiment is shown in Fig. 2.5. The photothermal spots are obtained when the gold nanoparticles were excited at 514 nm with 1 μW power at the sample. The probe laser power was 68 mW at 800 nm. The average SNR of photothermal spots is 8 with an integration time of 10 ms per pixel.

This way, we experimentally estimate the smallest dissipated power (p_{diss}) and temperature rise (ΔT_{surf}), which we can detect. Under this experimental conditions, we calculated the average dissipated power due to the heating beam as $p_{diss} = 2.6$ nW with a corresponding temperature rise of

$\Delta T_{surf} = 80$ mK.

By increasing the integration time to hundreds of ms, even smaller dissipated powers can be measured.

2.6 Detecting a single molecule by its absorption

A single molecule can release heat along two pathways: a direct nonradiative transition from the excited state and vibronic relaxation before and after a radiative fluorescent transition. The shorter the fluorescence lifetime (τ_F) and the lower the fluorescence quantum yield (η_F) are, the larger is the dissipated power at saturation. The most favorable molecules for photothermal detection should therefore have strong nonradiative channels and thus very weak fluorescence yields. This is the case for the trial molecules chosen in the present work. We calculated the dissipated power at saturation for several commercially available organic molecules (see Appendix A). The highest dissipated power at saturation of 15 nW well above the limit of 3 nW was obtained for a high-efficiency dark quencher (Black-Hole-Quencher, BHQ1, Biosearch Technologies, Novato, California). This azo dye molecule is used in the construct of oligonucleotide probes to quench the fluorescence of a dye in a DNA construct.[129,130] For the present experiments, we first perform absorption measurements on a chromophore-DNA construct to increase the absorption signal by the presence of two chromophores in each construct and to secure the adhesion of the constructs to the glass surface by their single-strand DNA linker (Fig. 2.1). Then we demonstrate the detection of optical absorption at a single molecule level by using single BHQ1-Amine molecules.

2.6.1 Single BHQ1-10T-BHQ1 constructs

A photothermal image obtained on a sample of spin-coated quencher-DNA construct (BHQ1-10T-BHQ1) submerged in nitrogen-bubbled glycerol is shown in Fig. 2.6 A. The image reveals four photothermal spots with a SNR $\sim$ 10 for an integration time of 300 ms. These spots persisted for as long as 1 hour without bleaching or fading. Less than 2% of the molecules bleached in the first 10 min of illumination. When the glycerol was saturated by oxygen, in contrast, one-step photobleaching was observed after an average time of $\sim$ 1 min. Several typical background-corrected photothermal

traces are displayed in Fig. 2.6 B and demonstrate digital irreversible steps. We never observed any blinking or any later reappearance of a bleached photothermal signal.

The absolute value of the change in absorption cross section upon photobleaching is estimated by comparison to the photothermal signal of 20-nm gold nanoparticles. The calculated[42,72] cross section of these gold nanospheres is 460 nm^2 at 514 nm in glycerol, in good agreement with absolute cross section measurements.[128]

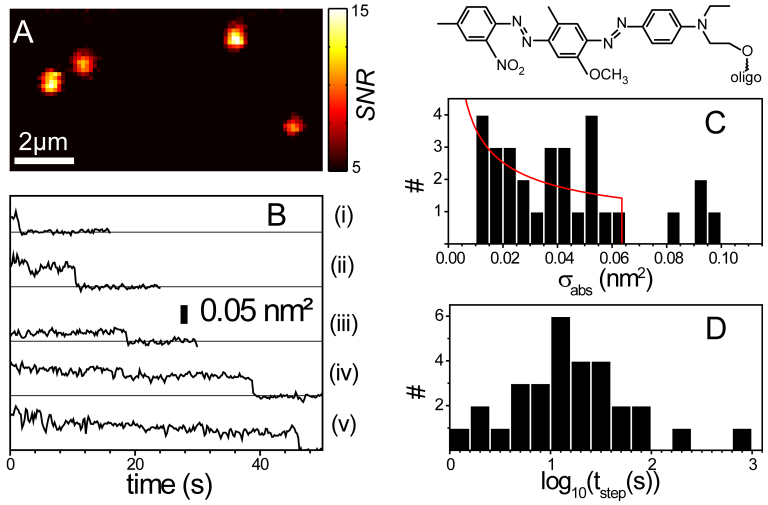

Figure 2.6: (A) Photothermal image of four constructs (BHQ1-10T-BHQ1), consisting of two fluorescence quenchers (BHQ1) attached to a single strand of DNA (10 thymine bases): integration time per pixel, 300 ms; heating power, 5.1 mW at 514 nm; probe power, 84 mW at 800 nm. (B) Photothermal time traces showing single-step bleaching obtained on a sample with BHQ1-10T-BHQ1 on glass in oxygen-saturated glycerol: integration time per point, 100 ms; heating, 5.1 mW; probe, 84 mW. (C) Histogram of amplitude of 30 bleaching steps in the photothermal traces. The average change in absorption cross section upon bleaching is 4.1 $Å^2$. The red line represents the distribution of absorption cross sections of single chromophores corresponding to the isotropic distribution of transition dipole moments. The cutoff at 6.3 $Å^2$ is the calculated cross section for a perfectly oriented molecule. (D) Histogram of survival times before one-step photobleaching events for the same set of data. The average time is 49 s.

The histogram in Fig. 2.6 C summarizes the absorption cross-section changes in 30 single bleaching steps, with an average value of 4.1 $Å^2$. This

value, which corresponds to the cross section of a single chromophore, is in satisfactory agreement with the isotropic value, $\sigma_{BHQ} = 2.1$ Å^2, deduced from the absorption spectrum of the quencher-DNA construct in glycerol. Note that the maximum value of the cross section for a favorably oriented molecule is $3\,\sigma_{BHQ} = 6.3$ Å^2. The histogram of Fig. 2.6 C is a broad distribution without distinct maximum, in qualitative agreement with the isotropic distribution of transition dipole moments (solid line in Fig. 2.6 C with a step-like cutoff at $3\,\sigma_{BHQ}$). Our observation suggests that the absorption dipoles of BHQ1 molecules are not freely rotating, even under the heavy illumination to which we subjected them, and that the molecules are fixed to the surface and/or to the DNA linker.

The histogram of survival times before digital photobleaching is shown in Fig. 2.6 D. The average number of absorbed photons before bleaching is about 10^{11} under oxygen-saturated conditions and larger than 10^{12} under oxygen-free conditions, showing a huge reduction in the bleaching efficiency per photon compared with usual fluorophores in the same conditions. This robustness can be attributed to the much shorter dwell time in the excited singlet state resulting from the efficient internal conversion. We have attempted measurements of the polarization dependence of single-molecule absorption signals, but these measurements were very difficult because of the buildup of a photothermal background over long illumination times by the pump beam (the probe had no noticeable effect on this buildup).

We could not observe simultaneous fluorescence and photothermal signals from the spots of Fig. 2.6. Such simultaneous signals arose only from abnormally bright spots, attributable to large aggregates, and showed quick correlated decays of both signals upon illumination. On the sample of Fig. 2.6, we also observed a few spots with strong photothermal signals corresponding to an absorption cross section of about 1 nm^2, which showed one-step bleaching. Possible interpretations are aggregates of several molecules desorbing simultaneously or, more probably, another chemical species with a large absorption cross section, possibly with excited-state absorption of the intense probe beam. We only found very few examples of two-step photobleaching of the BHQ1-10T-BHQ1 constructs. We believe that this absence results from the low probability of bleaching, joined with the low probability of finding two favorable orientations in the same construct.

2.6.2 Single BHQ1-Amine molecules

We performed the photothermal microscopy experiments on single BHQ1-Amine molecules under similar conditions as with DNA-constructs. The photothermal image of the molecules is shown in Fig. 2.7. The color-scale stands for the SNR and the calculated absorption cross sections σ_{abs}, simultaneously. We could image an arbitrary single BHQ1-Amine molecule with an average absorption cross section of $\sim$3 Å^2 with a signal-to-noise ratio of $\sim$ 11, which is in good agreement with the previously represented performance of the setup. We see a distribution in absorption cross sections which are within the range of isotropic $\sigma_{BHQ} = 2.1$ Å^2 and $3\,\sigma_{BHQ} = 6.3$ Å^2 of a favorably oriented molecule (see section 2.6.1). This observation suggests a similar conclusion as with DNA-constructs, that the molecules are not freely rotating and they are fixed to the substrate.

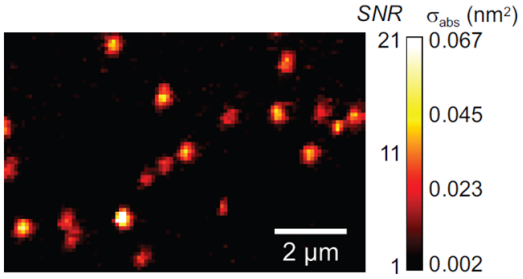

Figure 2.7: Photothermal image of BHQ1-Amine molecules on glass surface in glycerol: integration time per pixel 300 ms, heating power 5.1 mW at 514 nm, probe power 79 mW at 800 nm.

2.7 Conclusions

Our successful single-molecule detection relied here on favorable conditions, the use of glycerol (with large $\partial n/\partial T$ and poor heat conduction) instead of water, with a high heating power of 5.1 mW focused into the diffraction-limited spot and with an even higher probe power of more than 70 mW. Although the conditions for single-molecule absorption in a cell, for example, would be far from these ideal ones, this result opens the way for further optimization of the technique and to a much broader variety of absorbing molecules. Interesting candidates are natural absorbers, for example, metal

proteins such as hemoglobin, which would be useful for applications in analytical biochemistry and medical assays.[131]

An intrinsic limitation of the photothermal method is the low transduction factor between pump and probe because of the relatively weak variation of refractive index with temperature. A future search for more-efficient transduction, for example, photomechanical or photoelectrical detections using micro- and nano-optomechanical systems,[132] appears full of promise.

Acknowledgements

We acknowledge financial support by European Research Council (Advanced Grant SiMoSoMa). This work is a part of the research program of the Stichting voor Fundamenteel Onderzoek der Materie, which is financially supported by the Netherlands Organization for Scientific Research. We thank Harmen van der Meer for precious help with the experimental setup.

CHAPTER 3

Absorption, luminescence and sizing of organic dye nanoparticles

Organic nanoparticles made of a push-pull triarylamine dye with an average diameter of 60 nm, were prepared by reprecipitation. We study their photophysical properties by a combination of photothermal and fluorescence microscopy. Photothermal contrast provides a quantitative measure of the number of absorbers. The size of nanoparticles estimated from the absorption measurements was compared with sizes measured by AFM. Fluorescence and absorption microscopy provide quantum yield on the single-particle level as a function of excitation intensity. The quantum yield strongly decreases at high intensities because of singlet-singlet or singlet-triplet annihilation. We also report the formation of molecular thin layers and of labyrinth-shaped structures on glass substrates, presumably induced by dewetting.

The contents of this chapter are based on:
A. Gaiduk, M. Yorulmaz, E. Ishow, and M. Orrit, "Absorption, luminescence and sizing of organic dye nanoparticles and of patterns formed upon dewetting", ChemPhysChem **13**, 946-951 (2012)

3.1 Introduction

For decades, nanoparticles that are composed of metal and inorganic semiconductor materials have attracted much attention due to their unique size-dependent optical properties.[71,133–135] Various organic molecules with large structural diversity can form nanometer-sized particles (10-250 nm diameter). These nanoparticles are typically prepared by reprecipitation,[54] sol-gel formation,[136] laser fabrication,[137] or reprecipitation-encapsulation.[138] Organic nanoparticles are potential labels for biomedical imaging and sensing,[139–141] as well as promising materials for the fabrication of organic light-emitting diodes, field-effect and thin-film transistors, and photovoltaic solar energy collectors.[1,2] Self-organized patterns of nanoparticles[66,142] have been credited for the tunability of charge transport[143] and optical properties.[144] Strong correlations between morphology and fluorescence properties were demonstrated by near-field scanning optical microscopy in thin films of organic materials.[145,146] Considerable attention is currently paid to multicolor emission of organic nanoparticles under monochromatic excitation, and to the control of the emission range by changing only one active unit of a dye.[147] Also, Gesquiere et al. have shown that the emission color depends on the crystal structure of perylene-derivative nanoparticles, which is related to the size of nanoparticles.[43] For conjugated polymers, Wang et al. observed an increase in the fluorescence intensity with the size of alkyl-PTA and alkoxy-PTA nanoparticles (smallest size of 100 nm), and changes in the absorption spectrum upon their aggregation-driven growth.[148]

Light-scattering, absorption and fluorescence microscopy are typically used for investigating ensembles of organic nanoparticles. For individual nanoparticles, however, most scattering methods work well only for particles with diameters larger than 40 nm,[42,149,150] and a few are capable to visualize smaller diameters.[86–88] Alternatively, detection of individual gold nanoparticles with diameter down to 1.4 nm,[42,93] and even single organic molecules at room temperature are demonstrated in absorption microscopy.[82,91,92,104] Well-established fluorescence microscopy provides a broad range of methods that are used in biology, chemistry and material science.[36,151–154] A combination of photothermal microscopy and fluorescence microscopy[155,156] provides simultaneous insight into the absorption and fluorescence characteristics of single nanoparticles.

Here, we have selected 4-di(4′-*tert*-butylbiphenyl-4-yl)amino-4′-dicyanovinylbenzene (fvin)[147] molecule because of its absorption maximum around 450 nm, near the monochromatic excitation wavelength (514 nm), and for its red-shifted emission, peaking at around 620 nm, provided by a strongly distorted charge-transfer excited state. Along with its emission properties, the fvin excited state exhibits significant radiationless deactivation to the ground state through efficient vibrational processes. The heat dissipated upon internal conversion is detected in photothermal microscopy as a refractive index change of the local environment. Moreover, the peripheral bulky groups prevent the molecules from forming dark $\pi - \pi$ adducts. Finally, the complex shape and flexible backbone of fvin enables the formation of stable spherical fvin nanoparticles, giving rise to colloidal solutions by means of a simple reprecipitation method without the use of any surfactant.

In addition to previously stated optical and physical properties of fvin that make its NPs a suitable candidate for combined photothermal and fluorescence microscopy experiments, we find that microstructures are formed upon dewetting of the precipitate suspension. Similar structures are believed to favor charge collection in solar cells.[157]

Herein, photothermal[82] microscopy and fluorescence microscopy are first simultaneously applied for quantitative characterization of single immobilized organic nanoparticles (NPs) formed from the fvin molecule.[147] Then, the same characterization is employed on the dewetting induced microstructures. The combined technique reveals the complex luminescence mechanism affected by singlet-singlet or singlet-triplet annihilation and is utilized to determine the luminescence quantum yield of each individual fvin NP. The number of molecules in each individual NP is obtained from their absorption signal, luminescence signal and their volume. The number of molecules building up the structures is deduced from their optical absorption.

3.2 Experimental section

3.2.1 Combined photothermal and fluorescence microscopy

Optical microscopy experiments were performed on a combined photothermal and fluorescence microscope, home-built around an inverted optical

microscope (Olympus IX-71). The optical setup is schematically shown in Fig. 3.1. Details of photothermal detection were described in Chapter 2. In addition, the 514 nm emission of an Ar-ion laser (Coherent Inc, Innova 310, 10 W) was used here for both fluorescence excitation and photothermal heating of nanoparticles to detect them simultaneously in fluorescence and absorption, respectively. The same laser pumped a tunable continuous wave Ti:Sapphire laser (Spectra Physics, S3900s) which operated at 800 nm and served as a probe laser for absorption measurements.

For photothermal imaging, the intensity of the heating beam was modulated ($\sim$1 MHz) using an acousto-optic modulator (AOM, AA Optoelectronic) or an acousto-optical tunable filter (AOTF, AA Optoelectronic). In the latter case, the AOTF was also used to select the desired emission line from the Ar-Ion laser. The heating and the probe beams were expanded ($\sim$20 mm) and spatially overlapped on a dichroic mirror (BS 669, AHF or 595 DCXRR, AHF) by means of telescopes. Two different telescopes were used for heating and the probe beams to adjust their overlap in the focus of the oil immersion microscope objective (Olympus, 60$\times$, NA=1.45), thereby compensating for chromatic aberrations. Both beams were focused on the sample using the microscope objective (Olympus, 60X oil immersion, numerical aperture 1.45) after being reflected by a dichroic mirror (AHF z532/NIR). Nanoparticles were deposited on a cover glass and immersed in glycerol.

The back-reflected probe beam and fluorescence signals were collected by the same microscope objective and sent towards the dichroic mirror (AHF z532/NIR), which was separating the heating and probe light from the fluorescence signal. The probe beam passed through a 50/50 beamsplitter, longwave pass filters (LWP700, LWP750), and was focused on a variable-gain Si photodiode (Femto DHPCA-100-F). The output of detected signal was fed into a lock-in amplifier (SR844, Stanford Research Systems) and the photothermal signal was obtained by isolating the small modulated component from the high DC signal arising from the reflection of the probe beam from the glass-glycerol interface.

For luminescence imaging, the luminescence signal of nanoparticles, which was obtained by excitation at 514 nm, was spatially filtered by a 30 μm confocal pinhole and spectrally selected by a set of bandpass filters (AHF 615/150 and Omega 590/100), and was focused on a single-photon-counting avalanche photodetector (SPCM-AQR-16, Perkin-Elmer).

The experiment was controlled by using a home-written LabVIEW software. Data were collected by a data acquisition card (ADWin Gold, Germany). The raster-scan imaging was provided by a three-axis piezostage (Mars II, Physik Instrumente). ImageJ was used for data analysis.

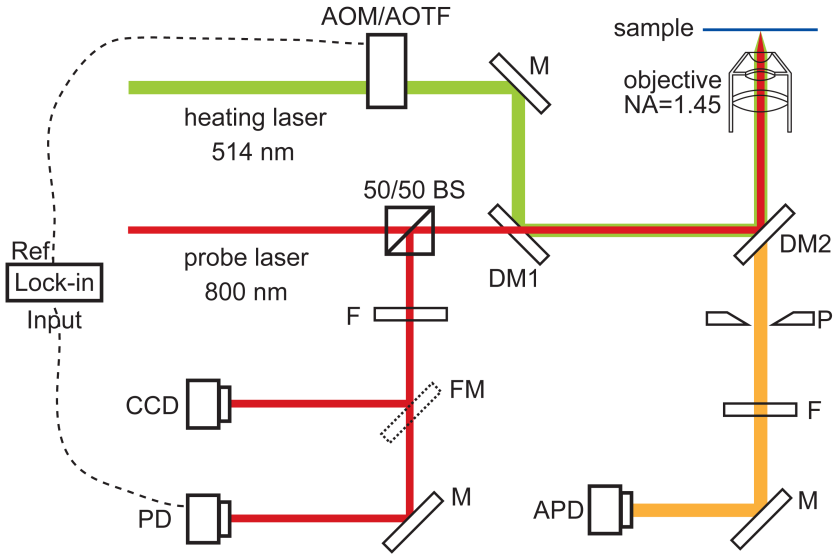

Figure 3.1: Schematic of the experimental setup for simultaneous absorption and luminescence detection. AOM - acousto-optic modulator, AOTF - acousto-optical tunable filter, M - mirrors, FM - flip mirror, DM - dichroic mirrors, F - filter, PD - photodiode, CCD - video camera, APD - avalanche photodetector. Beam expanding telescopes, focusing lenses, polarizers and spatial filters are not shown in this scheme.

3.2.2 Atomic force microscopy

Height distributions of organic nanoparticles were characterized with AFM (Veeco/Digital Instruments, Nanoscope IIIa) equipped with 280 kHz or 70 kHz resonance frequency commercial cantilevers working in tapping mode in air. (see Appendix B, Fig. B.1 for AFM image and height distributions)

3.2.3 Organic nanoparticles preparation

A push-pull triarylamine dye (fvin),[147] insoluble in water, was used for the preparation of the stock solution at a weight percentage ranging within 0.01-1 wt% in acetone. Nanoparticles were formed through reprecipitation of the compound upon addition of the stock solution in Milli-Q water (Millipore Corp.). A volume of 50 μL or 100 μL (giving similar results) of a stock fvin solution was quickly injected into vigorously stirred Milli-Q water (5 mL) (see Appendix B, Fig. B.2 for chemical structure and bulk spectroscopy results).

3.2.4 Sample preparation for optical microscopy

Glass coverslips (Menzel, Germany) were cleaned in the same way as in Section 2.4.1. Clean coverslides were functionalized with 3-aminopropyl triethoxy silane (APTES, Sigma-Aldrich) to facilitate the adhesion of fvin NPs to glass from water solution. Silanization was performed in liquid phase by immersing clean glass slides overnight in a 2% solution of APTES in spectroscopic-grade acetone. The slides were then sonicated in acetone and water, dried and shortly stored prior to use.

Nanoparticles were deposited on these surfaces by one of the following methods: 1) through incubation of 50 μL of NPs solution for 1-20 s on silanized coverslides, followed by gentle washing with 5-7 mL of Milli-Q water. Attention was paid to prevent dewetting of the sample by keeping it immersed in each step of NP deposition. This preparation method is used to prevent sublimation of fvin NPs in dry conditions; 2) through incubation of 50 μL of NPs solution for 1-2 hr, followed by an exchange of solution with pure water or glycerol; or 3) through spin-coating of 50 μL of nanoparticles solution in a 1% PVA matrix at 2000 rpm for 5 s, followed by drying at 4000 rpm for 90 s. The last two options involve dewetting of the sample and can induce pattern formation (see Section 3.3.2).

Optical experiments were performed in a fluid cell with a volume of approximately $50 - 150$ μL filled with glycerol ($> 99.5\%$, spectrophotometric grade).

3.3 Result and discussion

3.3.1 Optical microscopy of organic nanoparticles

We performed photothermal and fluorescence microscopy experiments on individual fvin NPs, which were formed through reprecipitation in water of fvin stock solutions at three concentrations (0.1, 0.5 and 1 wt%) in acetone. Experiments were carried out in two regimes for the heating/excitation power at the sample: low (0.85-1.7 μW), and high (8.5-130 μW) (see Appendix B, Fig. B.3, B.4). While simultaneous photothermal and fluorescence detection of NPs was possible at the high heating power regime, only a few NPs provided detectable photothermal signal at low heating regime. Therefore, most of the fluorescence raster scans at low heating power were accompanied by raster scans where fluorescence and photothermal were simultaneously recorded at high heating power. The photothermal signals acquired at high heating power were then used as a measurement of the NP absorption at low heating power. We were not able to increase the probe power to gain more sensitivity in photothermal detection[90] since we observed a weak two-photon excited fluorescence emission for probe powers higher than 50 mW at the sample. No two-photon excited fluorescence was detected with probe powers up to 40 mW.

Typical photothermal and fluorescence images of nanoparticles deposited in solution on an APTES-modified glass in glycerol, which are simultaneously acquired at high heating power regime, are shown in Fig. 3.2 A and 3.2 B, respectively. Spatially separated spots with different signal strengths, which correspond to individual nanoparticles, are observed in both images. About 1% of spots in raster scans are only visible in photothermal but not in fluorescence images (dashed circle), or in fluorescence but not in photothermal images (dashed box). The absence of fluorescence in some NPs can be explained by the presence of quenching states, originating, for example, from a small concentration of impurities in the solvents or the embedding liquids. The absence of photothermal signal of some fluorescent NPs points to a small number of fvin molecules, or to a fluorescent impurity with a high quantum yield. A different packing of fvin molecules may also lead to higher fluorescence due to inhibition of the radiationless deactivation. The large spread of magnitudes of both signals suggests that nanoparticles have a wide dis-

tribution of sizes, that is, of numbers of fvin molecules. Further analysis of optical signals from NPs was performed on selected spots with a photothermal signal-to-noise ratio (SNR) larger than 5.

The correlation between the fluorescence signal and the photothermal signal for the same individual fvin NPs, first in the low and then in the high excitation power regimes is shown in Fig. 3.2 C. The normalized photothermal signal reveals up to 10 times smaller absorption compared with 20 nm diameter gold nanoparticles (AuNPs) that were used as fiducial markers.

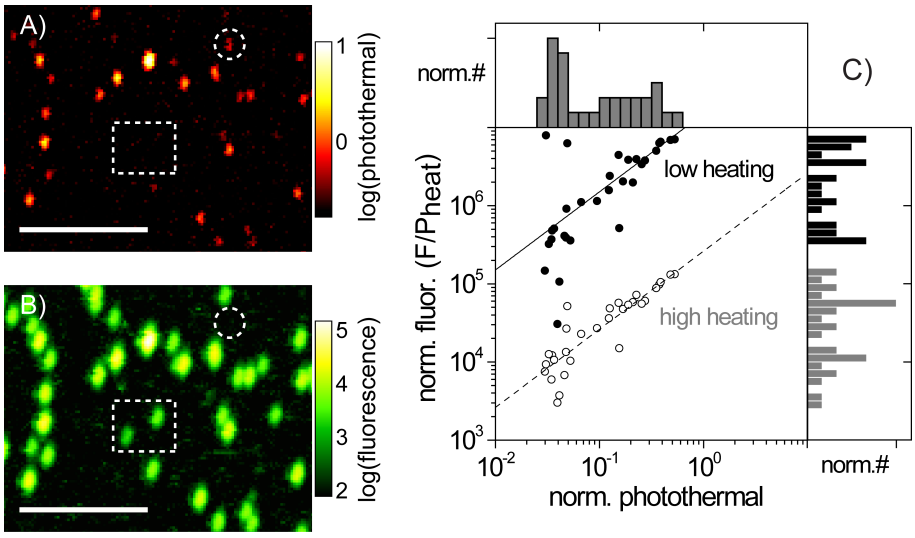

Figure 3.2: Simultaneous A) photothermal and B) fluorescence images of 0.5 wt% fvin NPs deposited on APTES-modified glass in glycerol. The scale bar is 5 μm. A dashed circle highlights a spot observed in the photothermal, but not in the fluorescence image, while a dashed box indicates two fluorescent spots that are not detectable in the photothermal image. The pump power used in the experiment is 106 μW, the probe power is 34 mW. The acquisition time per pixel is 10 ms with 3 ms lock-in integration time for photothermal signal. C) Correlation of normalized fluorescence with photothermal signals consequently measured on the same fvin NPs in two excitation regimes. The fluorescence intensity is in units of 100 counts s^{-1} mW^{-1}. Solid and dashed lines represent linear relationship between signals

Firstly, we observe a rough linear relationship between normalized photothermal and fluorescence signals in both regimes. We conclude that the fluorescence signal scales roughly linearly with the volume of NPs, since we

expect the photothermal signal to be proportional to the number of absorbing molecules, which scales as the NP volume. Indeed, direct correlations of AFM and optical microscopy images would reveal the relationship between a NP's size and its optical signals, similar to studies on individual spherical gold NPs.[156] We tried to obtain such correlations. However, it turned out to be difficult due to sublimation of fvin NPs in air. Secondly, the fluorescence intensity normalized to the excitation power decreases strongly with the excitation intensity (see Appendix B, Fig. B.5). We attribute this decrease of the fluorescence quantum yield to singlet-singlet or singlet-triplet annihilation, that is, to quenching of fvin excited state by other excited states in its surroundings. This phenomenon is well-known in other multichromophoric systems, such as conjugated polymers[158–161] and dendrimers.[162–166] Thirdly, we also note that photothermal and luminescence signals are better correlated at high power than at low power (see Appendix B, Fig.B.4). This observation is consistent with a quenching effect dominated at high power by singlet-singlet annihilation, a bulk effect. At low power, however, we expect quenching to occur mainly through surface and trap effects.

The complex behavior of absorption and fluorescence properties of fvin NPs is further complicated by photobleaching. Fluorescence and photothermal signals bleach upon exposure to the excitation power of 8.5 μW with characteristic times of 0.81 s and 0.84 s, respectively (Fig. 3.3). We find that the bleaching rates do not depend on the initial signal from individual NPs (or nanoparticle sizes), and rise as the heating power increases. At an excitation power of 17 μW, the fluorescence intensity is reduced by a factor of three after a dwell time of about 100 ms. There is negligible bleaching from exposure to probe powers less than 40 mW. In order to minimize the effect of bleaching at a given heating power, we shortened the exposure times in a raster scan to 10 ms per pixel (we had up to 25 pixels per NP in a two-dimensional raster scan).

Then, we calculate the average luminescence quantum yield of fvin NPs in the low heating power regime using 20 nm gold nanoparticles (AuNPs) as fiducial markers for quantitative absorption measurements, and estimating the detection efficiency of the setup to 5%. The quantum yield we find, 0.017, measured on 83 fvin NPs, is in reasonable agreement with the values estimated for ensembles (i.e. 0.013 for suspension of fvin NPs of diameter 85 nm).[55] The apparent QY calculated for more than 1000 NPs in the high

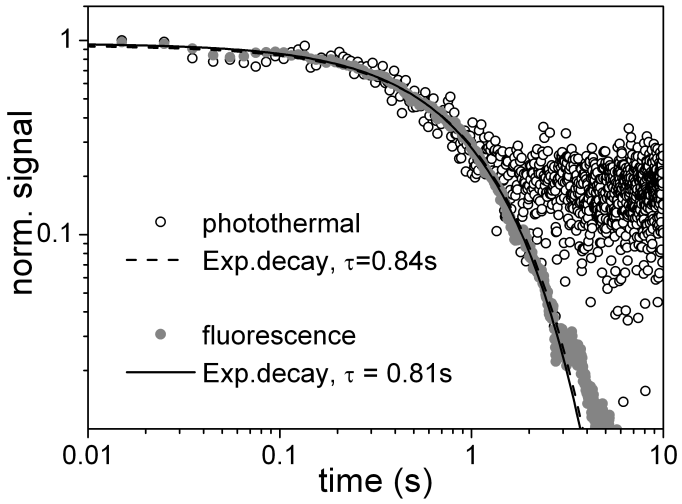

Figure 3.3: Photothermal (○) and fluorescence (●) signal bleaching traces measured on 0.1 wt% fvin NPs on APTES-modified glass in glycerol, shown on a log-log scale. Heating and probe powers were 8.5 μW and 23 mW, correspondingly. Characteristic bleaching times estimated from single exponential decay fits are 0.81 s, and 0.84 s for fluorescence (——) and photothermal (- - - -) signals, correspondingly. The normalized signal of about 0.2 is the background level of the photothermal signal.

heating power regime was found to be much lower, about 1.2×10^{-4} (see Appendix B, Fig. B.4).

Further, the number of molecules in individual fvin NPs is obtained in three different ways, from the photothermal signal, from the luminescence signal, and from the average height of NPs as measured by AFM (Appendix B, Table B.1):

1. The average absorption cross section of fvin NPs at 514 nm is about 180 nm^2. The average isotropic absorption cross section of an individual fvin dye molecule as deduced from the absorption spectrum of fvin NPs in glycerol is estimated to be about 3.2×10^{-3} nm^2 at 514 nm.[167,168] Thus, the average number of fvin molecules in an average fvin NP would be about 6×10^4.
2. We observe a fluorescence count rate of 600 kcounts s^{-1} under the excitation intensity of 1.7 kW cm^{-2} at 514 nm. Assuming a quantum yield of 10^{-2} similar to that of the isolated molecule, we deduce an absorption rate for an individual fvin NP of 1.2×10^9 photons s^{-1}. From

the number of photons absorbed by a single fvin dye molecule, about 1.4×10^5 photons s^{-1}, calculated from the absorption cross section at the same intensity, there would be $\sim 10^4$ molecules on average in a particle.

3. AFM measurements (Appendix B, Fig. B.1) give an average volume of 4×10^5 nm^3 for the NPs, assumed to be spherical.[55] The molecular Van der Waals volume of fvin is 0.85 nm^3. If the molecules are compactly packed in the NP, about 5×10^5 molecules would be present in a single fvin NP.

These independent estimates of about $10^4 - 10^5$ molecules per fvin NP are in reasonable agreement for these three independent methods.

3.3.2 Submonolayers and labyrinth structures formed by organic molecules

Figure 3.4 shows photothermal and fluorescence microscopy images of fvin NPs prepared from 0.025 wt% (Fig. 3.4 A-D) and 0.013 wt% (Fig. 3.4 E) solutions. We observe weak signals from surface structures besides intense spots of individual NPs. For instance, a net-shaped pattern is visible both in photothermal and fluorescence images (Fig. 3.4 A,B). The average photothermal and fluorescence signals of the net-shaped pattern are about 30 times and 500 times smaller than the average of 15 individual NPs in Fig. 3.4 A and 3.4 B, respectively. The characteristic size of meshes is about 5 μm. In some regions we further observe brighter structures like the ones shown in Fig. 3.4 C,D on the right side. The photothermal and fluorescence signals of these structures are about 5 times and 10 times higher than of the net-shaped patterns in the same images, respectively.

Formation of similar patterns via self-organization of molecules/nanoparticles from solution during dewetting has been reported in the literature.[62–64,169–173] Their origin is generally explained by instabilities driven by intermolecular and surface forces at solid-liquid-air interfaces, which are influenced by the solvent, the concentration of nanoparticles, the deposition method, the substrate and the temperature. We attribute the observed morphologies to such instabilities occurring during sample preparation either during the drying step of the spin-coating, or during the sample washing steps. In addition, samples obtained from

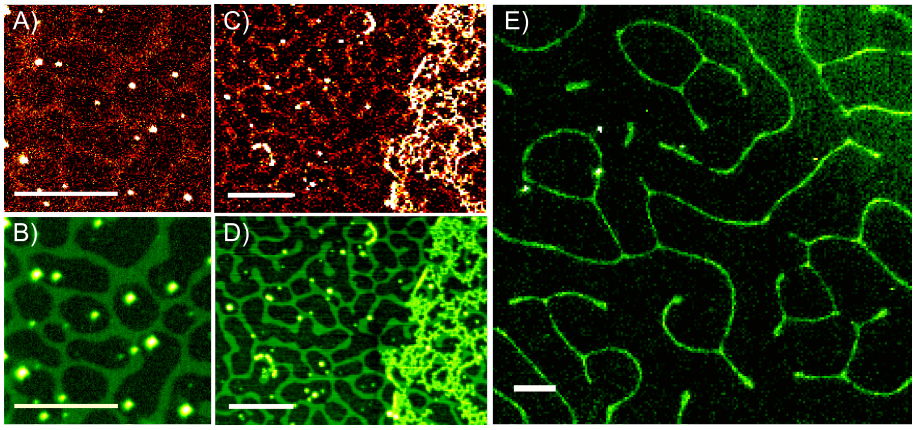

Figure 3.4: Photothermal (A,C) and corresponding simultaneously acquired fluorescence images (B,D) of net-shaped patterns formed on glass from 0.025 wt% fvin NPs in water. The pump power used in the experiment is 43 μW, the probe power is 23 mW. The acquisition time per pixel is 10 ms with 3 ms lock-in integration time for photothermal signal. E) Fluorescence image of a labyrinth pattern formed from 0.013 wt% fvin NPs in 1% PVA/water solution deposited on clean glass through spin-coating. The average fluorescence signal of bright labyrinth walls is 120 kcounts per 10 ms with the SNR of 5. The heating power is 260 μW, the probe power is 23 mW. The acquisition time per pixel is 10 ms. The photothermal signal is not detectable at these experimental conditions. The average spacing between the ridges in the fluorescence image in (E) is about 12 μm. The white scalebar for all images is 10 μm.

low-concentration NP solutions are expected to yield less dense structures in surface-tension-driven dewetting processes.[62] This explanation is supported by the observation of a labyrinth-like pattern with bright fluorescent ridges and the average spacing of about 12 μm (Fig. 3.4 E). These patterns were obtained by spin-coating a suspension obtained by diluting the original suspension of fvin NPs —water precipitated from 0.013 wt percent stock dye solution in acetone— into a 1 wt% solution of PVA in water. This image further resembles the labyrinth patterns formed in confined granular-fluid systems due to instabilities at the fluid-air interface, as described by Sandnes et al.[170] These authors report a notable decrease of the average spacing in the pattern and a slight thickening of ridges with increasing volume fraction of the grains. The features we observe are similar to those, but their characteristic length scale is four orders of magnitude smaller. It will be interesting to investigate whether the physical mechanisms behind pattern

formation are the same on those very different spatial scales.

It would be natural to assume that the structures in Fig. 3.4 A-D, displaying the same brightness everywhere, are formed by one monolayer of the dye. Let us estimate the number of molecules in the net-shaped patterns, assuming those are formed by fvin molecules that give rise to photothermal and fluorescence signals. If all molecules in the laser spot would be concentrated in a nanoparticle, the quantitative photothermal measurement would give an absorption cross section of $0.5 - 3.2$ nm^2. This corresponds to 150-1000 molecules, based on the absorption cross section of an individual molecule, 3.2×10^{-3} nm^2 (Appendix B, Table B.1). This number is about two to three orders of magnitude smaller than the expected number of fvin molecules packed in this area in a monolayer. Although the spread of the absorbing molecules over the whole laser spot may weaken their photothermal signal, this density appears much lower than that of a packed monolayer.

The quantitative interpretation of the fluorescence images obtained in the high heating power regime is rather difficult due to the unknown morphology of the molecular organization of the pattern and to a combination of quenching and photobleaching. However, the luminescence count rate per molecule appears larger when molecules are compactly packed in a spherical fashion than when they are homogeneously distributed. Similar to the experiments with fvin NPs, both patterns and aggregates show degradation of photothermal and fluorescence signals with prolonged illumination or after performing several scans in the same sample area.

3.4 Conclusions

We have investigated the organic nanoparticles prepared by reprecipitation of a triarylamine dye, fvin. We have studied the optical absorption and emission properties of these spherical NPs by means of combined fluorescence and photothermal (absorption) microscopy at the single-particle level. We have found a roughly linear correlation of normalized fluorescence and photothermal signals at low and high excitation regimes. In the high heating power regime nanoparticles show an apparent fluorescence quantum yield 100 times lower than in the low heating power regime. We attribute this high-power quenching to singlet-singlet or singlet-triplet annihilation at the high concentration of excitations, presumably assisted by exciton migration. Sim-

ilar quenching effects are observed in many multichromophoric systems. We have calculated the (low-power) fluorescence quantum yield of individual fvin NPs to be about 10^{-2}, which is in good agreement with results obtained earlier on ensembles. Furthermore, we used photothermal microscopy, fluorescence microscopy and AFM for quantitative measurements of the average number of molecules in individual NPs. Results from these three independent methods reveal an average number of molecules per nanoparticle to be $10^4 - 10^5$. Finally, we report the formation of patterns with complex morphologies from fvin molecules and NPs, which are probably driven by dewetting upon sample preparation.

This work presents a first study of the optical properties of individual organic nanoparticles, which are different from conjugated polymers, inorganic, and metal nanoparticles. It illustrates the potential of correlated absorption and fluorescence studies for the investigation of such complex systems.

Acknowledgements

We thank Prof. Thomas A. Witten for helpful discussions of labyrinth patterns, as well as Dr. Federica Galli and Prof. Tjerk Oosterkamp for their support with AFM equipment in the BioAFM Lab (Leiden Institute of Physics). We acknowledge financial support by ERC (Advanced Grant SiMoSoMa). This work is a part of the research program of the "Stichting voor Fundamenteel Onderzoek der Materie", which is financially supported by the Netherlands Organization for Scientific Research (NWO).

CHAPTER 4

Correlated absorption and photoluminescence of single gold nanospheres

We perform simultaneous absorption (photothermal) and fluorescence detection of gold nanospheres with diameters of 80, 60, 40, 20, 10, and 5 nm. We unambiguously identify the same individual nanoparticles (NPs) over large areas (>400 μm^2) by means of atomic force microscopy (AFM) and optical absorption (photothermal) microscopy. We correlate the height of NPs measured with AFM with absorption and fluorescence signals from the same individual NPs. That allows us to compare their brightness and estimate their fluorescence quantum yield at the single NP level. We also demonstrate a laser-induced enhancement of luminescence of 20 nm gold nanospheres. Simultaneous absorption and fluorescence detection of gold nanospheres makes them attractive for biosensing and multidimensional tracking applications where durable and nontoxic labels and complementary signals are required.

The contents of this chapter are based on:
A. Gaiduk, M. Yorulmaz, and M. Orrit, "Correlated absorption and photoluminescence of single gold nanoparticles", ChemPhysChem **12**, 1536-1541 (2011) and A. Gaiduk, P. Ruijgrok, M. Yorulmaz, and M. Orrit, "Making gold nanoparticles fluorescent for simultaneous absorption and fluorescence detection on the single particle level", Phys. Chem. Chem. Phys. **13**, 149-153 (2011)

4.1 Introduction

Gold nanoparticles (NPs) of various sizes and shapes, and with different surface properties, are commonly used as labels for optical microscopy.[133,134,174,175] These labels can be detected individually either by their scattering, absorption, or photoluminescence.[23,38,40–42,75,87,91,149,150,176–179] Although the quantum efficiency of the photoluminescence of gold NPs is very low, their large absorption cross section makes them detectable, opening possible applications. Earlier efforts to measure and understand the emission of gold NPs have rested on ensemble measurements on NPs of various sizes and shapes. A photoluminescence efficiency of 10^{-6} was reported for $4 - 80$ nm (diameter) spherical NPs in water.[180] Different theoretical descriptions have been proposed to understand the emission of AuNPs.[180–182] In essence, the electron-hole pairs created by optical excitation rapidly relax towards the Fermi sea level, but can still recombine radiatively with a low probability. Coupling of electrons and holes to the collective plasmon modes of a NP can enhance their radiative recombination rate and explain that the luminescence spectrum of gold NPs displays the same plasmonic resonances appearing in their absorption spectrum. Dulkeith et al.[180] have argued that, in the dipole approximation, the radiative coupling scales as the volume of the particle, whereas the screening factor effect reducing coupling of individual charges to plasmon modes scales as the inverse of the volume. The combination of these two effects explains the experimental observation that the quantum yield of gold NPs does not significantly depend on size for diameters between 5 and 50 nm, for which the dipole approximation applies. More recently, it has been shown that the presence of an imbedding/stabilizing medium and surface modification can influence the observed fluorescence signals.[155,183–186].

Photothermal microscopy is one of the methods allowing background-free detection of absorbers at room temperature,[38,39,90,95,97,98,187,188] with a sensitivity reaching the single-molecule level (see Chapter 2).[82] Further developments of this technique, including photothermal correlation spectroscopy,[124,189,190] photothermal tracking,[28] wide-field photothermal detection,[191] and its combination with fluorescence microscopy make photothermal microscopy a valuable tool in a large variety of applications. In this work, we simultaneously detected absorption and luminescence signals from the same single spherical gold NPs, which allows us to estimate directly their lu-

minescence quantum yield.[155] We also checked the sizes of these same NPs by correlating their optical images with atomic force microscopy (AFM) images. We used commercial gold NPs of various diameters providing both absorption (photothermal) and fluorescence signals. We compare their photoluminescence quantum yield to previously reported results from ensemble experiments. We also show, in a separate experiment, a laser-induced enhancement of luminescence of 20 nm diameter gold NPs. We conclude that individual small gold NPs with diameters as small as 5 nm could serve as nonbleaching labels for luminescence detection and tracking, and shortly discuss further perspectives of simultaneous photothermal and fluorescence detection of single gold NPs of various shapes.

4.2 Experimental section

4.2.1 Absorption (photothermal) and fluorescence microscopy

The absorption of individual NPs was measured by photothermal contrast. Photothermal detection is described in detail in Chapter 2. The experimental setup for simultaneous absorption and fluorescence microscopy was home-built around an inverted optical microscope, Olympus IX71, equipped with an Olympus 60× oil immersion objective (NA=1.45) and the simultaneous absorption and luminescence detection was performed as described in Chapter 3.

Briefly, correlated absorption and luminescence signals were detected while nanospheres with diameters of 80, 60, 40, 20, 10, and 5 nm were excited by the heating beam at 514 nm which was provided by an Ar-Ion laser (Coherent Innova 300) and modulated at a frequency of 740 kHz. The dissipated energy gives rise to a time-dependent temperature gradient around the nano-absorber. The maximum temperature rise in steady state on the surface of the particle is, $\Delta T = \frac{\sigma_{abs} I_{heat}}{4\pi\kappa R}$ where σ_{abs} is the absorption cross section of the NP, I_{heat} is the intensity (irradiance) of the heating laser, κ is the thermal conductivity of the medium around the NP, and R is its radius.

For photothermal detection, the probe beam was produced by a Ti:sapphire laser (S3900 s, Spectra Physics) which operated at 800 nm for this experiment. The small change in the detected probe intensity due to photothermal effect was isolated by using a lock-in amplifier to provide the

photothermal signal.

The luminescence detection was performed in the backward direction by spectral separation of the luminescence signal at the dichroic mirror (AHF z532/NIR). The luminescence signal was additionally spatially filtered by a 50 μm confocal pinhole and spectrally filtered by a set of bandpass filters (AHF 615/150 and Omega 595/100) and detected by an avalanche photon-counting module (SPCM-AQR-16).

In an independent experiment, we study a laser-induced method to enhance the luminescence signal of 20 nm diameter gold nanospheres. For the initial investigation of the observed luminescence enhancement, 532 nm laser light (Shangi Lasers) was used as the heating beam and the intensity of the laser was modulated at 740 kHz. 790 nm laser light (Mira, Coherent) was employed as the probe beam. For luminescence imaging, the heating beam was sent to the back-aperture of the microscope objective after it was reflected off from a 30/70 (Reflection/Transmission) beamsplitter. The back-reflected signal collected by the same microscope objective was sent through the same 30/70 beamsplitter. Then, the luminescence of 20 nm diameter gold nanospheres was spectrally selected by a set of bandpass filers (AHF 615/150 and Omega 595/100) and directly detected by an avalanche photon counting module (SPCM-AQR-16). There was no pinhole in the fluorescence detection path to suppress fluorescence background from out-of-focus planes. Moreover, the background signals of luminescence images was higher than the background signal of the images obtained by using the former described setup. Therefore, the intrinsic luminescence of gold nanospheres was not detectable in this case.

4.2.2 Atomic force microscopy (AFM)

We used an atomic force microscope (Digital Instruments) in tapping mode equipped with cantilevers with a resonance frequency of 280 kHz. We recorded AFM images in air to characterize the topography of our samples.

4.2.3 Sample preparation

Samples of colloidal suspensions of gold NPs with diameters of 80, 60, 50, 40, 30, 20, 10, and 5 nm (British Biocell International) were prepared by dilution in ultra-pure water at volume ratios of 1:1, 1:4, 1:4, 1:8, 1:20, 1:20, 1:150, and

1:1000, respectively. Approximately 50 μL of the suspension were deposited on the surface of cleaned glass immediately after filtration through a 450 nm porous membrane (except for the 80 nm diameter NPs) and spin-coated at 2000 rpm for 5 s, followed by drying at 4000 rpm for 90 s.

Glass coverslides (Menzel, Germany) were cleaned in several steps by sonication for 20 min, successively in a Hellmanex (Hellma) solution in water (2%), in acetone, in ethanol (both 96%purity), and in Milli-Q water after each cleaning step. The surfaces were modified with 3-aminopropylthriethylethoxysilane (APTES, Sigma-Aldrich) by immersing clean coverslides in APTES solution in acetone (2%) overnight. Experiments were performed in a fluid cell (approx. $50 - 150$ μL volume). We used glycerol (>99.5%, spectrophotometric grade) as the photothermal transducing fluid in all experiments. The background fluorescence of glycerol was too high to detect the luminescence of the smaller gold beads (5 nm). Their luminescence and photothermal signals were measured in air and calibrated with those of larger NPs (20 nm) under the same conditions.

4.3 Results and discussion

4.3.1 AFM characterization of gold NPs

The results of our AFM studies of commercial spherical gold NPs of various sizes are shown in Fig. 4.1 and Table 4.1. The mean values of measured heights are in good agreement with the specified diameters. The spreads of heights for individual NPs of 20, 40, 50, 60, and 80 nm diameter are about 11% (rms), which is close to 8-10 percent specification values. However, larger variations are observed for NPs with nominal diameters of 5, 10, and 30 nm. In particular, for the NPs with specified diameter of 30 nm a distinct population of smaller NPs leads to a 19% variation of the measured height. The differences between the actual mean values and the nominal diameters can be explained by the nonspherical shapes of the NPs. Because our AFM images were recorded at a relatively low resolution over large sample areas in order to correlate them with optical images, they did not allow us to retrieve the detailed nonspherical shape of NPs in the present experiments.

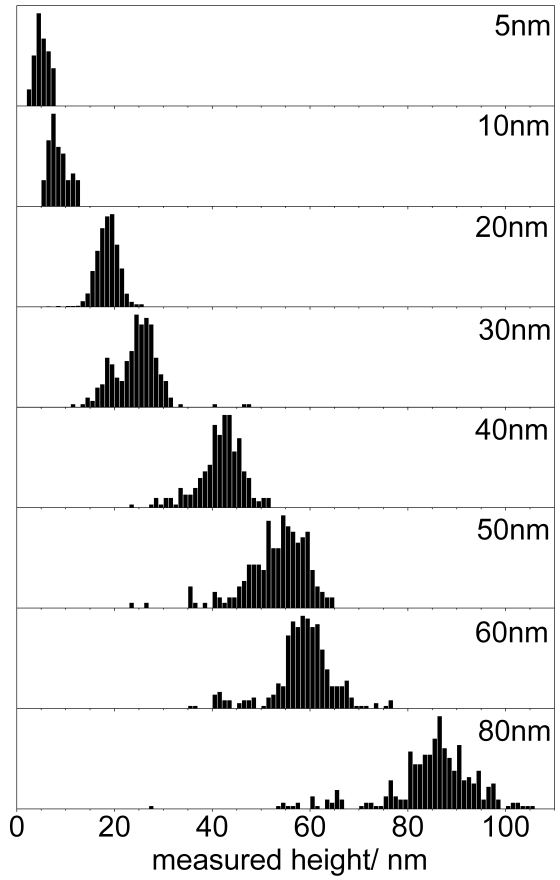

Figure 4.1: Distribution of the heights of commercial spherical gold NPs measured by AFM on APTES-modified glass surfaces. The NPs were imaged in tapping mode in air.

4.3.2 Correlation of AFM and optical microscopy results on gold NPs

To correlate the AFM images with those obtained in optical microscopy, we used a cross as a position reference visible in both types of microscopy techniques. This cross was made by scratching the glass coverslip's surface prior to cleaning and to surface modification. The results of the overlap of images obtained by the scanning-probe and optical absorption microscopy for the sample of 60 nm diameter gold NPs is shown in Fig. 4.2. It is straightforward to find patterns of perfect overlap, enabling unambiguous identification of

the topographical signals of individual nanospheres (white dots in the AFM image) and of their optical absorption signals (red dots). However, the overlap of the two images is not perfect over the whole scanned area due to the hysteresis and to the thermal drift of the AFM scanner during data acquisition time (about 30 min).

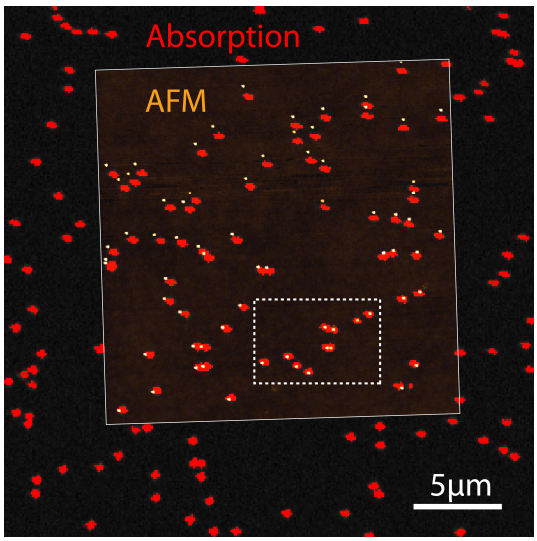

Figure 4.2: Overlap of the optical absorption microscopy image (area 900 μm^2) and of an AFM image (area 400 μm^2 enclosed in solid box) of a sample with 60 nm diameter gold NPs on APTES-modified glass surface. The absorption was measured in glycerol with powers of 29 μW and 2.3 mW for the heating and probe beams, respectively. White dots are individual NPs imaged with AFM and red spots are their optical absorption images. Patterns in NP locations provide an unambiguous correlation between these images. Thermal drift and nonlinearities in the AFM scanner (which has no position feedback) cause a mismatch in the precise location of individual NPs over the whole AFM field. The dashed box highlights an area with good overlap.

4.3.3 Correlation of absorption and luminescence of individual gold NPs

We simultaneously measured absorption (photothermal) and luminescence signals of individual gold NPs (diameters 10, 20, 40, 60, and 80 nm) on an APTES-modified glass surface in glycerol. The AFM and photothermal absorption results are presented in Fig. 4.3 as a scatter plot, where particles of

Table 4.1: Results of the AFM and optical microscopy measurements on commercial gold NPs spin-coated on an APTES-modified glass surface. The height of NPs (H) was measured in tapping mode in air for gold NPs with specified diameters (D). Absorption (photothermal, PTA) and fluorescence microscopy experiments were performed in glycerol, unless specified. The quantum yields (QY) were calculated using results of photothermal microscopy (QY from PTA) and AFM (QY from H).

D [nm]	H [nm]	# NPs	QY from PTA	QY from H	# NPs
5	5.2 ± 1.4	76	$(3.5 \pm 1.4) \times 10^{-7}$	$(3.1 \pm 1.7) \times 10^{-7}$	40 (air)
10	8.5 ± 2	58	$(3.1 \pm 1.2) \times 10^{-7}$	$(3.4 \pm 1.4) \times 10^{-7}$	104
20	18.5 ± 2.3	1811	$(3.7 \pm 1.4) \times 10^{-7}$	$(2.7 \pm 1.4) \times 10^{-7}$	123
			$(1.9 \pm 0.8) \times 10^{-7}$	$(2.2 \pm 1.0) \times 10^{-7}$	107 (air)
30	24.4 ± 4.7	241	–	–	–
40	41.6 ± 4.7	238	$(8.3 \pm 3.3) \times 10^{-7}$	$(3.2 \pm 2.5) \times 10^{-7}$	178
50	53.1 ± 6.6	199	–	–	–
60	58.5 ± 6.4	350	$(9.2 \pm 3.7) \times 10^{-7}$	$(3.0 \pm 2.5) \times 10^{-7}$	218
80	84.7 ± 9.7	323	$(3.3 \pm 2.2) \times 10^{-7}$	$(1.4 \pm 3.9) \times 10^{-7}$	282

different nominal sizes are represented by dots of different colors. As Fig. 4.3 shows, the photothermal signal scales linearly with the volume of NPs deduced from the AFM height. This linear dependence was expected and reported previously.[38,90,95] The linear correlation is well obeyed for particles smaller than 40 nm. We also note a larger spread of photothermal signals for 80 nm NPs. We attribute this spread to a distribution of the local heat transfer parameters (heat conductivities, contact areas) around each individual particle.

Figure 4.4 A presents a scatter plot of luminescence intensity correlated with absorption signal. Particles of different nominal sizes are represented by dots of different colors. The powers of the heating and probe lasers were adjusted in experiments to keep a comparable temperature rise (less than 20 K) at the surface of NPs of different diameters to eliminate laser-induced effects on luminescence (see Section 4.3.4). For all particle sizes, the photothermal signal-to-noise ratio was more than 10 with 3 ms integration time. For luminescence, the signal-to-background ratio was larger than 2 and the signal-to-noise ratio higher than 10. The luminescence signal of smaller NPs (5 nm diameter) was too weak to measure against the fluorescence background of glycerol. Therefore, these particles were measured in air (Fig. 4.4 B), where their luminescence was detected with a signal-to-background ratio of 1 and a

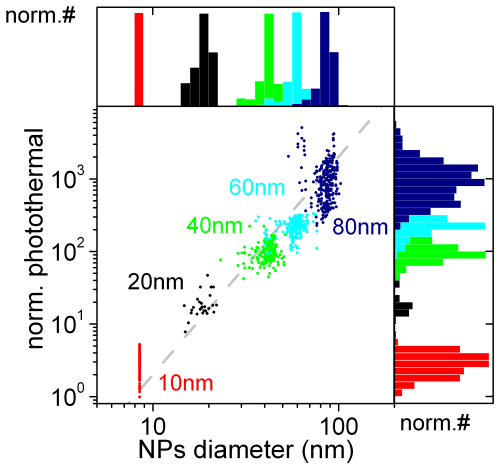

Figure 4.3: Normalized optical absorption (photothermal) signals from gold NPs of different sizes spin-coated on an APTES-modified glass surface in glycerol as a function of their size, as measured by AFM. As we could not correlate AFM with photothermal contrast for 10 nm NPs, we used the average AFM diameter in the plot. The gray line represents a linear relationship between the photothermal signal and NP volume.

signal-to-noise ratio of 5 to 10. The photothermal signal-to-noise ratio of 5 nm diameter NPs in air was more than 10 with 100 ms integration time. The collection efficiencies for the luminescence and photothermal properties differ in air and glycerol. Therefore, we repeated these optical microscopy experiments for a number of 20 nm diameter NPs in air as a reference to calibrate the luminescence and photothermal signal of 5 nm NPs. For these 20 nm NPs, the luminescence signal-to-background ratio was 5, the signal-to-noise ratio was larger than 10, and the photothermal signal-to-noise ratio larger than 30 with 3 ms integration time.

As shown in Fig. 4.4 A, the luminescence roughly scales linearly with the photothermal signal as reported previously by Dulkeith et al.[180] This linear relation is well followed from 5 nm to 20 nm. However, the luminescence signal appears somewhat larger for larger diameters and tends to decrease for very large particles, 80 nm and above. The scaling of the luminescence signal with the volume of the particles instead of their surface area indicates that this luminescence does not arise from surface states or from impurities at the NP's surface and supports the mechanism of particle plasmon emission pro-

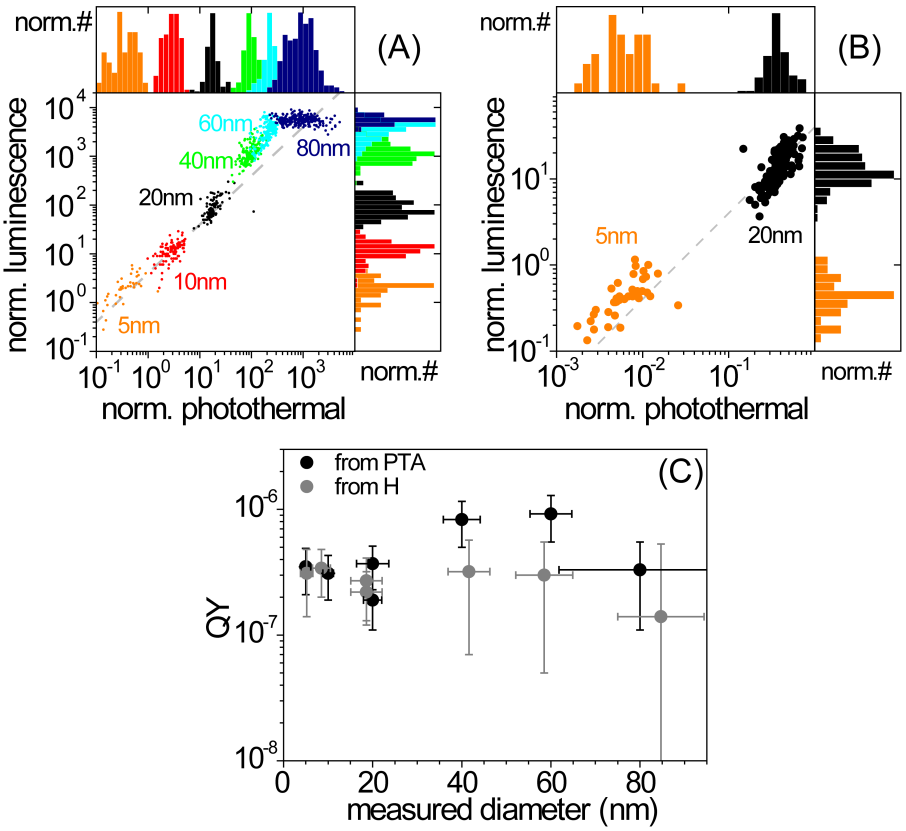

Figure 4.4: A) Combined normalized luminescence and absorption (photothermal) signals from gold NPs of different sizes spin-coated on an APTES-modified glass surface in glycerol. Gray lines [here and in (B)] represent linear relationships between optical signal and NPs volume. B) Normalized luminescence and absorption (photothermal) signals from gold NPs of 5 and 20 nm diameters spin-coated on APTES-modified glass surface in air. Dots represent values for individual NPs. The histograms of signals are shown in the top and right-side axes, correspondingly. C) Luminescence quantum yield (QY) as a function of measured diameters of gold NPs. Estimation of the QY is either based on absorption measurements of size of NPs via photothermal contrast (black dots), or on the size of NPs measured by AFM (gray dots). Error bars in QY represent the spread of values for individual NPs. Error bars for NPs diameters for black and gray dots are defined by the spread of diameters estimated from photothermal microscopy experiments and measured in AFM experiments, respectively

posed by Dulkeith et al.[180] Thus, this luminescence is different from the laser-induced luminescence,[155] which we may attribute to impurities produced at the particle surface by (photo-)chemical reactions (see Section 4.3.4). Furthermore, the good agreement of measurements for 5 nm and 20 nm particles in glycerol and in air is also consistent with a luminescence mechanism involving volume instead of surface states. The signals of 80 nm diameter NPs (Fig. 4.4 A) appear to deviate from the general linear trend of the absorption-luminescence correlation. The luminescence intensity seems to reach a saturation value. This behavior of the luminescence of the largest particles is not clear to us. It may have one or more of the following origins: 1) The nonspherical, ellipsoidal shapes of NPs influence spectrum and magnitude of their absorption and luminescence. Whereas these effects appear to average out for the smaller particles, they may bias the distribution for the larger particles. 2) Large NPs cannot be described within the dipole approximation any more. Multipolar terms can lead to deviations from the simple linear luminescence-absorption scaling. For example, reabsorption of plasmon radiation in the core of large particles could reduce their luminescence yield. 3) Larger particles may have specific defects, facets, or impurities which may modify their luminescence yield with respect to smaller particles.[192]

The luminescence quantum yield (QY) from individual NPs is calculated taking into account the excitation (heating) laser power, luminescence signal, the absorption cross section of a NP, and the detection efficiency, estimated to 5% for our setup. A more accurate measurement of the luminescence detection efficiency of the setup could lead to small changes of the quantum yield (see Appendix C). The absorption cross section in turn is estimated in two ways based on: 1) the absorption (photothermal) signal of NPs which is proportional to the volume in the approximation of Mie scattering,[42] or 2) the height of NPs measured in AFM experiments, which gives the diameter of NPs, assuming a perfect spherical shape. The particles in the optical scans which were outside the AFM scans were also included in the plots, but were assigned the average height measured by AFM. The results of the estimation of QY are shown in Fig. 4.4 C and in Table 4.1. The luminescence QY is found to be almost independent of the size of NPs and estimated to be a few 10^{-7}, in fair agreement with values reported previously.[180] Note that the quantum yields deduced from photothermal values and from AFM values are slightly different for particles larger than 40 nm.

4.3.4 Laser-induced enhancement of luminescence from gold nanospheres

In previous sections of this chapter (Sections 4.3.2 and 4.3.3), we study the intrinsic luminescence of spherical gold nanospheres with sizes ranging from 5 to 80 nm in diameter. In this section, we describe a simple laser-induced method to make 20 nm diameter gold nanospheres more luminescent. Our method relies on the excitation of nanopsheres on an individual basis with a focused laser beam at high powers. In the following, we provide a detailed description of the method, quantify the effect and briefly comment on possible mechanisms that may be responsible for the observed enhancement.

The results of enhancement of gold nanosphere's luminescence are shown in Fig. 4.5 A-I. Time-marks next to each row of images indicate the time since the start of the experiment. Three single 20 nm diameter gold NPs are observed in Fig. 4.5 A, situated more than 500 nm apart. The photothermal signal-to-noise ratios are higher than 300 with 0.26 mW heating power (532 nm) and 40 mW probe power (790 nm) at the sample, and integration time (Δt) of 1 ms. The corresponding temperature elevation at the NP surface caused by the heating light is about 23 K. The absorption of the probe light provides an additional non-modulated temperature rise of 9 K. The full-width-at-half-maximum (FWHM) of the Gaussian fit of the shape of photothermal signal are 220 nm and 260 nm (for vertical and horizontal directions, respectively). The simultaneously acquired confocal luminescence image (Fig. 4.5 B) shows only the background signal in glycerol. The vertical lines observed in the luminescence image (along the fast scan axis) are due to diffusing fluorescent impurities in glycerol. The overlap of the simultaneously detected photothermal Fig. 4.5 A and luminescence Fig. 4.5 B signal is shown in Fig. 4.5 C with the red and green color representing the photothermal and luminescence signal, respectively. The intrinsic photoluminescence signals of 20 nm diameter spheres were not visible in this experiment because of the high fluorescence background signal of the batch of glycerol which was used as immersion liquid.

As a next step, we focus laser beams on the central NP and perform an experiment similar to the one depicted in Fig. 4.6. The graph shows simultaneously recorded photothermal (red) and luminescence (green) time-traces normalized to the heating power. The top part of the graph illustrates how

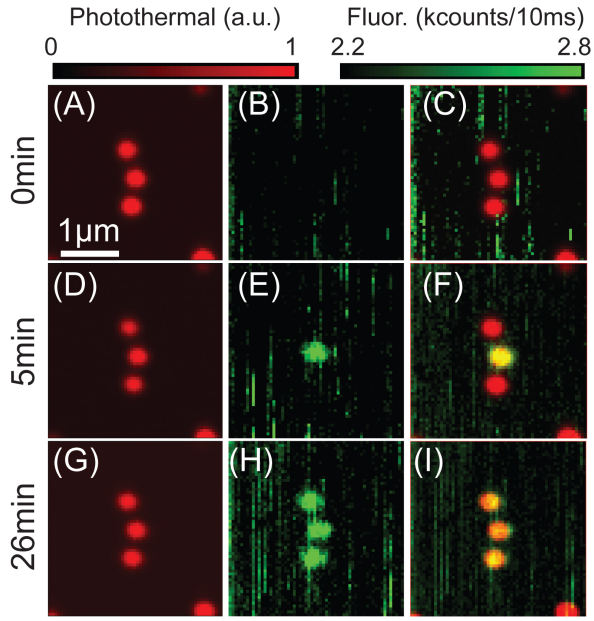

Figure 4.5: Photothermal (A, D, G) and corresponding luminescence (B, E, H) raster scan images simultaneously obtained on 20 nm diameter gold NPs on glass surface in glycerol. (C, F, I) shows the overlap of the two signals. Time-marks next to each row indicate the time since the start of the experiment. Vertical lines (along fast scan axis) in luminescence images originate from diffusing fluorescent impurities in glycerol. There is no detectable luminescence observed from single NPs in (B), while (E) demonstrates bright luminescence from the treated central NP (Fig. 4.6) and others remain non-fluorescent. Finally all three nanospheres have been made fluorescent, as shown in (H). Experimental parameters for raster scans are $P_{heat} = 0.26$ mW and $P_{probe} = 40$ mW at the sample, $\Delta t = 1$ ms, ΔT_{surf} due to heating light (532 nm) is about 23 K.

the heating power is varied in the experiment. The temperature rise on the surface of the nanospheres (ΔT_{surf}) and the photothermal signal depend linearly on the heating power. At approximately 98 s, the heating power has been increased and, with it, the temperature of the NP. The increase of the heating power (514 nm) from 0.26 mW up to 0.85 mW leads to a temperature rise from 17 K up to 57 K on the surface of the NP. At the same time a dramatic increase of the luminescence signal is observed, as well as luminescence fluctuations. The high luminescence signal remains after the heating power is reduced back to 0.26 mW.

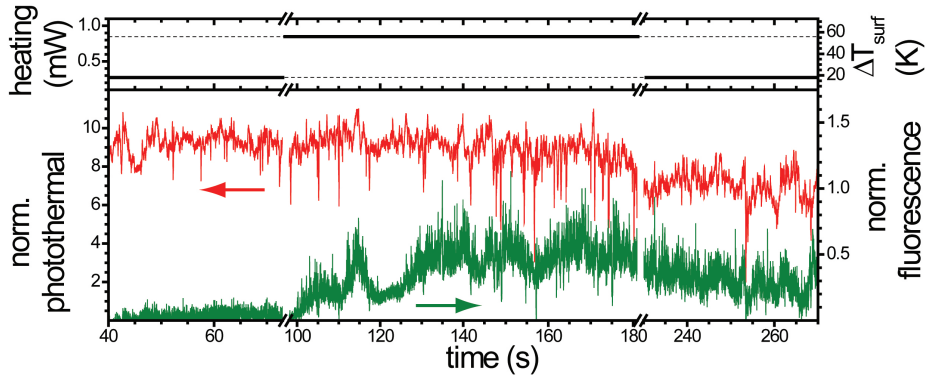

Figure 4.6: A time trace illustrating the appearance of the luminescence signal from a single 20 nm gold NP. An increase of the heating power (top, black) at the first axis break (98 s) leads to the temperature rise at the NP. A significant change in luminescence signal and its fluctuations are observed at the same time (green). At the second axis break (182 s) the heating power is reduced to its starting value. The normalized luminescence signal remains above its background level at the start. Due to the mechanical drift in the setup (about 20 nm min^{-1}) the photothermal signal (red) is about 20% smaller after 230 s. The wavelength of the heating light is 514 nm.

It is important to note that simultaneous photothermal and luminescence raster scans reveal no change in the photothermal signal (Fig. 4.5 D). The unaltered absorption of light suggests no fragmentation of the particle has occurred. A fragmentation of similar size NPs is previously reported with the intense pulsed laser light, where the temperatures rise above 1000 K.[193] We use moderate heating with CW lasers with an order of magnitude lower temperature elevation (less than 100 K) at the surface of NPs. The absence of NPs fragmentation is supported in independent experiments by SEM imaging after the studies of the vibrations of individual gold NPs, where temperature elevation about 300 K is used.[176,194] In contrast to the unchanged absorption, the confocal luminescence image (Fig. 4.5 E) shows a clear change. A fluorescent spot appears with a signal-to-background ratio of 1.4, signal-to-noise ratio of more than 50, and a full width at half-maximum (FWHM) of 300 and 340 nm (for vertical and horizontal directions correspondingly). The spatial overlap of the two images is shown in Fig. 4.5 F with the yellow colour encoding the overlap of photothermal and luminescence signals. The same effect is observed on other NPs in the sample (about 50 NPs tried) and further demonstrated in Fig. 4.5 G, H, I, where the other two NPs in the

image are made fluorescent in the same manner as the middle one. The obtained luminescence persists under illumination for a long time (tested up to 10 min), although its intensity fluctuates. In the particular experiment presented in Fig. 4.5 luminescence was also detected as particles were revisited after 148 min.

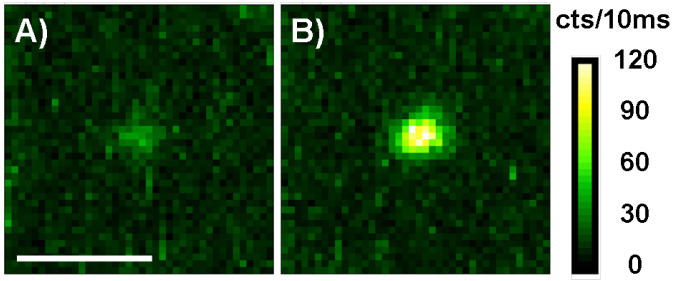

Figure 4.7: Luminescence images of the same 20 nm diameter gold nanosphere A) before and B) after employing the laser-induced treatment of the nanosphere to enhance its luminescence. The excitation power is $P_{heat} = 0.26$ mW at 514 nm. The color scale shows the luminescence count-rate and is the same for both images. The scale bar is 1 μm.

To further quantify the enhancement of the luminescence by the laser-induced method, we repeated the above described experiment on the setup we used to record luminescence images of gold nanoparticles by their intrinsic luminescence (see section 4.3.3). Figure 4.7 shows the luminescence images of the same 20 nm diameter nanosphere. Fig. 4.7 A shows the intrinsic luminescence of the nanosphere, whereas Fig. 4.7 B corresponds to the signal of the same nanosphere after it was treated in the same way as for the nanosphere of Fig. 4.6. The luminescence signal of the nanosphere, under the same excitation and detection conditions, is increased from about 30 cts/10 ms to 110 cts/10 ms by employing the laser-induced luminescence enhancement method. We observe an increase in the luminescence of the nanosphere by a factor of 3 to 4 times. This enhancement factor was confirmed by repeating this measurement on several tens of 20 nm diameter gold spheres.

The enhancement of luminescence upon illumination with laser can be explained by the modification of the surface of NPs, caused by thermal processes, photochemical processes,[195–197] or a combination of those. A temperature-mediated part of the observed enhancement mechanism is sup-

ported by our observation of the enhancement of luminescence after an exposure to only the probe light with a power larger than 150 mW at the sample. In contrast, no enhancement was seen with heating light power kept as low as 0.26 mW for times longer than 200 s, or with the probe light only with powers below 100 mW for times longer than 100 s. However, both observations can not directly exclude a possible effect of the laser illumination on the observed enhancement. We also observe luminescence appearance in pentane and hexane, organic solvents that are chemically different from glycerol. This luminescence enhancement effect is not observed in water, although enhanced luminescence of gold NPs in glycerol remain when glycerol is exchanged with water. The simplest temperature-activated chemical reactions in the above-mentioned solvents would first lead to saturated and therefore non-fluorescent products. A high enough temperature elevation at the surface of NPs, however, can result in the formation of more and more complex unsaturated products, which may decorate the NP and generate luminescence. Still, in order to eliminate the effect of laser light on the observed enhancement, a separate experiment where nanospheres were kept in a heat bath to increase their surface temperature by about 40 degrees should be performed. However, localized excitation and ensemble (macro) heating would be different. An additional complication is the possible catalytic role of the gold surface, which may act in more specific ways than just a local "frying pan".[198–200] Hereafter, we speculate about possible surface chemistry on NPs in glycerol, which requires further investigation: (i) thermal decomposition of glycerol or residual fatty acids in glycerol *, (ii) formation of a reactive acrylic acid aldehyde (acrolein, $H_2C = CH - CHO$ obtained in thermal decomposition of glycerol by dehydration in the presence of a catalyst . Recently, reversible and irreversible temperature mediated reactions of glycerol and citric acid[201] have been studied with the method of differential scanning calorimetry (DSC) in the temperature range of $20 - 220^{\circ}C$. The work reports irreversible esterification and glycerol citrate polyesters formation. Also, Ruppert et al.[202] have studied a selective etherification of glycerol to linear, branched and cyclic diglycerols, and triglycerol in the presence of alkaline earth metal oxides.

*Communication with Sigma-Aldrich

4.4 Conclusions

Herein, we have correlated three observation methods (AFM topography, optical photothermal absorption, and optical photoluminescence) on individual gold nanospheres of different sizes, from 5 to 80 nm. The AFM height signal gives a very good indication of the particle's volume, as deduced from absorption properties, at least for large enough particles. Photothermal detection is much easier than AFM for small particles (5 nm and lower), particularly when those have to be found over large sample areas.

Our measurements confirm that the photoluminescence signal scales roughly as the volume of the NPs, and that the luminescence yield is therefore roughly independent of size, from 5 to 60 nm. The value of the yield is about 3×10^{-7} (subject to a possible small calibration error, see Appendix C), in good agreement with previous determinations. We also find that the yield appears to decrease for even larger particles (larger than 80 nm in diameter).

We also demonstrate a simple method to make commercial 20 nm diameter gold NPs more luminescent. The luminescence enhancement appears after the laser excitation of the NPs at moderately high power, which leads to a transient temperature elevation at the surface of NPs and modification of their surface properties. We observe this effect in different solvents (glycerol, hexane, pentane). We shortly speculate on the origin of the observed enhancement in order to stimulate research and we suggest that temperature-assisted (photo-)chemical reactions lead to a complex modification of the surface of gold NPs. However, the mechanism which is responsible for the laser-induced enhancement of luminescence still remains a subject to study. In order to identify and separate between different mechanism, more rigorous studies (e.g. Raman spectroscopy or two-photon excited photothermal microscopy) at single-particle level are required to find the effect of NP's size, surface modification and environment on the observed enhancement.[131].

Independently of AFM measurements, the combined optical absorption and luminescence microscopy of individual NPs is a convenient new method to study luminescence of gold particles with various shapes and to compare to theory. Gold nanorods, platelets, stars, cubes, pyramids, and various organic or hybrid NPs are obvious candidates for future investigations. Absorption and luminescence properties of these NPs can be used for applications where the combination of photostability and brightness of the labels are

required.

Acknowledgements

We thank Dr. Peter Zijlstra for helpful discussions of the origins of gold NPs luminescence, as well as the BioAFM Lab at Leiden Institute of Physics, in particular Dr. Federica Galli and Prof. Tjerk Oosterkamp for the support with AFM equipment. We acknowledge the financial support by ERC (Advanced Grant SiMoSoMa).

CHAPTER 5

Luminescence quantum yield of single gold nanorods

We study the luminescence quantum yield (QY) of single gold nanorods with different aspect ratios and volumes. Compared to gold nanospheres, we observe an increase of QY by about an order of magnitude for particles with a plasmon resonance >650 nm. The observed trend in QY is further confirmed by controlled reshaping of a single gold nanorod to a spherelike shape. Moreover, we identify two spectral components, one around 500 nm originating from a combination of interband transitions and the transverse plasmon and one coinciding with the longitudinal plasmon band. These components are analyzed by correlating scattering and luminescence spectra of single nanorods and performing polarization sensitive measurements. Our study contributes to the understanding of luminescence from gold nanorods. The enhanced QY we report can benefit applications in biological and soft matter studies.

The contents of this chapter are based on:
M. Yorulmaz, S. Khatua, P. Zijlstra, A. Gaiduk, and M. Orrit, "Luminescence quantum yield of single gold nanorods", Nano Lett. **12**, 4385-4391 (2012)

5.1 Introduction

Optical probes that provide good contrast and are small enough not to perturb the system under investigation are essential to obtain structural and dynamical information on the nanoscale. For this purpose, single fluorescent molecules are widely used as probes of, for instance, soft matter systems[24,47,48,203] and biological mechanisms[45,46] since they are small and have a high fluorescence quantum yield. However, single molecules suffer from blinking[51] and bleaching,[53] which limits their observation time.

Gold nanoparticles do not blink nor bleach and their nontoxicity and biocompatibility make them attractive for biological applications.[11,28] There has been a considerable effort to investigate their size- and shape-dependent optical properties, both experimentally[32,156] and theoretically.[72,73] Their scattering and absorption properties have been widely investigated and characterized, which has led to many new applications.[71]

In recent studies, the photoluminescence from single gold nanoparticles has proven to be a complementary property to absorption and scattering for imaging and sensing purposes.[192,204–207] Although the luminescence quantum yield (QY) of gold nanoparticles is several orders of magnitude lower than the QY of fluorescent labels such as organic dyes or semiconductor nanoparticles, their large absorption cross section compensates for their low QY, making them high-contrast imaging agents.

The first observation of photoluminescence of gold dates back to 1969, when Mooradian studied bulk gold[208] and observed a broad luminescence spectrum with a QY of about 10^{-10}. Photoluminescence from bulk gold originates from radiative transitions of conduction electrons toward empty electron states, which can be either holes in the d-band (electron-hole interband recombination),[208–211] or empty electron states or holes within the sp-conduction band (intraband transitions).[182]

Later, the effect of surface roughness on the photoluminescence of gold was studied by Boyd et al. who showed that the QY could be enhanced by several orders of magnitude compared to a smooth film.[210] The enhancement was attributed to the concentration of fields at tips of surface protrusions (lightning-rod effect) and to the presence of localized surface plasmons.[210,212] Since this first observation of plasmon-enhanced emission, the effect of localized surface plasmons has been investigated in solutions of nanoparticles

with different sizes and shapes.

Early efforts to understand the emission from gold nanoparticles have relied on ensemble measurements. A QY of $\sim 10^{-5}$ to 10^{-4} was reported for ensembles of 5 nm diameter gold nanospheres by Wilcoxon et al.[186] Mohammed et al.[213] have measured the luminescence from ensembles of gold nanorods with aspect ratios ranging from 2.4 to 5.4 and reported QYs of 10^{-4}-10^{-3}. They have explained the observed luminescence by the radiative recombination of electron-hole pairs that is enhanced by local fields associated with the particle plasmon resonance. In a recent ensemble study by Dulkeith et al., the QY of gold nanospheres with diameters ranging from 2 to 60 nm was reported to be $\sim 10^{-6}$ and independent of size.[180] These authors argued that the moderate field enhancement of about 10 was too weak to explain this enhancement by 4 orders of magnitude compared with bulk gold. Instead of the radiative recombination of e-h pairs, the authors proposed a process in which d-band holes recombine non-radiatively with sp electrons. In the process, each excited d-band hole polarizes the particle and thus triggers a collective electron oscillation, that is, a surface plasmon. These plasmons decay either radiatively by emitting photons or nonradiatively via transformation into excited e-h pairs.

The reported QYs of gold nanoparticles in ensemble measurements differ by 2-3 orders of magnitude. The observed variations could be due to the presence of inhomogeneities within the sample. For instance, the measured signal can be easily overestimated due to a low number of aggregates of nanoparticles. Other measurements may have been affected by reabsorption of luminescence, which reduces the apparent signal. This complicates the interpretation of ensemble studies and manifests the need for single-particle measurements.

Gaiduk et al.[156] reported the luminescence QY of single gold nanospheres to be $\sim 3 \times 10^{-7}$ on average and independent of size for diameters ranging from 5 to 80 nm, which is in agreement with the measurements of Dulkeith et al.[180] Recently, one-photon plasmon luminescence from individual nanorods has been studied by Tcherniak et al.[206] They showed that plasmons play a central part in the observed luminescence from nanorods, because the luminescence spectrum closely reproduces the sharp plasmonic band of the scattering spectrum. The same group reported the QY of a single gold nanorod of 24 nm $\times$ 76 nm to be 8×10^{-6} when excited at 514 nm. This measured QY is

significantly higher than the QY reported by Gaiduk et al.[156] for single gold nanospheres. However, no explanation was proposed for the larger QY of nanorods and its shape dependence.

The reported luminescence QY for nanoparticles with different sizes and shapes range from 10^{-7} to 10^{-4} in the above-mentioned studies.[156,180,186,206,213] Although it was shown that the QY is roughly independent of size for nanospheres, further experiments are required to establish the effects of the particle shape. These studies could shed light on the mechanism of the luminescence, which will benefit potential applications.

In this chapter, we present a detailed study of the luminescence QY of single gold nanoparticles of different shapes and sizes. We systematically study nanorods with aspect ratios ranging from 1 (sphere) to 3.5. We show about an order of magnitude increase in QY for nanorods with longitudinal plasmon wavelengths longer than 650 nm compared to spheres. The observed trend is confirmed when a single gold nanorod is slowly reshaped to a spherelike shape. We find a strong correlation between the scattering and luminescence spectra of the same particle, confirming the plasmonic influence on the observed luminescence. Finally, we investigate the luminescence spectrum of a nanorod by performing polarization-sensitive measurements. We show that the emission is dominated by a polarized contribution that coincides with the longitudinal plasmon. In addition, we consistently observe a weak short-wavelength component that peaks around 500 nm and is not (or only weakly) polarized. We attribute this component to a combination of interband transitions and the transverse surface plasmon.

5.2 Experimental

5.2.1 Sample preparation

We prepared gold nanorods with different sizes by varying the silver ion and seed concentration in a seed-mediated growth method.[214] Electron microscopy images and the dimensions of the nanorods used in this study are shown in Fig. 5.1. The extinction spectra of the nanorod suspensions are shown in Appendix D (Fig. D.1), where longitudinal SPRs at around 630, 650 and 730 nm are observed for nanorods with ensemble-averaged aspect ratios of 2.4, 2.6 and 3.4, respectively. In addition, we used a commercial col-

loidal suspension of 18.5 nm diameter[156] gold nanospheres (British Biocell International).

For the optical experiments we spin-coated gold nanoparticles on a clean glass substrate and used glycerol as immersion liquid. We obtained samples with well-separated nanoparticles so that single particles could be optically resolved.

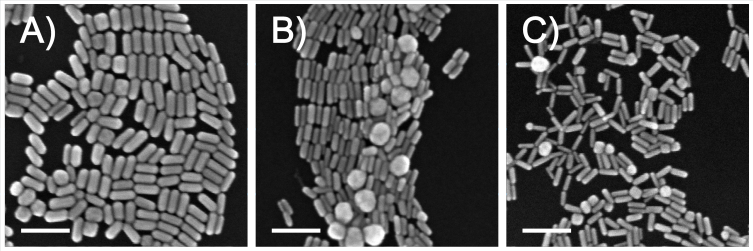

sample	length (nm)	width (nm)	asp. ratio	V (10^3 nm^3)
A	58±5	25±4	2.4±0.4	24±7
B	34±5	13±3	2.6±0.5	4±2
C	38±3	11±1	3.4±0.3	4±1

Figure 5.1: SEM images of the three samples used in this study. The table shows the dimensions of nanorods for each sample with standard deviations of the mean. Scale bars are 100 nm.

5.2.2 Optical microscopy

We performed single particle measurements on our home-built combined photothermal, scattering, and luminescence microscope, assembled on an inverted optical microscope (Olympus IX-71). Our photothermal microscope is described in detail elsewhere (see Chapter 2).[90] The schematic of the setup and the experimental details for combined photothermal (absorption) and fluorescence microscopy are given in Section 3.2.1. Details of combined fluorescence and scattering microscopy are discussed in Appendix D (Fig. D.2). Briefly, the continuous wave (cw) excitation light is time-modulated and overlapped with a cw probe beam that is off-resonance with the plasmon. Both excitation and probe lasers are focused through a microscope objective onto the sample. The energy absorbed by the particle is mainly released as heat giving rise to a temperature gradient ΔT_{surf} around the nanoparticle (Appendix D, Fig. D.3). The probe laser is scattered by the resulting refractive

index profile. This scattered field interferes with the reflected field creating small changes in the detected probe intensity. A lock-in amplifier demodulates the signal and provides the photothermal signal.

Photothermal microscopy provides contrast only for absorbing objects and suppresses scattering background from impurities or interfaces. The photothermal signal is proportional to the absorption cross section and in turn to the volume of the nanoparticle for a given excitation wavelength. To obtain the absolute absorption cross section of single nanorods we used gold nanospheres with a diameter of 18.5 nm as a calibration sample.[156] When the nanorods and nanospheres are imaged under the same illumination conditions the absorption cross section of a nanorod follows from:

$$\sigma_{\mathrm{NR}} = \sigma_{18.5} \times \frac{S_{\mathrm{NR}}}{S_{18.5}} \tag{5.1}$$

where σ_{NR} is the absorption cross section of the nanorod, $\sigma_{18.5}$ (calculated using full Mie theory[72] to be 203 nm^2 at 476 nm) is the absorption cross section of a single 18.5 nm diameter gold nanosphere, S_{NR} is the measured photothermal signal of a nanorod, and $S_{18.5}$ is the measured average photothermal signal of 18.5 nm spheres.

We chose 476 nm laser light (circularly polarized) as the excitation wavelength for both photothermal and luminescence imaging and an off-resonant 864 nm laser light as probe laser for photothermal microscopy. We sequentially recorded luminescence and photothermal images of the same particles at the same excitation intensity. With Eq. 5.1, the photothermal signal directly gives the measured absorption cross section at 476 nm, which was used to calculate the luminescence QY. Note that this method takes into account all factors that govern the absorption cross section of a particle such as defects, shape irregularities, and variations in local environment. These factors are difficult to take into account in calculations.

5.3 Results and discussion

We show typical photothermal and luminescence raster scan images of isolated nanorods with an ensemble-averaged aspect ratio of 2.4 in Fig. 5.2 A,B. Both images were recorded on the same area. The color scales of photothermal and luminescence image show the calculated absorption cross section

and luminescence count-rate. To confirm that each bright spot corresponds to a single gold nanorod, we recorded luminescence spectra of each particle, shown in Fig. 5.2 C. A single Lorentzian line-shape confirms that each spot corresponds to an individual nanorod. We observe a large spread in plasmon energy which is consistent with the presence of a broad distribution of aspect ratios as observed in electron microscope images (Fig. 5.1). Aggregates are easily identified in the spectra by a broadened or split peak[31] (Appendix D, Fig. D.4). Signals of such particles were discarded from the data analysis. We also checked that the plasmon resonance and the spectral line shape of each individual particle did not change after all measurements were finished. A typical example of these control experiments is shown in Appendix D (Fig. D.5). In order to check if the observed luminescence is a one-photon process, we measured the power dependence of the luminescence intensity. Indeed, the luminescence intensity was linearly dependent on the excitation laser power as shown in Appendix D (Fig. D.6). The excitation power dependence of the photothermal signal also exhibits a linear dependence, as expected[90] (Appendix D, Fig. D.6).

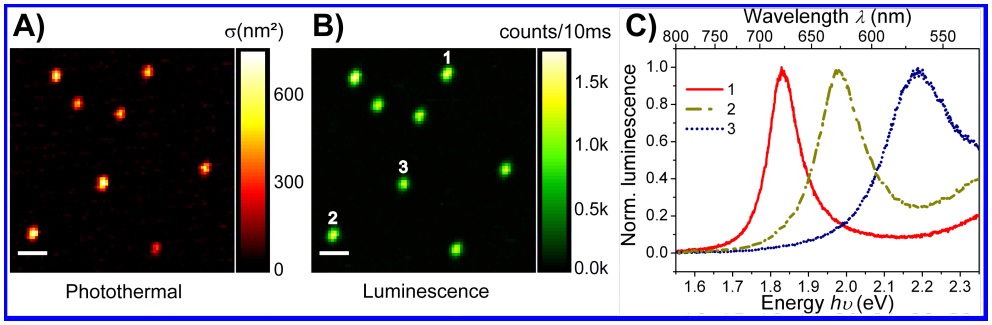

Figure 5.2: (A) Photothermal and (B) one-photon luminescence images of individual gold nanorods on a glass coverslip, immersed in glycerol. The scale-bars are 1 μm. (C) Normalized luminescence spectra of the numbered particles in panel B. Experimental: the excitation intensity is $I_{\text{exc}} = 32\ \text{kW/cm}^2$ (circularly polarized) for photothermal and luminescence images and luminescence spectra; the probe intensity is $I_{\text{probe}} = 1.4\ \text{MW/cm}^2$ to record photothermal images; acquisition and lock-in integration times for luminescence and photothermal images are $t_{\text{acq}} = 10$ ms and $t_{\text{int}} = 3$ ms, respectively. Each luminescence spectrum was recorded in 10 s.

The QY of individual nanorods was calculated from the signal strength in the photothermal and photoluminescence images. The photothermal sig-

nal was first converted into an absorption cross section, according to Eq. 5.1. Then, the luminescence count-rate of each single nanorod was used to calculate the QY[56,156] as follows:

$$\eta_{\mathrm{lum}} = \frac{N_{\mathrm{em}}}{N_{\mathrm{abs}}};\ N_{\mathrm{em}} = \frac{N_{\mathrm{signal}}}{\Pi_{\mathrm{setup}}};\ N_{\mathrm{abs}} = \frac{\sigma_{\mathrm{NR}} I_{\mathrm{exc}}}{h\nu_{\mathrm{exc}}} \tag{5.2}$$

where η_{lum} is luminescence QY, N_{em} is the number of emitted photons, N_{abs} is the number of absorbed photons, N_{signal} is the measured luminescence count-rate, Π_{setup} is the wavelength-dependent detection efficiency of the setup (Appendix D, Fig. D.7), σ_{NR} is the absorption cross section of the nanorod (obtained from the photothermal signal), I_{exc} is the excitation laser intensity and $h\nu_{\mathrm{exc}}$ is the photon energy of the excitation light. We estimate the error, $\delta\eta_{\mathrm{lum}}/\eta_{\mathrm{lum}}$, in the measured QYs to be 30%, taking into account the individual errors in the variables used for the QY calculation (Eq. 5.2).

In Fig. 5.3 we show the measured QY for individual nanorods with aspect ratios ranging from 1 to ∼3.5, or plasmon wavelengths ranging from 530 to 780 nm. The experiments were performed on 150 nanorods from the three samples shown in Fig. 5.1. We observe a significant increase in QY for particles with a plasmon between 530 and 650 nm. For nanorods with a plasmon resonance beyond 650 nm we observe no significant change in QY anymore.

The QY increase for longer nanorods with a plasmon moving from 530 to 650 nm may be correlated with the decreased damping of the plasmon by creation of interband excitations. The higher aspect ratio nanorods emit further away from the interband transitions. As the surface plasmon moves away from the interband transitions, less channels are available for dissipation, which raises the efficiency of radiative emission.[89] It is thus the proximity of the interband transitions to the plasmon resonance frequency that determines the QY. For nanorods with a plasmon energy lower than 1.8 eV,[215] creation of interband excitations is impossible and radiative emission only competes with the creation of intraband excitations.

It is important to note that the observed increase in QY is not caused by (photo)chemistry-mediated enhancements as we observed before on strongly excited gold nanospheres[155] (see Section 4.3.4). We reported a nonreversible enhancement in luminescence of gold nanospheres when the surface temperature of the nanoparticles was raised by 60 K.[155] The increase in luminescence was explained by modification of the surface of the nanoparticle, caused

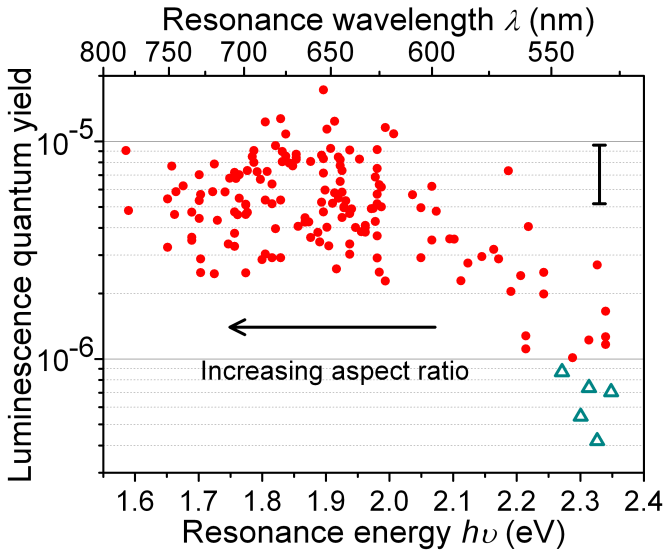

Figure 5.3: Luminescence QY of individual nanorods as a function of their plasmon resonance energy (red-filled circles). Data shown with open-dark-cyan triangles are from 18.5 nm diameter spheres and shown for comparison. Each individual dot here represents one particle. The arrow in the graph indicates the direction of increase of the nanorod aspect ratio. The error bar represents the estimated error in the QY measurement.

by thermal processes, photochemical processes, or a combination of both. To eliminate these effects we kept the surface temperature rise below 10 K by employing a low excitation intensity (for more details see Appendix D, Fig. D.3).

The QY of nanospheres was shown to be roughly independent of their size.[156] In order to establish the effect of the volume of a nanorod on its QY, we selected particles with similar plasmon energies but with different volumes (i.e., photothermal signal) from the data points in Fig. 5.3. We observe no significant dependence of the QY on volume (Appendix D, Fig. D.8). However, there is a slight decrease in QY for nanorods with larger volumes, as we also observed before for spheres[156] (see Chapter 4, Section 4.3.3). We hypothesize that the quantum yield may be lowered by reabsorption of radiation within the larger particles. The origin of this slight decrease is unknown and requires further investigation.

Figure 5.3 indicates a broad distribution of QYs, even for particles with

a similar plasmon energy. For example, particles with a plasmon between 620 and 630 nm exhibit QY values that range from 2.3×10^{-6} to 1.2×10^{-5}. We attribute this spread in QY to local irregularities in crystal structure, to faceting of particle surfaces, and/or to the possible presence of defects on the surface of the nanorods. In addition, small variations in the particle environment due to a molecular-scale contamination can cause these distributions. We cannot rule out the effect of small variations in the detection efficiency for different polarizations, which, among other mentioned reasons, could cause variations in the observed QY due to the random orientation of the particles on the sample surface.

Reshaping, the laser-induced shape transformation of a nanorod toward a spherical shape, can occur at temperatures well below the melting point of bulk gold (1064°C).[68,216,217] This allows us to compare the QY on one-and-the-same particle for different plasmon energies. For that purpose, we controllably reshaped a single gold nanorod in several steps, and measured its QY after each reshaping step. The reshaping was done by heating the particle with a circularly polarized 514 nm cw laser with powers ranging from 2 to 5 mW at the sample. These powers raise the particle's temperature by up to $\Delta T_{\text{surf}} \sim 160\ K$, resulting in a slow reshaping of the nanorod and a gradual blue shift of its plasmon resonance. We increased the excitation laser power and irradiation time as the nanorod's shape became more and more spherical in order to compensate for the increased thermal stability of lower aspect ratio particles.[69] The photothermal signal did not change significantly during the transformation of the nanorod to a sphere-like shape. This observation confirms that the volume of the particles is maintained.

The result of the thermal reshaping of the nanorod with an initial plasmon at 720 nm is shown in Fig. 5.4 where the QY of the nanorod is plotted as a function of its plasmon resonance after each reshaping step. Figure 5.4 clearly shows no significant change of QY when the plasmon resonance shifts from 720 to 640 nm. Further melting the particle shifted its plasmon to 540 nm and its QY reduced by a factor of 6. These results confirm the overall trend of QY that we observed in Fig. 5.3

We note that, even though the surface temperature increase was up to $\sim$160 K in this experiment, we did not observe any photoinduced luminescence as we reported before for citrate-capped gold spheres (see Chapter 4, Section 4.3.4).[155] In this study, we employed CTAB-coated gold nanorods,

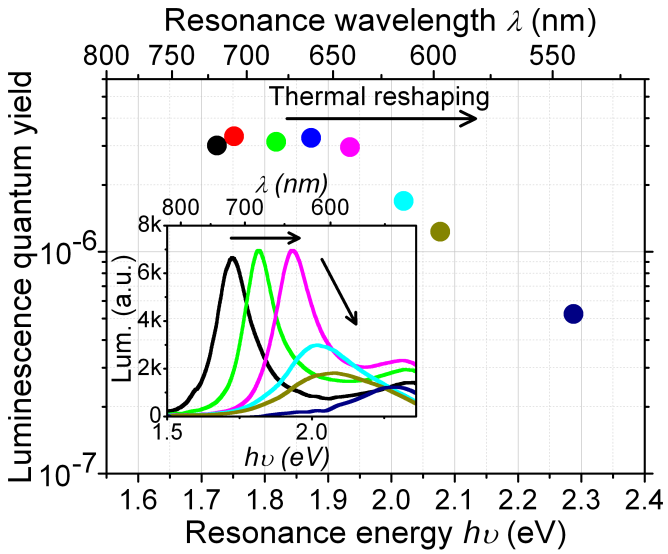

Figure 5.4: Controlled photothermal reshaping of a single gold nanorod. Each dot represents the QY of the same nanorod obtained after each thermal reshaping step as a function of its resonance energy. The inset shows the luminescence spectra of the nanorod after each reshaping (melting) step. Arrows in the graph indicate the direction of spectral and intensity change upon melting of the nanorod.

which were UV/ozone cleaned before the experiment to remove all organic molecules from the surface. The absence of the organic capping layer eliminates the photoinduced luminescence and allowed us to employ higher excitation powers.

In order to investigate the origin of the observed luminescence, we correlated the luminescence and the scattering spectra of the same particle. The results of these experiments are shown in Fig. 5.5. Figure 5.5 A,B shows luminescence and scattering images recorded on the same sample area. The luminescence spectra (green dots) correlate very well with the scattering spectra (blue lines) in Fig. 5.5 C, confirming the plasmonic origin of luminescence as previously reported.[180,182,217] We further confirmed the correlation between luminescence and scattering spectra by changing the medium around the same gold nanorod from air to glycerol, which caused a shift of both the scattering and the luminescence bands from 625 to 680 nm (Appendix D, Fig. D.9).

We note that there is a slight difference between photoluminescence and

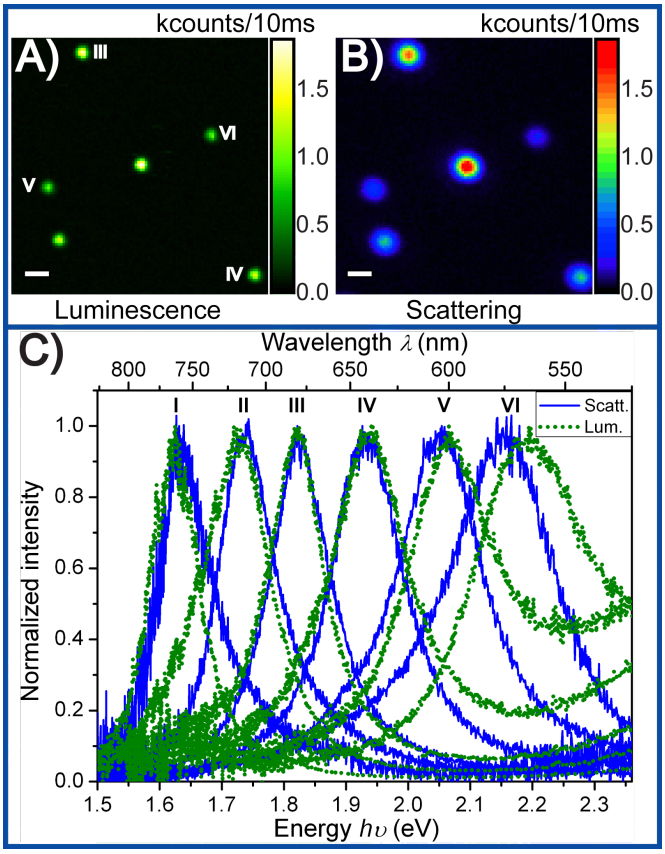

Figure 5.5: Correlation of scattering and luminescence spectra of individual gold nanorods with different aspect ratios. (A) Photoluminescence and (B) dark-field scattering image of gold nanorods with ensemble average aspect ratio of ∼2.4 taken on the same area of the sample. Scale bars correspond to 1 μm. (C) Correlation of normalized luminescence (green dots) and normalized scattering (blue line) spectra for nanorods with different aspect ratios. Photoluminescence signals were obtained with circularly polarized excitation at 476 nm and scattering signals were obtained by excitation with unpolarized white light. Particles I and II are measured from a different sample with an ensemble average aspect ratio of ∼3.4 to cover a larger wavelength range.

scattering spectra both in terms of peak position as well as the line-shape. This slight difference is especially apparent for nanorods with a lower aspect ratio (shorter resonance wavelength). Luminescence spectra appear broader as well as slightly blue shifted. Part of the shift may be due to a broad back-

ground ("green" emission), starting at about 690 nm (energy 1.8 eV) and increasing for shorter waves, which overlaps with the longitudinal plasmon of the shorter rods (see Fig. 5.5).

We further investigated the green component of the emission. By correlating its intensity with the photothermal signal for many individual particles, we found that this component is proportional to the volume of the nanorod (Appendix D, Fig. D.10). We then performed the polarization measurements presented in Fig. 5.6. To reduce depolarization effects by the microscope objective we decreased the excitation and collection NA to approximately 0.9. The right inset of Fig. 5.6 shows that the longitudinal plasmon component is strongly polarized, as expected for a dipolar emission pattern. In contrast, we did not observe any clear polarization of the green emission. This observation suggests that this component cannot be exclusively due to the transverse plasmon, which should be polarized along the short axis of the particle. The polarization anisotropy is a measure for the degree of polarization of the emission and is defined as

$$P = \frac{I_{\parallel} - I_{\perp}}{I_{\parallel} + I_{\perp}} \tag{5.3}$$

where $I_{\parallel}$ and $I_{\perp}$ are the emission intensities with an analyzer along the long and short axis of the nanorod, respectively. P is 0.9 for the longitudinal plasmon. We find $P = 0.1$ for the green component indicating a nearly unpolarized emission.

The green component we observe is peaked close to 500 nm, similarly to the luminescence of a smooth gold film measured by Beversluis et al.,[182] which they attributed to interband transitions (between d-band and sp-conduction band near the X and L points in the Brillouin zone). Any unpolarized interband emission should be enhanced by the transverse plasmon, as it happens for spheres. Some residual enhancement by the longitudinal plasmon may explain the absence of a clear polarization of the green component. Further studies are required to clarify this point.

Finally, we would like to discuss what our observations may tell us about the mechanism of the photoluminescence of gold nanoparticles. Two models have been proposed in the literature.

(i) The first model, based on energy transfer, postulates that the energy from an electron-hole pair is transferred to a plasmon excitation, which then

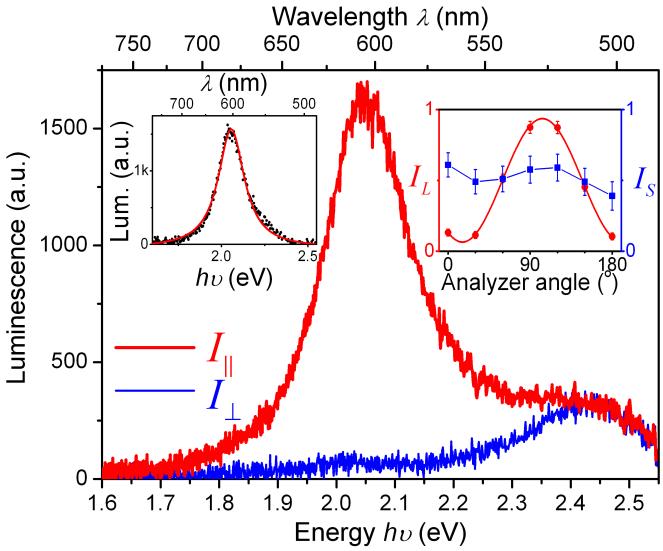

Figure 5.6: Luminescence spectra of a gold nanorod excited by a circulary polarized 476 nm laser beam and recorded with a detection polarizer parallel ($I_{\parallel}$, red) and perpendicular ($I_{\perp}$, blue) to the long axis of the nanorod. Left inset shows the longitudinal component of the luminescence spectrum (black dots) that is obtained after subtracting the luminescence spectrum perpendicular to the long-axis of the nanorod and the Lorentzian-line fit (red). Right inset shows the detection polarization dependence of the long wavelength peak (I_L, red dots) and the short wavelength peak (I_S, blue dots).

emits a photon.[23,180,217] The molecular analog is a FRET process, in which a virtual photon from the donor is absorbed by the acceptor, relaxes, and is re-emitted as acceptor fluorescence by the acceptor dipole moment.

(ii) The second interpretation involves the internal field enhancement, which in nanorods ranges from ten to a hundred.[218] The optical field created by the recombination is shared by the plasmon and enhanced by its antenna effect, enhancing the emission rate[182,213,219] (for gold particles excited at wavelengths shorter than 500 nm, no excitation enhancement is expected, and only luminescence enhancement can occur). The molecular analog of this mechanism is the emission of an exciton, a strongly coupled pair of molecules. The emission of the coherent exciton state proceeds via the collective dipole moment of the pair, not that of the acceptor alone.

In both cases, the luminescence is mainly determined by the plasmon's

dipole moment, either because the plasmon itself emits (model i) or because the plasmon's dipole moment is much larger than that of the original source, and because the enhancement factor resonates at the plasmon frequency (model ii). Therefore, the mere observation of the plasmon band in the luminescence spectra does not allow us to discriminate between the two models.

5.4 Conclusions

We have investigated the one-photon photoluminescence properties of single gold nanoparticles by performing photothermal, fluorescence and dark-field scattering microscopy on the same individual particles. Our approach provides a direct measurement of the absorption cross section, emission intensities, and of the QY. We find that the QY of single gold nanorods with plasmon wavelengths longer than 650 nm is about an order of magnitude larger than that of single gold nanospheres. The observed QY is largely independent of the volume of nanorods, which is in agreement with our previous measurements on spheres. Over a broad spectral range, we find that the photoluminescence spectra closely resemble the scattering spectra, confirming the plasmonic nature of the emission. In the luminescence spectra, we find a weak, unpolarized component that we attribute to a combination of interband emission and transverse plasmon. Our results provide a better description and understanding of the photoluminescence of single gold nanoparticles and pave the way for their potential use in biological and soft matter studies. In our QY measurement, we excited the nanorods at 476 nm to reduce the effect of aspect ratio on the absorption cross sections. However, in a recent study the QY of a nanorod was reported to be even higher when excited on the blue wing of the longitudinal plasmon.[206] For future studies, it is therefore interesting to investigate the excitation wavelength dependence of the QY to obtain a complete picture of the luminescence mechanism. Here, we only studied one-photon luminescence properties of single gold nanorods. It would be interesting to investigate their QY and photoluminescence spectra upon two-photon excitation.

Acknowledgements

We acknowledge financial support by the ERC (Advanced Grant SiMoSoMa). This work is a part of the research program of the "Stichting voor Fundamenteel Onderzoek der Materie", which is financially supported by The Netherlands Organization for Scientific Research (NWO). Dr. Peter Zijlstra acknowledges financial support by NWO (Veni fellowship).

CHAPTER 6

Influence of an approaching dielectric interface on the plasmon resonance of a gold nanorod

We study the effect of the distance between a gold nanorod and a glass surface on the plasmon resonance of a gold nanorod. To achieve this aim, we immobilize gold nanorods on one substrate, which is approached by the other one. These two substrates are bent rectangular cover-slides whose cylindrical axes are perpendicular to each other. We select a nanorod on the area where the two substrates can come into contact. In this geometry, a ring-shaped interference pattern (i.e. Newton's rings) appears at the contact area. The center of this pattern is determined prior to achieving contact between the substrates. Combining single-particle fluorescence spectroscopy and white-light interferometry, we follow the one-photon-excited luminescence spectrum of an individual nanorod as a function of the distance between the two substrates. We observe a significant red-shift of the surface plasmon for separation distances below 400 nm. This effect is reversible. Although the results are preliminary, this sensitivity of the plasmon resonance of a nanoparticle to its local dielectric environment may be useful in the study of interfaces between two solids and to map the contact areas between them.

6.1 Introduction

Studying the interactions between two approaching surfaces is essential for many scientific and technological applications. Materials with specific properties can be designed and developed to make miniaturized devices with optimal mechanical performance.[106,220] For instance, wear in sliding contacts can be reduced using lubricants.[221,222] Intermolecular and surface forces between moving or stationary bodies give rise to a resisting force against motion. In order to control friction between surfaces, it is necessary to investigate the structure of the contact area.[105–107] All surfaces in nature have roughness, which extends over many different length scales, from atomic ($\sim$ nm) to macroscopic dimensions ($\sim$ mm). These complex heterogeneities of the contacting interfaces make the interactions between the two bodies difficult to study.

Early experiments to understand these complex interactions have been started as early as 1699 by Amontons. He used different materials (i.e. iron, lead, wood) in different combinations and measured the force necessary to bring a plate to slide on another plate. He found the friction force to be directly proportional to the applied load and independent of the macroscopic contact area.[223] By 1781, the distinction between static and kinetic friction was made by Coulomb. He studied the friction between sliding surfaces of different materials and considered the effect of sliding velocities on the friction. Coulomb is often credited with the third law of friction, which states that the kinetic friction force is nearly independent of the sliding velocity. Later, Hertz's theory suggested that the contact area would increase nonlinearly with the applied load under elastic deformation.[224] After the pioneering work of Hertz,[224] the experimental and theoretical effort was increased to study the real contact area between two solids that are brought together. For example, surfaces of elastic materials were reported to present many irregularities.[109,225] Bowden and Tabor suggested the presence of a number of small spherical contact points (asperities) which are uniformly distributed within the boundary of macroscopic contact.[109] The sum of the contact areas at asperities was then suggested to be smaller than the apparent contact area. This assumption was refined by Archard who showed that small asperities could also be present on each asperity.[225] According to this latter model, the increasing number of contacting asperities at the interface results in a near

proportionality of the contact area to the load. A more detailed model than the previous one was presented by Greenwood and Williamson[110], who took into account a Gaussian distribution of asperity heights and possible deformation of high asperities.[224] They also predicted the real contact area to be nearly proportional to the applied load. Because surfaces exhibit roughness on different length scales, the real area of contact is different from the apparent contact area.[107,110,112,226–228]

In recent studies, the tribological interactions that take place at solid-solid or solid-liquid-solid interfaces have been studied by sensitive scanning probe and optical microscopy techniques.[229–236] In scanning probe techniques, topography images are usually obtained by recording the distance-dependent changes of probe-sample interactions. The standard approach to study the real contact area between solids at molecular scales has been conventional atomic force microscopy (AFM)[237]. This technique can provide topography images of a solid surface with a very high resolution, down to atomic scale.[238] However, the contact in AFM studies takes place between the AFM tip and the very local region under the tip.[239] The deformation under and around the tip may be very different from the deformation of the bodies in the extended contact areas. Moreover, the information obtained from AFM topography images depends very much on the tip shape and on the path the tip follows.[113,239–241]

Optical microscopy measurements are usually noninvasive and can provide a larger field of view than scanning probe microscopy.[112,231,242] The surface force apparatus of Israelachvili[231] is used to measure the forces between two solid surfaces usually immersed in a liquid (e.g. Van der Waals and electrostatic forces). This instrument consists of two curved surfaces and sensitive force-measuring leaf springs. In this method, the forces between curved surfaces are measured while one of the two surfaces is approached or retracted. The forces measured can be as weak as 10^{-8} N. The distances between the two surfaces are measured using optical interferometry, down to 0.3 nm.[243] For a reliable measurement, atomically smooth surfaces (i.e. mica) are needed. Uses of the surface force apparatus are therefore restricted to special measurement conditions and samples.

In a recent study of Krick. et. al[112], interferometric optical measurements and mechanical measurements were combined by an optical in-situ tribometer. They used changes in the intensity of 0^{th} order Newton's rings to probe

the complex area of contact between a rubber sphere and a polished glass flat. The intensity reflected by the interface between two solids (at least one of them has to be transparent) monotonically decreases for air gaps less than a quarter of a wavelength. Monitoring this reflection in a wide-field image, Persson and coworkers[112] could map the separation between two surfaces. However, in wide-field imaging, removing reflection contributions from other, off-focus interfaces is difficult. Therefore, they had to subtract a background image (obtained when sphere and glass were not in contact) from the contact image (when sphere and glass were in contact). In this way, they obtained topography images for different applied loads (mN), but, because of the noise in the subtraction, they could not measure very small gaps accurately. They applied this method mostly to determine the roughness of the rubber sphere, which was on the order of a few μm. For quantitative determinations of very small gaps, it would be advantageous to use confocal scanning instead of wide-field imaging.

Another example of optical imaging of topography is the well-known technique of frustrated total internal reflection microscopy.[242,244] In this technique, evanescent waves are created at a plane interface by total internal reflection of light of wavelength λ, and a second parallel plane interface is approached towards the first one. For distances below the typical decay length of the evanescent wave between the two interfaces, evanescent waves interact with the second interface and can be partly transmitted as propagating radiation. The relative intensity of the transmitted light depends on the distance between the two substrates. The transmitted intensity exponentially decreases for increasing gap widths.[244] Therefore, transmission measurements will provide accurate measurements of large gaps (provided the transmitted intensity is still measurable). Conversely, reflection vanishes for vanishing gaps and will be very sensitive to small gaps (see previous discussion). Shallow topographic features with sizes smaller than $\lambda/2\pi$ or smaller were detected using this method.[242] Small gaps can also be measured in a similar way by observing the reflection at normal incidence.

Sensitive plasmonic sensors[14,119,245] can be applied for measuring distances between two substrates, and might be useful to improve the lateral resolution of measurements of the contact area. These sensors exhibit a very high sensitivity to refractive index changes,[78] because their plasmon resonance is highly sensitive to the dielectric environment.[25,31,246] The sensitivity

of gold nanorods to local environmental changes has been exploited in numerous applications.[14,25,119,247,248] In these studies, nanorods served as transducers of molecular binding events in biological or chemical experiments. Their signals are also sensitive to the changes in their orientation.[149] Moreover, gold nanorods are easy to synthesize and they can cover larger areas than those probed by scanning probe measurements. For this purpose, it is important to study the sensitivity of single gold nanorods to nearby surfaces.

In our study, we investigate the response of the gold nanorod with respect to an approaching glass substrate. We use two curved glass substrates whose longitudinal axes are oriented perpendicular to each other (so called "crossed-cylinder" geometry[231]). We immobilize gold nanorods on one glass substrate and deposit a thin layer of PMMA on the other substrate. We perform luminescence spectroscopy on a single gold nanorod to study the distance dependence of its plasmon resonance. Changes in the refractive index of the medium affect the optical properties of the gold nanorods,[249] i.e., the plasmon resonance wavelength red-shifts for decreasing gaps between the glass substrates.[14,250] The observed changes are related to the rapid decay of the electromagnetic near fields away from the surface of the gold nanorod[14,251] and to the interactions of plasmon with the mirror image of the nanorod in the nearby dielectric surface.[250] We show that the gold nanorod exhibits distinct changes in its plasmon resonances. Gold nanorods can find applications for sensing in biology or tribology studies as they exhibit distinct changes in their plasmon resonances by the variations in the local nm-scale environment.

6.2 Methods and materials

6.2.1 Fluorescence spectroscopy and white-light interferences

We performed fluorescence spectroscopy measurements on our home-built variable-distance cell, assembled on an inverted microscope. The schematic of the setup is shown in Fig.6.1. Circularly polarized light (476 nm) is used for fluorescence excitation. The beam is expanded to $\sim$20 mm and reflected off from a 20R/80T beam-splitter towards an oil-immersion microscope objective (Olympus, 60$\times$, 1.45 NA). The excitation light is focused by the objective to a diffraction-limited spot (about 300 nm in diameter) for excitation

of individual gold nanorods. The luminescence from nanorods and backscattered excitation light are collected by the same microscope objective and they are transmitted through the beam splitter. The luminescence is filtered out from the excitation light by long-pass filters (LP02-514RS-25, Semrock and NF476, AHF) and is spatially filtered by a 75 μm pinhole. Luminescence images and spectra of the same individual nanorods are respectively detected by an avalanche photodiode and by a spectrometer with the help of a mirror installed on a flip mount. During luminescence measurements, nanorods are immobilized on one glass substrate, which can be approached by another one (see Section 6.2.2).

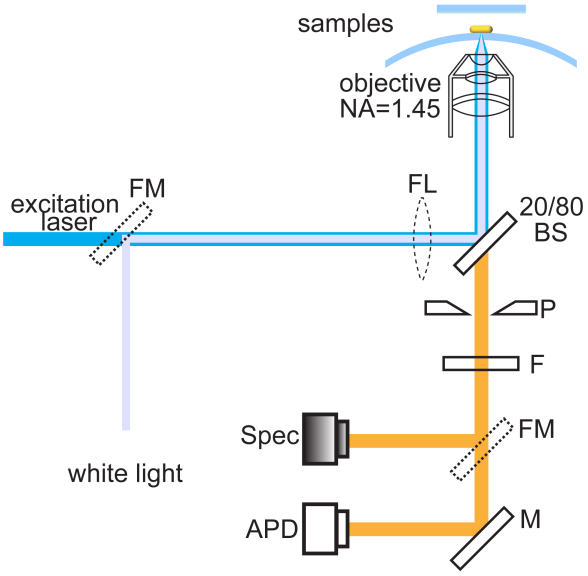

Figure 6.1: Schematic of the experimental setup. FM-flip-mirror; FL-flip-lens; NA-numerical aperture; BS-beam-splitter; P-pinhole; F-filter; M-mirror; APD-Avalanche photodetector; Spec-Spectrometer.

For recording white-light interference, a 100 W halogen lamp is used as the light source. The white light is focused at the back focal plane of the microscope objective (Olympus 60×,1.45 NA or Olympus 10×, 0.4 NA). This way, a collimated beam in the air gap within the two substrates is obtained. An interference pattern (fringes) is created by the interference of reflected waves from the air-glass interfaces. The interference spectra are recorded using a spectrometer and used for measuring air-gap widths between the sub-

strates (see Section 6.3.1, Figure 6.5). White-light interference images are also recorded. The obtained image represents the well-known Newton's rings, which are useful to find the contact area (see Section 6.3.1, Figure 6.4).

6.2.2 Variable-distance cell

We used a variable-distance cell to change the distance between the two substrates so that we could study the influence of nanorod-substrate distance on the plasmon resonance of a gold nanorod. The variable-distance cell is formed of two curved sample holders, two three-axis (xyz) piezo-stages and several aluminum adapters. We use two rectangular BK-7 glass slides (25mm $\times$ 60mm $\times$ 160μm) that are installed on curved aluminum sample holders of radius of curvature $R \approx 100$ mm (Fig.6.2 B). The curved rectangular substrates are positioned such that their long axes are perpendicular to each other and they can approach each other (Fig.6.2 C). This geometry is called "crossed-cylinders configuration" and frequently used in wear (friction) experiments.[231] The crossed-cylinders configuration is advantageous because its geometry is equivalent to that of a flat surface and a sphere of radius R. The apparent contact area can be calculated taking into account the applied load and the radius of curvature of the substrates. Moreover, alignment with crossed-cylinder geometry is much easier than with two flat substrates, i.e., two curved substrates come in contact at the place of 0_{th} order Newton's rings (see Section 6.3.1, Fig.6.4).

In order to set up the variable-distance-cell, the curved sample holder with one substrate (bottom sample) is initially attached to a PI-MARS piezo-stage (Fig.6.2 A, component 9). The sample holder is made so that bottom sample can be approached by an objective from beneath for optical spectroscopy (Fig.6.2 C).

The other substrate (top sample) on the other curved sample holder is installed on a different piezo-stage (PI-NanoCube), which is attached to a rectangular aluminum adapter plate. This configuration is supported by two (attached) aluminum blocks such that the top sample faces the bottom sample. We call this design bridge configuration (Fig.6.2 A, components 1-4,7).

During the installation process, the bottom sample and the bridge configuration (which includes the top sample) are consecutively installed on the same piezo-stage (PI-MARS) such that the two substrates can be moved si-

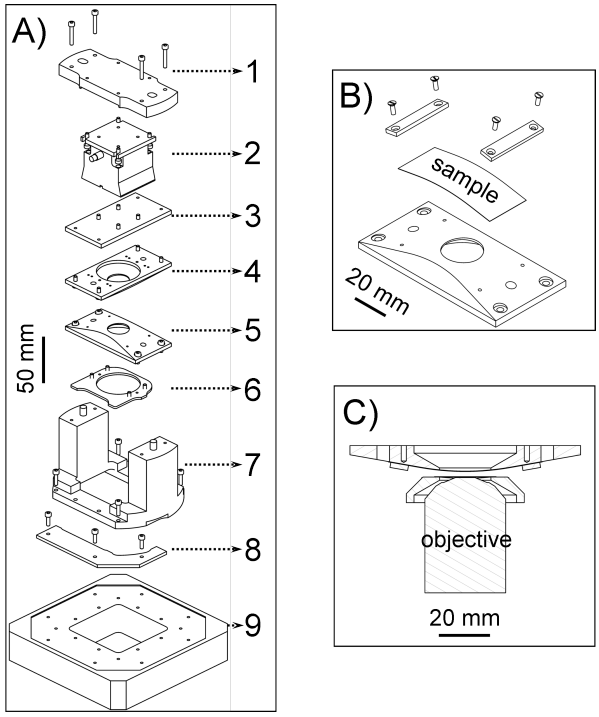

Figure 6.2: A) Components of the variable-distance-cell 1) Aluminum adapter plate to which PI-NanoCube is mounted. 2) PI-NanoCube piezo-stage. 3) Adapter plate for sample mount. 4)Top sample holder. 5)Bottom sample holder. 6)Kinematic platform for bottom sample holder. 7) (Attached) aluminum blocks. 8)Kinematic platform for bridge configuration (1-4,7). 9) PI-MARS piezo-stage. B) Sample holder and cover glass with mounting adapters C) Side view of two sample holders with microscope objective.

multaneously. The design also allows moving the top sample separately with respect to the bottom sample along three axes while keeping the position of the bottom sample the same. Moreover, two kinematic platforms (Fig.6.2 A, components 6, 8) help for precise positioning of the two samples if samples need to be installed and re-installed with high repeatability. They are convenient whenever the sample has to be removed, for example to change the objective.

After the installation of the two samples, it is necessary to find the contact area to start spectroscopy measurements. This procedure may require lateral movement of both samples for distances ranging from several 100 μm to a few millimeters. Therefore, the variable-distance cell is attached to a manual xy translation stage, which is used for coarse lateral movements of both samples with respect to the microscope objective.

During the optical study of gold nanorods, we keep the variable-distance cell in a thermocol box with thick walls ($\sim$30 mm). We use the box to minimize possible small thermal drift (a few 100 nm/K) of piezo-stages. The box partly isolates the variable-distance cell from the room, thereby minimizing

temperature variations during the optical measurements.

6.2.3 Samples

We spin-coated single gold nanorods on one glass substrate for optical microscopy measurements and we used this substrate with nanorods as the bottom sample. The gold nanorods used in this study were prepared in a seed-mediated growth method.[214] The ensemble average aspect ratio of the nanorods is about 2.2. The ensemble average width and length of the nanorods are 30 nm and 65 nm, respectively. The absorption spectrum of the nanorods suspension is shown in Fig. 6.3. An SEM image of the nanorods is shown in the inset of Fig. 6.3.

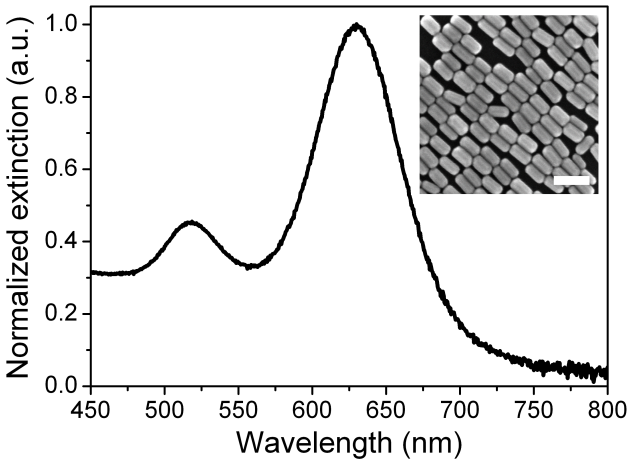

Figure 6.3: Extinction spectrum of gold nanorod suspension in water. There are two peaks. The red-most plasmon resonance corresponds to the longitudinal plasmon resonance of gold nanorods. The blue-most peak is formed by contributions from both transverse plasmon resonance of gold nanorods and residual gold nanospheres in the suspension. The inset shows an SEM image of the sample used in this study. The ensemble average width and length of the nanorods are 30 nm and 65 nm. The scale bar in the inset SEM image is 100 nm.

The top sample is prepared by spin-coating 15 mg/mL PMMA/toluene solution at 4000 rpm for 90 s. This procedure yields a ($\sim$ 25 nm) thick PMMA layer on glass, which helps to suppress stiction between the glass substrates.

Surfaces, which come in close proximity, may adhere to each other. This stiction, or static friction, arises from various forces between the two surfaces, including Van der Waals forces, electrostatic forces, and capillary forces from a liquid (water) bridge.[232] Stiction complicates the distance-dependent measurements because extra force (stiction force) is required to overcome the adhesion to enable relative motion of two surfaces. Moreover, if the two substrates are in close proximity of each other, they may uncontrollably come into contact. Capillary forces are often the dominant adhesive forces, and they are usually responsible for the stiction. They give rise, e.g. by condensation of water vapor, to a liquid bridge between the two solids. In this case, stiction may be reduced by minimizing the surface energy, the amount of liquid present at the interfaces and/or the contact area between the surfaces.[252] Surface energy can be reduced by using a hydrophobic surface[252] and the thin hydrophobic PMMA layer on the top sample was found to reduce the stiction during spectroscopy measurements.

We were also careful to minimize the dust deposition on the prepared samples. After we prepared the samples, we put them directly in a sealed box and transferred them to the laboratory. We then quickly installed them on sample holders which we installed in the variable-distance cell to conduct optical spectroscopy of single gold nanorods.

6.3 Results and discussions

6.3.1 Newton's rings and distance measurement

After samples were prepared, we installed them in the variable-distance-cell as described in Section 6.2.2. We performed single-particle spectroscopy after we found the local minimum of the distances between the two substrates. We first recorded interferences of the white light on a CCD, which showed the well-known Newton's rings (Fig. 6.4). We used a different objective (Olympus 10X, 0.4NA) because the size of the Newton's rings formed in this geometry was larger than the image sizes obtained by $60\times$ magnification objective.

We observed Newton's rings when the distance between the two substrates was less than half of the coherence length of the white light (about 2 micrometers). Newton's rings consist of colored concentric rings. This is because different wavelengths of each color constructively interfere (in re-

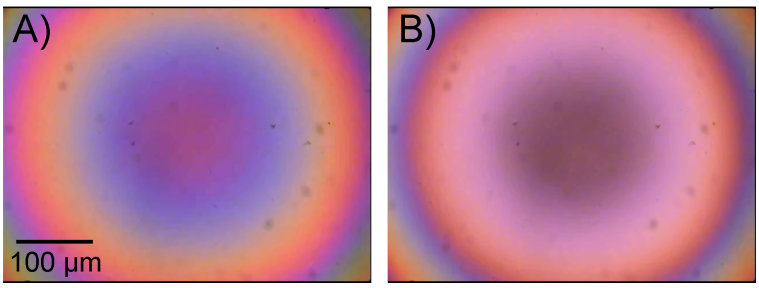

Figure 6.4: Newton's rings formed when the two substrates are in A) optical contact; B) mechanical contact. The contact area should be completely black, but a background from out-of-focus reflections remains.

flection) at different air-gap thicknesses, which increases outward from the center of the rings (Fig. 6.4 A). We used the Newton's rings to find the local-minimum distance, as the center of the Newton's rings is the point where the distance between the two crossed-curved substrates is minimum.

We first have to find the Newton's rings and overlap their center with the center of the microscope objective's field-of-view. This procedure ensures that the optical measurements will be done at (or close to) the point where the two surfaces will first get into contact. This is important in order to relate the piezo-stage translation to the gap size in a simple way. Indeed, if the same measurement is done at a point away from the point of first contact, it may not be possible to achieve contact. Moreover, because the two substrates already get into contact elsewhere, they will deform in complicated ways upon further approach, making the relation between piezo-stage displacement and gap nonlinear and uncontrollable.

At the optical contact, the two substrates do not physically touch each other. Alternating colors of Newton's rings are observed for varying distances below about 2 μm. When the distance between the two substrates is further decreased, a transition from optical contact to mechanical contact is observed (Fig. 6.4A-B). At the mechanical contact, the center area of Newton's rings turns black due to destructive interference of the white-light since the path difference is zero (Fig. 6.4 B). This dark spot is used to detect mechanical contact and check the circular shape of the contact area.[112] The size of the dark spot increases with the radius of curvature of the two glass substrates and with the load applied to the substrates.[112]

The distance between the two surfaces can be determined by record-

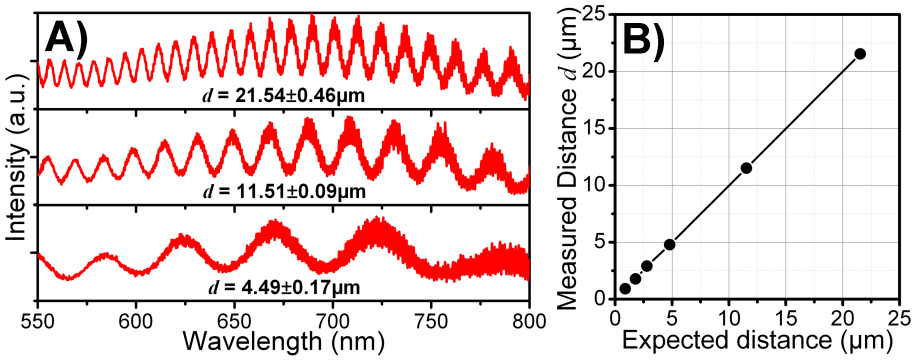

Figure 6.5: (A) Fringes of the reflected white light from the friction cell at different air-gap thickness. Distances (B) Characterization of the piezo stage movement and the distance measurement.

ing the spectrum of the reflected light (interference fringes) as shown in Fig. 6.5 A. The distance (d) is estimated from the fringe spectrum by averaging all distances obtained from each pair of consecutive peak wavelengths (λ_1 and λ_2) according to Eq. 6.1 using Matlab. For different separation distances of two substrates, the calculated distances with standard deviations of the mean are depicted in Fig. 6.5 A.

$$d = \frac{\lambda_1 \lambda_2}{2\,|\lambda_1 - \lambda_2|} \tag{6.1}$$

In order to check for the linearity of the PI-NanoCube movement, we measured the distance as described above while we were moving the top sample. We plotted the measured distance as a function of the expected distance Fig. 6.5 B. We measured the distance for six piezo-steps as shown in Fig. 6.5 B, which shows a linear movement. We relied on piezo-movement for distances below 1 μm since distances below 1 μm could not be measured by white light interferences.

We also recorded the fringes continuously while we were simultaneously moving the two samples in lateral directions using the manual xy translation stage. We followed the number of fringes in the interference spectrum so that we could find a point very close to the minimum-distance point. In order to get rid of any uncontrolled mechanical contact of the nanorod with the top substrate during the course of these lateral motions, we kept several tens of micrometers spacing between the two substrates.

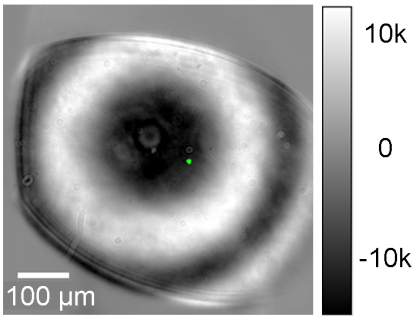

Figure 6.6: Overlap of the small green laser spot and the Newton's rings

After finding the first-contact area, we focused the laser on the same area of the bottom sample and looked for a nanorod to record its spectrum. After finishing the single-nanoparticle spectroscopy measurements, we checked the overlap again by imaging the Newton's rings (Fig.6.6). The measurement point is shown as a small green dot in Fig.6.6. In our experiments, the distance between the laser spot and the center of the Newton's ring was about 75 μm. We calculated that the distance between the two substrates at the imaging point was 30 nm when the two substrates first got in mechanical contact at the minimum-distance point. For distances lower than 30 nm, we can no longer ensure the linearity of the gap as a function of the piezo-stage movement (Fig. 6.5 B).

6.3.2 Plasmon resonance as a distance ruler

In order to characterize the response of the gold nanorod to an approaching dielectric interface, we studied its luminescence spectrum. We initially recorded the luminescence spectrum of the gold nanorod when the distance between the substrates was about 30 μm. This spectrum served as reference for infinite gap width. We had to check whether the mechanical contact led to any irreversible change of the nanorod spectrum. Therefore, we checked for changes of the spectrum and of the orientation of the nanorod after mechanical contact with the top substrate. Thus, we recorded the spectra of the nanorod at different detection polarizations before and after the substrate was in contact with the top substrate (see Fig. 6.9 B). We measured the polarization anisotropy and determined the orientation of the nanorod for both cases.

A luminescence spectrum and an image of a nanorod at about 30 μm separation of the substrates is shown in Fig. 6.7. The color scale of the luminescence image shows the luminescence count-rate of the nanorod, which was excited at 476 nm at an intensity of 360 kW/cm^2. We obtained the full-with-at-half-maximum of the luminescence spot along the x- and y-axis by a Gaussian fit. This yielded values for σ_x and σ_y of 390 nm and 340 nm for the luminescence spot, respectively. We also recorded the luminescence spectrum of the gold nanorod (Fig. 6.7). We checked that we had a single gold nanorod by looking at its spectral shape, a single Lorentzian profile (see Chapter 5).

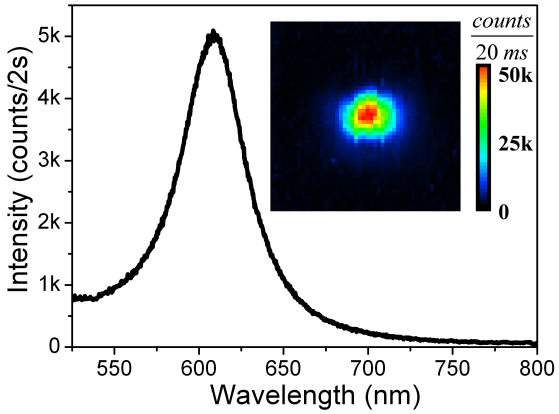

Figure 6.7: Luminescence spectrum of a single gold nanorod. The spectrum was recorded in air on glass substrate with 476 nm excitation at 360 kW/cm^2 in 2 s. The plasmon resonance of the nanorod is 608.8 nm. The inset shows the luminescence image of the nanorod, which was excited under the same conditions as of the spectrum. The size of the image is 2 μm^2 $\times$ 2 μm^2 (20ms/pixel, 40 nm pixel size).

We started to successively record the spectrum of the single gold nanorod when the spacing between the two substrates was 1.4 μm. We moved the top piezo-stage step by step, thereby moving the top sample towards the stationary bottom sample. The step size of the movement was 50 nm. Because the piezo-stage moves linearly (See Fig.6.5 B), we assume that the distance between the two substrates was decreased by 50 nm at each step. It is important to keep in mind that the linear movement could only be achieved for spacings larger than 30 nm (see Section 6.3.1, Fig. 6.6). We show the results of our experiment in Fig. 6.8 where we plot the luminescence spectra of the

same nanorod for different air-gap sizes. The arrow in the figure indicates the direction of the decreasing distance.

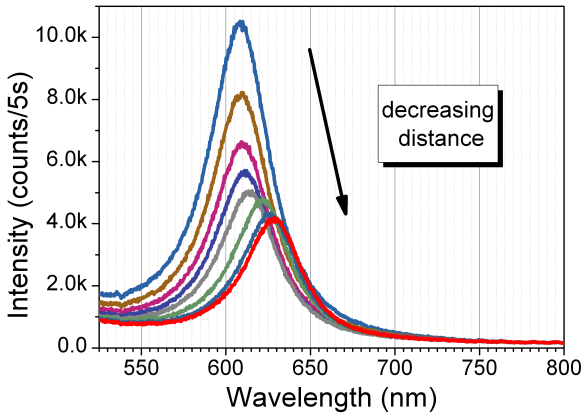

Figure 6.8: The change in the luminescence spectrum of the nanorod when the nanorod is approached with a second glass substrate from the top.

Fig. 6.8 clearly shows red-shifted plasmon resonances for decreasing distances. The observed red-shifts can be attributed to an increase in the effective refractive index.[71,73] While two substrates are getting closer, polarization charges in the approaching dielectric shield the surface plasmon field and reduce the oscillation frequency of the longitudinal plasmon. We also observe a decrease in the detected photoluminescence intensity of the nanorod for decreasing separations of the two substrates. It can be attributed to the change in the radiation pattern of the nanorod due to the approach of the second dielectric interface.[244] The radiation pattern of the dipole in an air gap between two planar interfaces depends on the dipole's orientation, the dipole's position within the gap, and the refractive index of the dielectric.[244] For large separation distances between the substrates, we can assume that the nanorod is immobilized at the air-glass interface (refractive indices $n_{glass} \approx 1.5$ and $n_{air} \approx 1$). Under this condition, most of the luminescence intensity of the nanorod is radiated towards the high-refractive-index side. When the upper interface touches the gold nanorod, the nanorod's radiation pattern becomes symmetrical and equal amounts are emitted in both glass slides.[253] The amount of light emitted in the bottom slide and detected will therefore decrease during the approach.

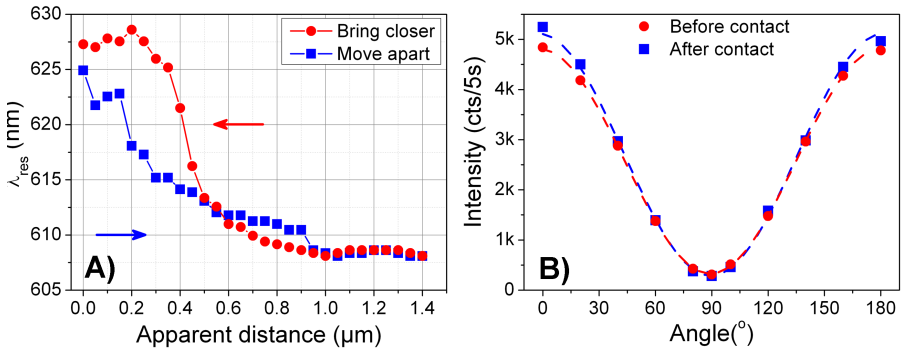

Figure 6.9: (A) The plasmon resonance wavelength λ_{res} as a function of the apparent distance between the two substrates. (B) Longitudinal plasmon resonance intensity as a function of the analyzer angle. For both images red-circles represent data which are obtained while decreasing the distance between the two substrates. The blue-square data is of experiment when the top substrate was retracted.

In Fig.6.9 A, we plot the plasmon resonance (λ_{res}) as a function of the apparent distance between the two substrates. For distances smaller than 1 μm, we estimated the apparent distance from the movement of the piezo-stage. The upper substrate was moved first towards the lower substrate until contact, then back, and spectra were recorded during the two movements to check the reversibility of the plasmon resonance wavelength change. The red points in Fig.6.9 A refer to the approach of the upper substrate, whereas the blue points were measured upon retraction. We note that the shift curve upon retraction differs from the shift curve upon approach. This may arise from hysteresis of the piezo stage, or from irreversible modifications of the substrates upon contact. For example, a capillary bridge can form, or plastic deformation of the PMMA layer can take place. For this reason, we consider only the first approach curve (red points in Fig.6.9 A). This approach curve shows a distinct shift for distances less than 1 micron, which regularly increases until the distance of 350 nm. At smaller distances, the shift remains essentially constant. The weak changes of the shift which are still observed below 350 nm may be due to interaction of the nanorod with the approaching PMMA layer, in a similar way as was observed by Novo et al.[121] We attribute the change of behavior of the shift at ∼350 nm to the first contact between the two substrates. We therefore deduce the actual distance between the substrates according to $s = [\text{Apparent distance}] - 350$ nm, and can plot the mea-

sured shift $\Delta\lambda = \lambda_{measured} - \lambda_0$ as a function of this distance s, as shown in Fig.6.10.

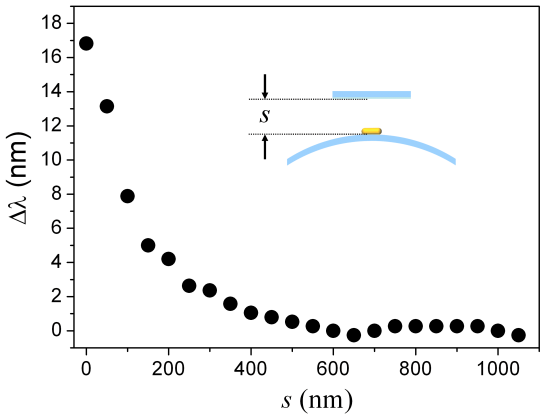

Figure 6.10: The change in the plasmon resonance wavelength ($\Delta\lambda$) as a function of the distance (s) between the two substrates.

We now discuss the curve in Fig.6.10, starting from contact and increasing the gap distance. As the air gap is increased, we find a significant blue shift of 15 nm, corresponding to a decrease of the shielding of plasmon charges by polarization charges of the upper substrate. Alternatively, this effect may be seen as an interaction between the plasmon charges and their (delayed) electrostatic image charges in the second interface. This shift reaches an almost constant value for gaps larger than 400 nm, with possibly a small oscillating contribution already observed by Hakanson et al.[250], and related to the well-known oscillations of the radiative lifetime a few wavelengths away from a dielectric interface.[244,253–256]

In order to check if there are any changes in the polarization anisotropy and the orientation of the particle before and after the two substrates get in mechanical contact, we performed polarization dependent measurements as we performed previously in Chapter 5. Shortly, we recorded the photoluminescence spectrum of the same single gold nanorod while rotating the analyzer and plotted the maximum intensity of the longitudinal plasmon resonance as a function of the detection polarization. This experiment yields the curves in Fig.6.9 B and a modulation depth of 0.9 confirming a dipole behavior. Fig.6.9 B also shows that there was no significant change in the anisotropy

and orientation of the nanorod.

6.4 Conclusions

We have investigated the effect of an approaching dielectric interface on the luminescence properties of individual gold nanorods. We observe a red-shift in the luminescence plasmon resonance wavelength of a gold nanorod while the distance between the two substrates is decreased. The significant changes in the plasmon resonance are observed for distances less than 400 nm. The maximum change in the plasmon resonance wavelength is about 15 nm. The observed effect is reversible. With this knowledge, gold nanorods can find applications in areas ranging from biology to tribology. For instance, single gold nanorods can be used for sensitive measurement of distances between dielectric surfaces and they can serve as asperity sensors. Molecular contacts can be monitored by following the changes in the luminescence (or scattering) spectra of individual nanorods. In this way, one can study the real contact area as a function of the distance between the two substrates.

Appendices

APPENDIX A

The dissipated power for some common chromophores

Here we estimate the dissipated power in photothermal experiments with single molecules. A single molecule modelled as a two-level system can release heat via two pathways: (i) through non-radiative transitions (internal conversion) from the excited state, and (ii) through vibronic relaxation prior to or after a radiative (fluorescence) transition.

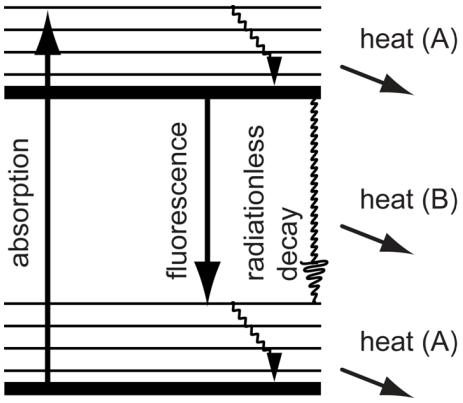

Figure A.1: Simple level scheme representing a single molecule. Absorbed energy either leads to fluorescence emission or/and can be transformed into heat. The dissipation of energy into heat goes through (A) vibronic relaxation, and (B) radiationless decay. For an organic molecule at saturation, the calculated dissipated power p_{diss} is given in Table A.1.

The power (p_{diss}) dissipated as heat into the surrounding medium by a single molecule depends on the absorbed power ($P_{abs} = \sigma_{sm} \cdot P_{heat}/A$) provided by the heating beam (or excitation) focused into the spot of area A, the fluorescence quantum yield ($\eta_F = k_r/(k_r + k_{nr})$), defined by the radiative lifetime ($\tau_r = 1/k_r$) and the non-radiative lifetime ($\tau_{nr} = 1/k_{nr}$) of the excited state of the molecule. The fluorescence lifetime ($\tau_F = 1/(k_r + k_{nr})$) is defined by the contribution of the radiative and non-radiative transitions. The dissipated power can be written as follows:

$$p_{diss} = P_{nr} + P_{fluor} = P_{abs} \cdot \eta_{diss} = P_{abs} \left[(1 - \eta_F) + \eta_F \frac{h\nu_{exc} - h\nu_{fluor}}{h\nu_{exc}} \right] \quad \text{(A.1)}$$

where ν_{exc} and ν_{fluor} are frequencies of excitation and fluorescence, $P_{heat} = P_{exc}$ is the power of the heating laser (fluorescence excitation), η_{diss} is the dissipation yield.

In the approximation of a two-level system the heating laser power required for absorption saturation P_{heat}^{sat} is given by the following equation:

$$P_{heat}^{sat} = h\nu_{heat}\frac{1}{\tau_F}\frac{A}{\sigma_{sm}} \tag{A.2}$$

Table A.1: Calculations of the dissipated power for several commercial organic molecules. τ_F is the fluorescence lifetime. η_{fluor} is the fluorescence quantum yield and η_{diss} is the dissipation yield. The absorption cross-sections for molecules (σ_{sm}) are calculated based on the manufacturer's data for extinction coefficients. Heating laser power at absorption saturation (P_{heat}^{sat}) is calculated according to Eq.A.2, assuming the 514 nm excitation light focused into a diffraction-limited spot. The dissipated power (p_{diss}) is calculated for two cases: (i) in the approximation of a saturated optical transition, and (ii) if possible, with a heating power of $P_{heat} = 5.1$mW.

						p_{diss} (nW)	
Dye	τ_F (ns)	η_{fluor}	η_{diss}	σ_{sm} (nm^2)	P_{heat}^{sat} (mW)	at saturation	with $P_{heat} =$ 5.1mW
Rh6G	4.08	0.95	0.08	0.043	0.5	0.015	0.015
Cy3	0.3	0.04	0.96	0.057	4.4	2.5	2.5
Cy5	1	0.4	0.61	0.096	0.8	0.5	0.5
BHQ1 *	0.05	-	1	0.013	117	15	0.34
ErB †	0.61	0.12	0.88	0.04	3.1	1.1	1.1
CV ‡	0.1	0.019	0.98	0.037	20	7.6	0.94

The lifetime of BHQ1 is unknown. We estimated it to 50 ps from those of similar azo dyes. The fluorescence quantum yield is also uncertain and was deduced from the lifetime. As we can see from the Table A.1, the chromophore we selected for our experiments, BHQ1, has the highest dissipated power in the saturation limit (15 nW), and Rh6G - the lowest one (0.015 nW). The dissipated powers for the experimental heating power of 5.1 mW focused into a diffraction-limited spot are about 1 nW. These small dissipated powers can be detected in photothermal experiments with an acceptable SNR, provided suitable integration time and probe power are chosen. We note that the

*black-hole-quencher[126,127,130,257]

†erythrosine[36,258]

‡crystal violet[259,260]

high heating powers required in single-molecule photothermal microscopy also require a good photostability of the absorbers. This is difficult to achieve with most of the weakly fluorescent dyes (Cy3, CV, etc.).

APPENDIX B

Organic dye nanoparticles

AFM studies of fvin nanoparticles

The results obtained from height measurements of fvin NPs is shown.

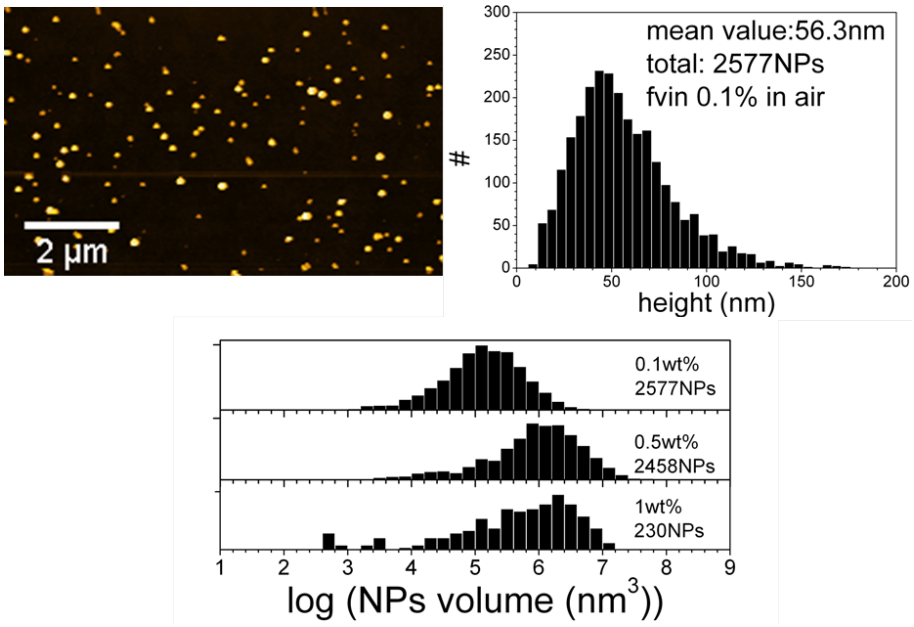

Figure B.1: A typical AFM image (top, left) and a histogram of heights (top, right) of fvin NPs prepared from a 0.1 wt% stock solution, and deposited on APTES glass by spin-coating. Measurements are done in tapping mode in air. The average diameter of fvin NPs is 56 nm, as estimated from the average height in AFM images. (Bottom) Histograms of the volumes of NPs estimated from the heights measured by AFM for various fvin concentrations.

These histograms reveal large variation of NPs volumes (more than 10 times). This observation corresponds well with the distribution of photothermal signals (Photothermal signal is proportional to the volume of NPs) obtained in the photothermal microscopy experiments. The average volume of 0.1 wt% fvin NPs is 4×10^5 nm^3.

Bulk absorption and luminescence properties of fvin dye and nanoparticles

We give information about the chemical structure of the organic dye (fvin) used for fvin nanoparticles (fvin NPs) preparation together with bulk absorption and luminescence spectra of nanoparticles.

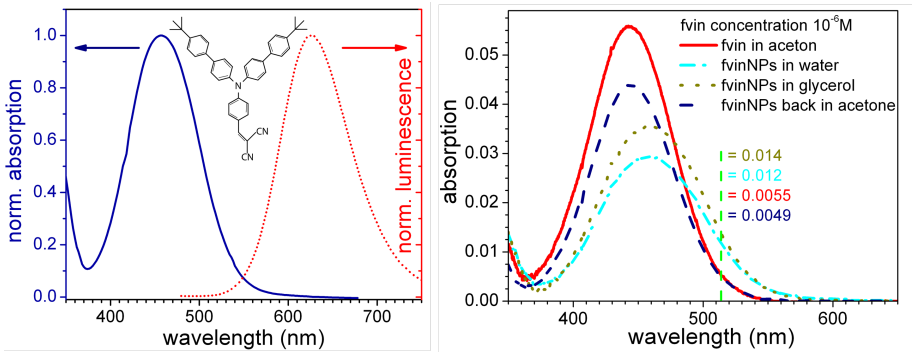

Figure B.2: Bulk spectroscopy experiment results. (left) Normalized absorption (solid) and luminescence (dot) spectra of 0.1 wt% fvin nanoparticles in water. Absorption and emission maximums are at about 450 nm and 620 nm, respectively. Since luminescence is largely red-shifted, fvin NPs do not suffer from re-absorption. Inset shows the chemical structure of the organic dye (fvin) used for nanoparticles preparation (right) Absorption spectra of fvin dye in acetone (solid), 0.1 wt% fvin NPs in water (dash-dot), 0.1 wt% fvin NPs in glycerol (dash), and 0.1 wt% fvin NPs placed back from the water solution into acetone (dash) measured at the constant concentration of fvin dye of 1.67×10^{-6} M. Absorption maximum in acetone is at 443 nm and the molar extinction coefficient is $\varepsilon(\lambda = 443\,\text{nm}) = 33400\,\text{Lmol}^{-1}\text{cm}^{-1}$. Absorption maximum in glycerol is at 458 nm and the molar extinction coefficient is $\varepsilon(\lambda = 458\,\text{nm}) = 21300\,\text{Lmol}^{-1}\text{cm}^{-1}$.

Photothermal and fluorescence microscopy of fvin NPs at low and high heating power regimes

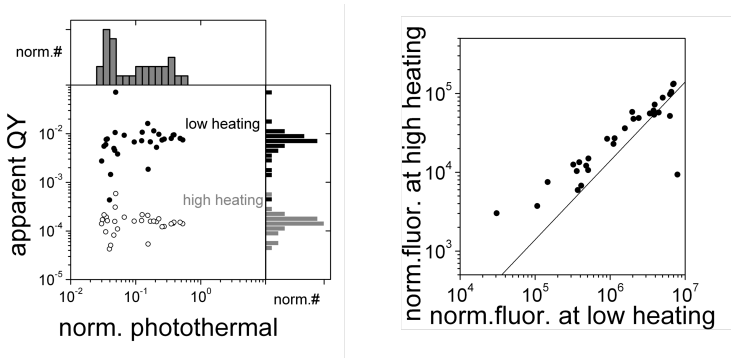

Figure B.3: (left) A scatter plot presenting apparent fluorescence quantum yield for the same data as in Fig. 3.2 C (right) A correlation of normalized fluorescence from the same fvin NPs consequently measured at two excitation regimes. A solid line presents a linear correlation with the slope of 1 on the log-log scale.

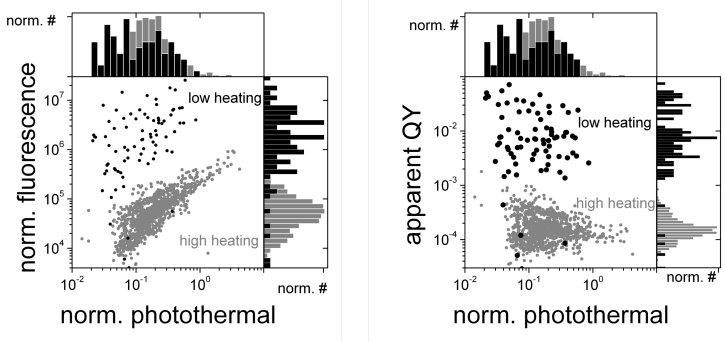

Figure B.4: (Left)A correlation of normalized fluorescence and normalized photothermal signals in two regimes of heating power: low heating power less than 2 μW (black, 83 NPs), and high heating with $85 - 128$ μW (light grey, 1268 NPs). Top and right panels show histograms for photothermal and fluorescence signals, correspondingly. (right) Apparent quantum yield as a function of normalized photothermal signal. The probe power used in the experiments is 23-56 mW. The acquisition time for fluorescence signal per pixel was 10 ms, and 3 ms lock-in integration time for the photothermal signal.

Annihilation and apparent quantum yield

We show the effect of annihilation (singlet-singlet or single-triplet) — quenching of an excited state by other excited states in the surrounding — on the luminescence count-rate of fvin nanoparticles and accordingly on the quantum yield. We observe a decrease in the quantum yield at high excitation regime.

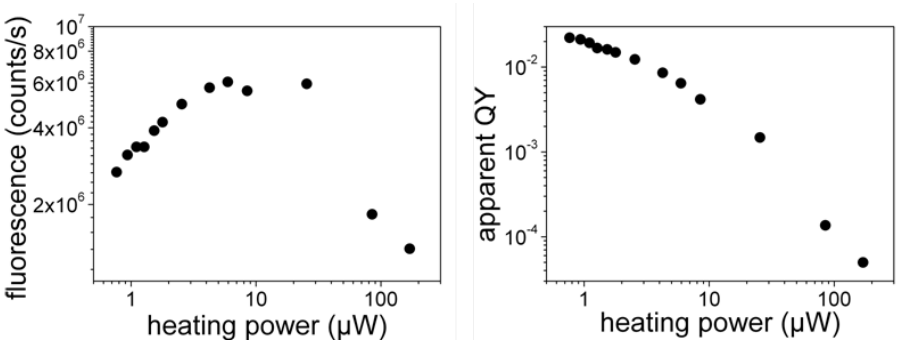

Figure B.5: (left) Fluorescence signal from individual fvin NP (0.5 wt%) as a function of the heating power. Two regions can be indicated: (i) low heating power regime with the power less than 5 μW, where fluorescence signal grows with the heating power; (ii) high heating power regime, where the apparent fluorescence signal decreases with the heating power due to combined effects of fluorescence quenching and bleaching. (Right) The calculated apparent fluorescence quantum yield as a function of the heating power. The value of the absorption cross-section for the fvin NPs is assumed to be constant in these calculations.

Calculation of number of dye molecules in a nanoparticle

We calculate the number of fvin dye molecules in fvin NPs in three independent ways.

(i) based on the photothermal signal from NPs:

The extinction coefficient of dye compound in glycerol (ε_{dye}) is 8400 $Lmol^{-1}cm^{-1}$ at 514 nm. The average isotropic absorption cross-section of a single dye (σ_{dye}) is calculated as follows:

$$\sigma_{dye}(cm^2) = 1000 \cdot \ln(10) \frac{\varepsilon_{dye}}{N_A} \sim 3.2 \times 10^{-3} nm^2$$

where N_A is the Avogadro constant.

The average absorption cross-section of individual fvin nanoparticles in glycerol is found to be $\sigma_{fvinNP} \approx 180\ nm^2$. (The absorption cross-section of each individual fvin NP was estimated by comparing photothermal signal of each fvin NP with the average photothermal signal from individual 20 nm diameter gold NPs under same illumination conditions).

We further assume that free fvin dye molecules and fvin dye molecules in nanoparticle have similar, but anisotropic absorbance. Thus, the number of dye molecules per average fvin NP is calculated as follows:

$$\frac{\sigma_{fvinNP}}{\sigma_{dye}} = \frac{180}{3.2 \times 10^{-3}} \approx 6 \times 10^4$$

(ii) based on the photoluminescence signal from NPs:

The photoluminescence quantum yield (QY) can be estimated as follows:

$$QY = \frac{N_{em}}{N_{abs} \times Det.Eff.}$$

where N_{em} is the number of the emitted photons, N_{abs} is the number of the absorbed photons, and $Det.Eff.$ is the detection efficiency (5%). The average number of photons emitted by a fvin NP is $N_{em} \sim 600$ kcounts/s for the excitation intensity of 1.7 kW/cm^2. Taking into the account the average QY of 10^{-2} for fvin NPs in the low heating power regime, the average number of absorbed photons by fvin NPs is $(N_{abs})_{fvinNPs} \sim 1.2 \times 10^9$.

The number of absorbed photons by a dye molecule is estimated as follows:

$$(N_{abs})_{dye} = \frac{\sigma_{dye} I}{h\upsilon} \approx 1.4 \times 10^5$$

where σ_{dye}, I and $h\upsilon$ are absorption cross-section of dye compound, laser intensity and energy of a photon, respectively.

Thus, the number of molecules per fvin NP is: $\frac{(N_{abs})_{fvinNPs}}{(N_{abs})_{dye}} \approx 10^4$

(iii) based on the measurements of diameters of NPs by means of AFM:

The average diameter of fvin NPs is 3.2×10^5 nm^3 (See Fig. B.1). The molecular Van der Waals volume of fvin is 0.85 nm^3. Then, the average number of molecules per fvin NP is about 4×10^5.

Table B.1: Parameters for calculations of the average number of molecules in fvin NPs.

	$\sigma(nm^2)$*	N_{abs} $(photons/s)$ †	Volume (nm^3)
fvin NP	180	1.2×10^9	4×10^5
fvin dye, isotropic	3.2×10^{-3}	1.4×10^5	0.85
$\frac{\#\ of\ molecules}{fvinNP}$	6×10^4	10^4	5×10^5

*at 514 nm

†at excitation intensity of 1.7 kW/cm^2

APPENDIX C

Single gold nanospheres

Correction factor for the luminescence efficiency

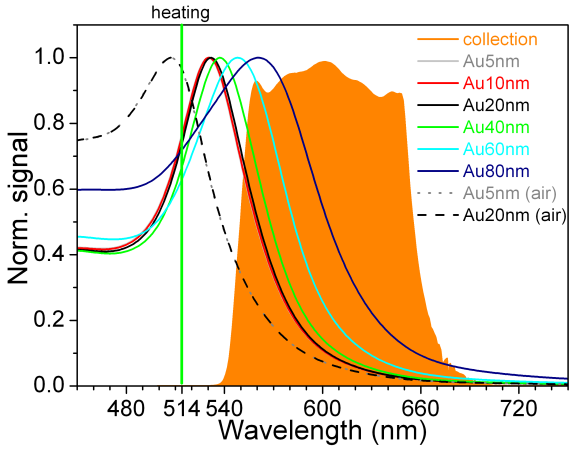

Figure C.1: Normalized absorption spectra for gold NPs of various sizes immersed in glycerol or in air (lines) and the normalized transmission spectrum of optics in fluorescence detection path (shaded area). The variable overlap between detection and emission spectra leads to adjustment factors for the quantum yield. The calculated factors for different sizes of gold nanospheres are given below in Table C.1. We assume the emission spectrum to follow the absorption on the long-wave side.

Table C.1: Correction factors for the luminescence efficiency. In order to calculate the correction factor, we compare the area under the absorption spectrum and the area of overlapping region of absorption and transmission spectrum for each nanosphere over the wavelength range of 480 nm to 800 nm.

Diameter (nm)	Norm. total abs. (a.u.)	Norm. trans. of abs. spectrum (a.u.)	QY mult. factor *
5 (air)	67	11	6.1
10	71	18	3.9
20	71	18	3.9
40	71	19	3.7
60	76	24	3.2
80	89	37	2.4
20 (air)	67	11	6.1

*The correction factor is subject of a possible error. Exact values have to be estimated based on measurements of luminescence spectra of individual NPs.

APPENDIX D

Single gold nanorods

Extinction spectrum of nanorods and nanospheres

The normalized extinction spectra of the nanorods shown in Fig. D.1 exhibit two peaks. The peak at around 515 nm-520 nm corresponds to the transverse plasmon resonance and a contribution from spherical particles present in the nanorod suspension. The red-shifted peak corresponds to the longitudinal plasmon resonance. The normalized extinction spectrum of gold nanospheres with ensemble averaged diameter of 18.5 nm has a single peak at 525 nm.

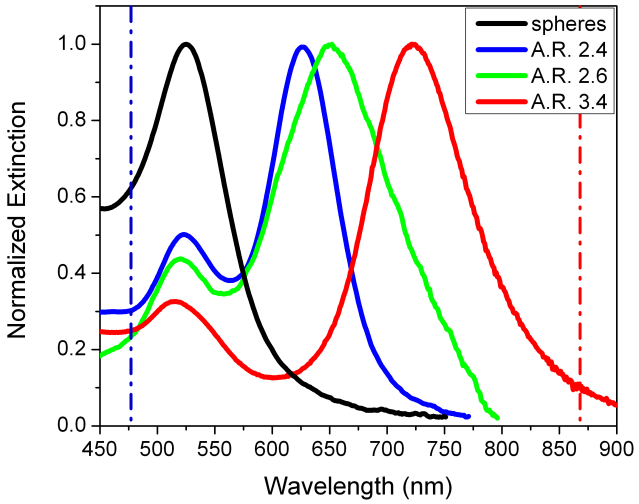

Figure D.1: Extinction spectra of nanorod and nanosphere suspensions in water measured using UV-VIS spectrophotometer. Blue, green and red solid curves correspond to suspension of nanorods with ensemble average aspect ratios (A.R.) of 2.4, 2.6 and 3.4, respectively. Black curve corresponds to the suspension of 18.5 nm diameter gold nanospheres. Dashed-dotted lines show the excitation (476 nm) and probe laser wavelengths (864 nm) used in the experiment.

Setup for combined fluorescence and scattering microscopy

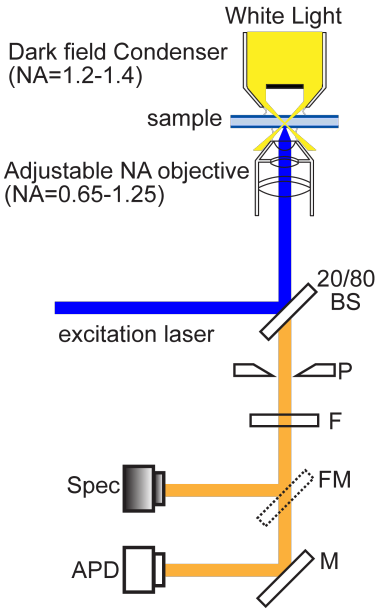

Figure D.2: Schematic of the experimental setup for correlation of scattering and luminescence signals of nanorods. M - mirror, FM - flip mirror,F - filter, P - pinhole, BS - beam splitter, Spec - spectrometer, APD - avalanche photodetector.

For luminescence imaging, the luminescence signal of nanoparticles, which was obtained by excitation at 476 nm, was spatially filtered by a 50 μm pinhole and spectrally selected by a set of longpass filters (LP02-514RU-25 and LP02-514RS-25, Semrock). The raster-scan luminescence images were recorded by focusing the luminescence signal on a single-photon-counting avalanche photodetector (SPCM-AQR-16, Perkin Elmer). The luminescence signal which was filtered out from excitation laser was also directed towards a spectrometer (SpectraPro500i) with the help of a flip mirror for spectra measurements. It was collimated and then focused on a 200 μm slit and dispersed by a 150 g/mm grating and finally detected by a liquid nitrogen cooled CCD (PI Acton SPEC10:400).

Scattering spectra were measured in a dark-field geometry using a 150 W halogen light source (Thorlabs). The experiment was performed using a microscope objective with a variable numerical aperture (NA) (Olympus, 60X oil immersion, 0.65-1.25 NA) and a dark-field condenser (Olympus, 1.2-1.4 NA). To facilitate the correlation between scattering and luminescence spectra of the same particle, we used the same focusing objective set at 1.25 NA to record the luminescence spectra or set to 0.65 NA for dark-field spectroscopy.

Temperature rise on the surface of nanorods

The maximum temperature increase on the surface of a gold nanorod is calculated by $\Delta T_{surf} = \sigma_{NR} I_{exc} / 4\pi\kappa R$ where I_{exc} is the excitation laser intensity, σ_{NR} is the absorption cross-section of the nanorod at the wavelength of the excitation laser, κ is the thermal conductivity of the medium (glycerol), and R is the equivalent radius of the particle which has absorption cross section of σ_{NR}. Temperature rises on the surface of nanorods of Fig. 5.3 (in Section 5.3) are shown in Fig.D.3. We obtained the laser intensity from the full-width-at-half-maximum σ of the photothermal and luminescence spots along the x- and y-axis by a Gaussian fit. This yielded values for σ_x and σ_y of 260 nm and 340 nm for photothermal spots and 320 nm and 360 nm for the luminescence spots.

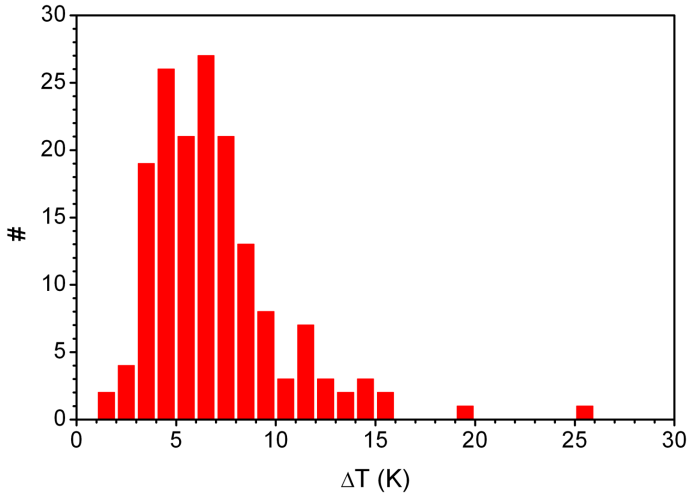

Figure D.3: The histogram of the laser-induced ΔT_{surf} on nanoparticles shown in Fig. 5.3 (in Section 5.3). The average surface temperature is $\Delta T_{surf,av} = 7 \pm 3$ K.

Signature of clustered particles

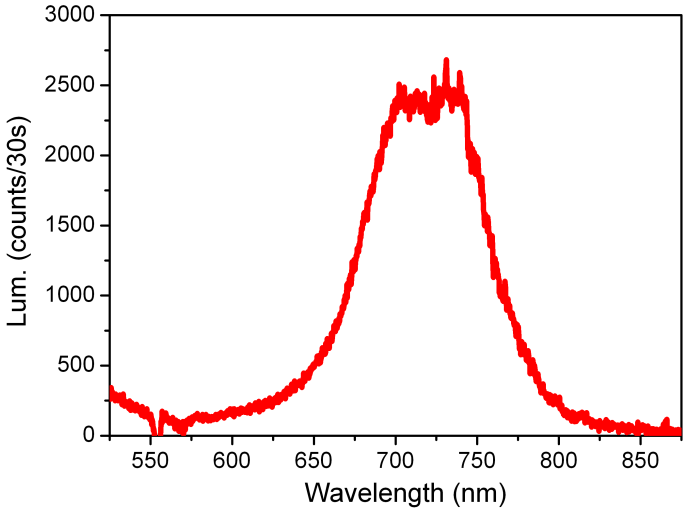

Figure D.4: An example of luminescence spectrum which does not belong to a single particle.

The shape and width of luminescence spectra provides us information to distinguish single Au nanorod from aggregates. The luminescence spectrum shows a non-Lorentzian shape or double peak when it belongs to aggregated nanorods.

An example of control experiments to ensure there is no reshaping of particles

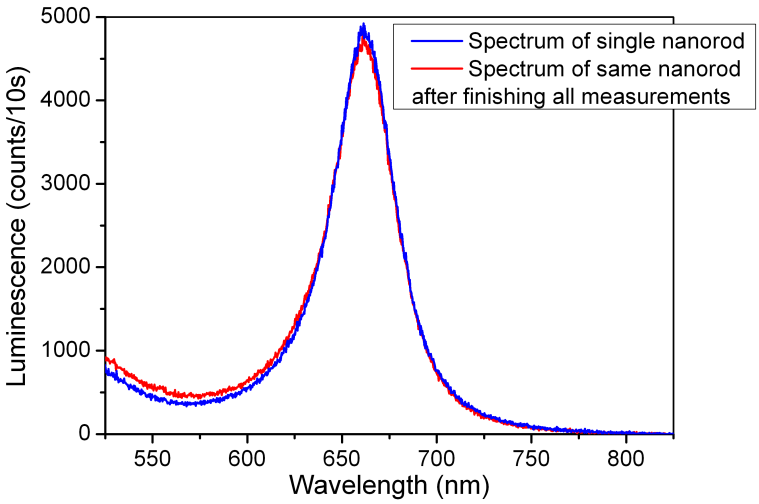

Figure D.5: The luminescence spectrum of a single gold nanorod before and after performing all optical measurements. This has been checked for each sample to ensure there was no significant reshaping of the particles for the measurements of the QY.

Excitation power dependence of photothermal and luminescence signal

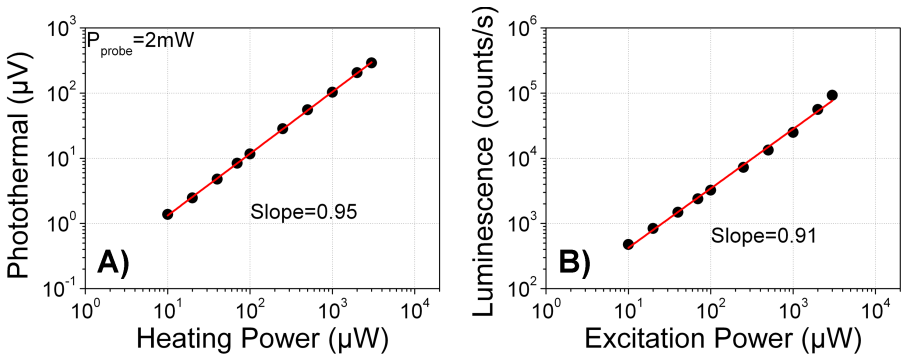

Figure D.6: Power dependence of (A) photothermal and (B) luminescence signal. The linear relationship between the excitation power and the luminescence intensity confirms that the observed luminescence is one-photon luminescence.

Transmittance of optics and the detection efficiency

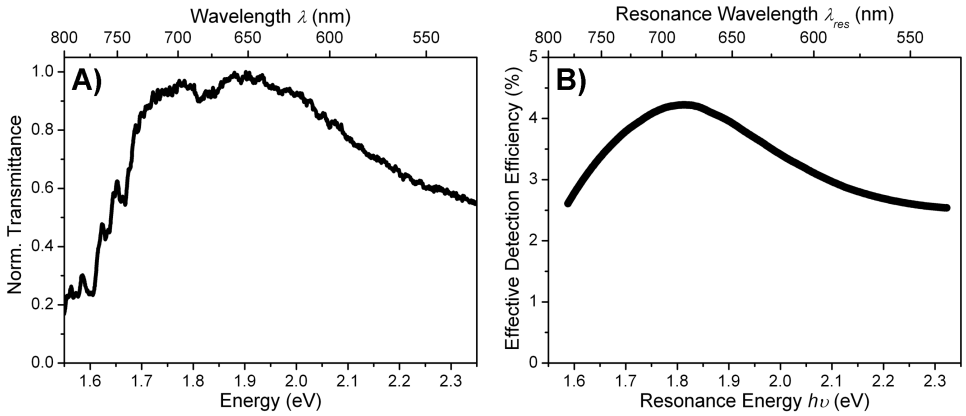

Figure D.7: (A) Normalized transmittance of optics with spectrometer efficiency, $T(\lambda) \times F(\lambda)$, as a function of photon energy (wavelength - top axis). (B) Calculated effective detection efficiency of setup, $\Pi_{setup}(\lambda_{res})$, as a function of nanorod plasmon resonance energy (resonance wavelength - top axis).

In order to obtain the luminescence spectrum of a nanorod, $I(\lambda)$, the measured spectrum, $S(\lambda)$, was corrected for the transmission of optics, $T(\lambda)$, including the spectrometer efficiency, $F(\lambda)$, as follows:

$$I(\lambda) = \frac{S(\lambda) - B(\lambda)}{T(\lambda) \times F(\lambda)}$$

where $S(\lambda)$ is the measured spectrum of a nanorod, $B(\lambda)$ is the background signal and $T(\lambda) \times F(\lambda)$ is the normalized transmittance of optics including the efficiency of the spectrometer.

For the calculation of the quantum yield, we used the detection efficiency of setup, $\Pi_{setup}(\lambda_{res})$ which was calculated as follows:

$$\Pi_{setup}(\lambda_{res}) = \frac{5\%}{C(\lambda_{res})}; C(\lambda_{res}) = \frac{\int I(\lambda) d\lambda}{\int I(\lambda) T(\lambda) A(\lambda) d\lambda}$$

where $C(\lambda_{res})$ is the calculated correction factor for a nanorod with luminescence spectrum $I(\lambda)$ and plasmon resonance λ_{res}. $T(\lambda)$ is the transmission of optics and $A(\lambda)$ is the efficiency of APD.

Volume effect on QY

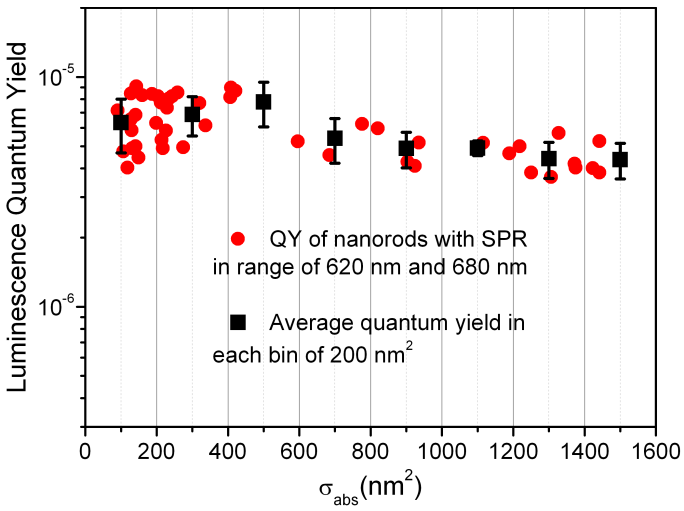

Figure D.8: Luminescence QY as a function of absorption cross-section of nanorods with similar surface plasmon resonance in range of 620 nm and 680 nm. Red-filled-circles are data of individual nanorods. Black-filled-squares are the averages of QY in bins of 200 nm^2 where error bars show the standard deviation of the mean.

Medium effect on the luminescence spectrum of a single gold nanorod

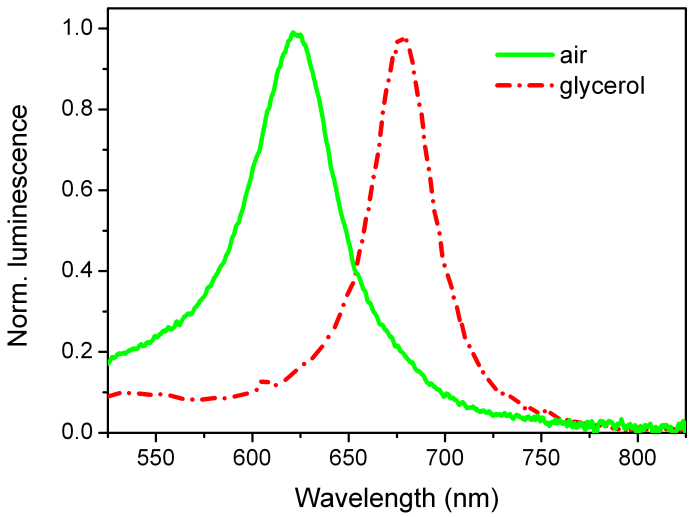

Figure D.9: Photoluminescence spectra of a single gold nanorod in air (green-solid line) and in glycerol (red dashed-dotted line). The plasmon wavelengths are 625 nm and 680 nm in air and in glycerol, respectively. The excitation wavelength is 514 nm.

We observed a plasmon peak shift of ∼55 nm when the medium was changed from air to glycerol. The observed shift is due to the change of the effective refractive index from 1.25 (glass-air interface) to 1.5 (glass-glycerol interface) and is close to the expected difference of ∼50 nm.

Volume dependence of the ”green” emission component

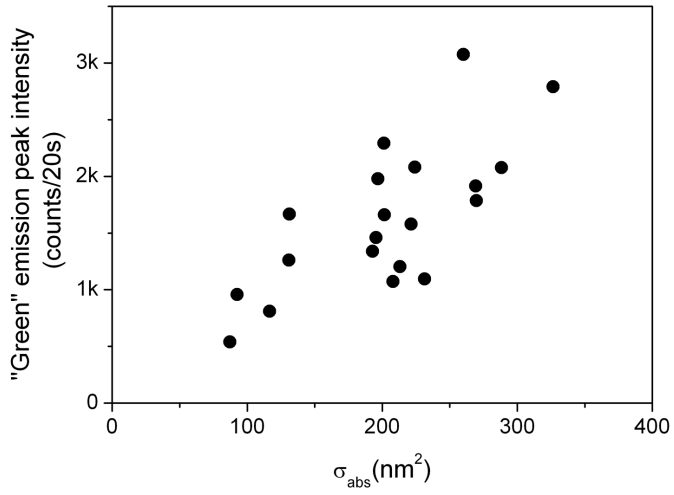

Figure D.10: Intensity of the ”green” component contribution as a function of the calculated absorption cross section of the nanorods. The ”green” emission peak intensity was obtained from the mean of luminescence intensities over 525 nm and 530 nm for each particle. The absorption cross sections of nanorods were obtained as described in the main text. The ”green” component we observe is peaked at 500 nm, and its intensity scales as the volume of the particle (as deduced from photothermal measurements).

Bibliography

[1] J. Jo, J. S. Yu, T. M. Lee, and D. S. Kim, *Fabrication of Printed Organic Thin-Film Transistors Using Roll Printing*, Japanese Journal of Applied Physics **48**, 04C181 (2009).

[2] S. A. Odom, S. R. Parkin, and J. E. Anthony, *Tetracene derivatives as potential red emitters for organic LEDs*, Organic Letters **5**, 4245 (2003).

[3] B. Lounis and M. Orrit, *Single-photon sources*, Reports on Progress in Physics **68**, 1129 (2005).

[4] T. H. Lee, P. Kumar, A. Mehta, K. W. Xu, R. M. Dickson, and M. D. Barnes, *Oriented semiconducting polymer nanostructures as on-demand room-temperature single-photon sources*, Applied Physics Letters **85**, 100 (2004).

[5] A. J. Shields, *Semiconductor quantum light sources*, Nature Photonics **1**, 215 (2007).

[6] E. Knill, R. Laflamme, and G. J. Milburn, *A scheme for efficient quantum computation with linear optics*, Nature **409**, 46 (2001).

[7] D. Bouwmeester, A. K. Ekert, and A. Zeilinger, *The physics of quantum information: quantum cryptography, quantum teleportation, quantum computation* (Springer, Berlin, 2000).

[8] N. Gisin, G. G. Ribordy, W. Tittel, and H. Zbinden, *Quantum cryptography*, Reviews of Modern Physics **74**, 145 (2002).

[9] S. Schultz, D. R. Smith, J. J. Mock, and D. A. Schultz, *Single-target molecule detection with nonbleaching multicolor optical immunolabels*, Proceedings of the National Academy of Sciences of the United States of America **97**, 996 (2000).

[10] C. J. Cogswell, D. K. Hamilton, and C. J. R. Sheppard, *Color Confocal Reflection Microscopy Using Red, Green and Blue Lasers*, Journal of Microscopy-Oxford **165**, 103 (1992).

[11] X. L. Nan, P. A. Sims, and X. S. Xie, *Organelle tracking in a living cell with microsecond time resolution and nanometer spatial precision*, ChemPhysChem **9**, 707

(2008).

[12] M. Horisberger and J. Rosset, *Colloidal Gold, a Useful Marker for Transmission and Scanning Electron-Microscopy*, Journal of Histochemistry and Cytochemistry **25**, 295 (1977).

[13] C. Sonnichsen, B. M. Reinhard, J. Liphardt, and A. P. Alivisatos, *A molecular ruler based on plasmon coupling of single gold and silver nanoparticles*, Nature Biotechnology **23**, 741 (2005).

[14] R. T. Hill, J. J. Mock, A. Hucknall, S. D. Wolter, N. M. Jokerst, D. R. Smith, and A. Chilkoti, *Plasmon Ruler with Angstrom Length Resolution*, ACS Nano **6**, 9237 (2012).

[15] G. J. Nusz, S. M. Marinakos, A. C. Curry, A. Dahlin, F. Hook, A. Wax, and A. Chilkoti, *Label-free plasmonic detection of biomolecular binding by a single gold nanorod*, Analytical Chemistry **80**, 984 (2008).

[16] C. J. Orendorff, S. C. Baxter, E. C. Goldsmith, and C. J. Murphy, *Light scattering from gold nanorods: tracking material deformation*, Nanotechnology **16**, 2601 (2005).

[17] C. J. Murphy, A. M. Gole, J. W. Stone, P. N. Sisco, A. M. Alkilany, E. C. Goldsmith, and S. C. Baxter, *Gold Nanoparticles in Biology: Beyond Toxicity to Cellular Imaging*, Accounts of Chemical Research **41**, 1721 (2008).

[18] C. Loo, A. Lin, L. Hirsch, M. H. Lee, J. Barton, N. J. Halas, J. West, and R. Drezek, *Nanoshell-enabled photonics-based imaging and therapy of cancer*, Technology in Cancer Research and Treatment **3**, 33 (2004).

[19] X. H. Huang, P. K. Jain, I. H. El-Sayed, and M. A. El-Sayed, *Gold nanoparticles: interesting optical properties and recent applications in cancer diagnostic and therapy*, Nanomedicine **2**, 681 (2007).

[20] S. Jain, D. G. Hirst, and J. M. O'Sullivan, *Gold nanoparticles as novel agents for cancer therapy*, British Journal of Radiology **85**, 101 (2012).

[21] I. H. El-Sayed, X. H. Huang, and M. A. El-Sayed, *Selective laser photo-thermal therapy of epithelial carcinoma using anti-EGFR antibody conjugated gold nanoparticles*, Cancer Letters **239**, 129 (2006).

[22] P. Zijlstra, J. W. M. Chon, and M. Gu, *Five-dimensional optical recording mediated by surface plasmons in gold nanorods*, Nature **459**, 410 (2009).

[23] A. Tcherniak, J. W. Ha, S. Dominguez-Medina, L. S. Slaughter, and S. Link, *Probing a Century Old Prediction One Plasmonic Particle at a Time*, Nano Letters **10**, 1398 (2010).

[24] F. Kulzer, T. Xia, and M. Orrit, *Single Molecules as Optical Nanoprobes for Soft and*

Complex Matter, Angewandte Chemie-International Edition **49**, 854 (2010).

[25] P. Zijlstra, P. M. R. Paulo, and M. Orrit, *Optical detection of single non-absorbing molecules using the surface plasmon resonance of a gold nanorod*, Nature Nanotechnology **7**, 379 (2012).

[26] G. F. Wang, W. Sun, Y. Luo, and N. Fang, *Resolving Rotational Motions of Nano-objects in Engineered Environments and Live Cells with Gold Nanorods and Differential Interference Contrast Microscopy*, Journal of the American Chemical Society **132**, 16417 (2010).

[27] C. Veigel and C. F. Schmidt, *Moving into the cell: single-molecule studies of molecular motors in complex environments*, Nature Reviews Molecular Cell Biology **12**, 163 (2011).

[28] D. Lasne, G. A. Blab, S. Berciaud, M. Heine, L. Groc, D. Choquet, L. Cognet, and B. Lounis, *Single nanoparticle photothermal tracking (SNaPT) of 5-nm gold beads in live cells*, Biophysical Journal **91**, 4598 (2006).

[29] B. van den Broek, B. Ashcroft, T. H. Oosterkamp, and J. van Noort, *Parallel Nanometric 3D Tracking of Intracellular Gold Nanorods Using Multifocal Two-Photon Microscopy*, Nano Letters **13**, 980 (2013).

[30] Y. Gu, X. W. Di, W. Sun, G. F. Wang, and N. Fang, *Three-Dimensional Super-Localization and Tracking of Single Gold Nanoparticles in Cells*, Analytical Chemistry **84**, 4111 (2012).

[31] A. M. Funston, C. Novo, T. J. Davis, and P. Mulvaney, *Plasmon Coupling of Gold Nanorods at Short Distances and in Different Geometries*, Nano Letters **9**, 1651 (2009).

[32] L. Slaughter, W. S. Chang, and S. Link, *Characterizing Plasmons in Nanoparticles and Their Assemblies with Single Particle Spectroscopy*, Journal of Physical Chemistry Letters **2**, 2015 (2011).

[33] M. Orrit and J. Bernard, *Single Pentacene Molecules Detected by Fluorescence Excitation in a Para-Terphenyl Crystal*, Physical Review Letters **65**, 2716 (1990).

[34] P. Tamarat, A. Maali, B. Lounis, and M. Orrit, *Ten years of single-molecule spectroscopy*, Journal of Physical Chemistry A **104**, 1 (2000).

[35] W. E. Moerner and D. P. Fromm, *Methods of single-molecule fluorescence spectroscopy and microscopy*, Review of Scientific Instruments **74**, 3597 (2003).

[36] J. R. Lakowicz, *Principles of Fluorescence Spectroscopy* (Springer, New York, 2006).

[37] C. Joo, H. Balci, Y. Ishitsuka, C. Buranachai, and T. Ha, *Advances in single-molecule fluorescence methods for molecular biology*, Annual Review of Biochem-

istry **77**, 51 (2008).

[38] D. Boyer, P. Tamarat, A. Maali, B. Lounis, and M. Orrit, *Photothermal imaging of nanometer-sized metal particles among scatterers*, Science **297**, 1160 (2002).

[39] S. Berciaud, L. Cognet, G. A. Blab, and B. Lounis, *Photothermal heterodyne imaging of individual nonfluorescent nanoclusters and nanocrystals*, Physical Review Letters **93**, 257402 (2004).

[40] F. V. Ignatovich and L. Novotny, *Real-time and background-free detection of nanoscale particles*, Physical Review Letters **96**, 013901 (2006).

[41] M. A. van Dijk, M. Lippitz, and M. Orrit, *Far-field optical microscopy of single metal manoparticies*, Accounts of Chemical Research **38**, 594 (2005).

[42] M. A. van Dijk, A. L. Tchebotareva, M. Orrit, M. Lippitz, S. Berciaud, D. Lasne, L. Cognet, and B. Lounis, *Absorption and scattering microscopy of single metal nanoparticles*, Physical Chemistry Chemical Physics **8**, 3486 (2006).

[43] A. J. Gesquiere, T. Uwada, T. Asahi, H. Masuhara, and P. F. Barbara, *Single molecule spectroscopy of organic dye nanoparticles*, Nano Letters **5**, 1321 (2005).

[44] D. Tuncel and H. V. Demir, *Conjugated polymer nanoparticles*, Nanoscale **2**, 484 (2010).

[45] W. E. Moerner, *Optical measurements of single molecules in cells*, TrAC-Trends in Analytical Chemistry **22**, 544 (2003).

[46] A. Yildiz, J. N. Forkey, S. A. McKinney, T. Ha, Y. E. Goldman, and P. R. Selvin, *Myosin V walks hand-over-hand: Single fluorophore imaging with 1.5-nm localization*, Science **300**, 2061 (2003).

[47] W. E. Moerner and M. Orrit, *Illuminating single molecules in condensed matter*, Science **283**, 1670 (1999).

[48] J. Kirstein, B. Platschek, C. Jung, R. Brown, T. Bein, and C. Brauchle, *Exploration of nanostructured channel systems with single-molecule probes*, Nature Materials **6**, 303 (2007).

[49] A. Yildiz, M. Tomishige, R. D. Vale, and P. R. Selvin, *Kinesin walks hand-over-hand*, Science **303**, 676 (2004).

[50] A. Schob, F. Cichos, J. Schuster, and C. von Borczyskowski, *Reorientation and translation of individual dye molecules in a polymer matrix*, European Polymer Journal **40**, 1019 (2004).

[51] M. Orrit, *Chemical and physical aspects of charge transfer in the fluorescence intermittency of single molecules and quantum dots*, Photochemical and Photobiological Sciences **9**, 637 (2010).

[52] J. Schuster, F. Cichos, and C. von Borczyskowski, *Blinking of single molecules in various environments*, Optics and Spectroscopy **98**, 712 (2005).

[53] R. Zondervan, F. Kulzer, M. A. Kol'chenko, and M. Orrit, *Photobleaching of rhodamine 6G in poly(vinyl alcohol) at the ensemble and single-molecule levels*, Journal of Physical Chemistry A **108**, 1657 (2004).

[54] H. Kasai, H. S. Nalwa, H. Oikawa, S. Okada, H. Matsuda, N. Minami, A. Kakuta, K. Ono, A. Mukoh, and H. Nakanishi, *A Novel Preparation Method of Organic Microcrystals*, Japanese Journal of Applied Physics Part 2-Letters **31**, L1132 (1992).

[55] M. Breton, G. Prevel, J. F. Audibert, R. Pansu, P. Tauc, B. Le Pioufle, O. Francais, J. Fresnais, J. F. Berret, and E. Ishow, *Solvatochromic dissociation of noncovalent fluorescent organic nanoparticles upon cell internalization*, Physical Chemistry Chemical Physics **13**, 13268 (2011).

[56] A. Gaiduk, M. Yorulmaz, E. Ishow, and M. Orrit, *Absorption, Luminescence, and Sizing of Organic Dye Nanoparticles and of Patterns Formed Upon Dewetting*, ChemPhysChem **13**, 946 (2012).

[57] E. Ishow, R. Guillot, G. Buntinx, and O. Poizat, *Photoinduced intramolecular charge-transfer dynamics of a red-emitting dicyanovinyl-based triarylamine dye in solution*, Journal of Photochemistry and Photobiology A: Chemistry **234**, 27 (2012).

[58] H. Yao, *Prospects for Organic Dye Nanoparticles*, Advanced Fluorescence Reporters in Chemistry and Biology II **9**, 285 (2010).

[59] A. Wakamiya, K. Mori, and S. Yamaguchi, *3-Boryl-2,2 '-bithiophene as a versatile core skeleton for full-color highly emissive organic solids*, Angewandte Chemie-International Edition **46**, 4273 (2007).

[60] Z. Y. Tian, W. W. Wu, and A. D. Q. Li, *Photoswitchable Fluorescent Nanoparticles: Preparation, Properties and Applications*, ChemPhysChem **10**, 2577 (2009).

[61] A. Jana, K. S. P. Devi, T. K. Maiti, and N. D. P. Singh, *Perylene-3-ylmethanol: Fluorescent Organic Nanoparticles as a Single-Component Photoresponsive Nanocarrier with Real-Time Monitoring of Anticancer Drug Release*, Journal of the American Chemical Society **134**, 7656 (2012).

[62] A. Stannard, *Dewetting-mediated pattern formation in nanoparticle assemblies*, Journal of Physics-Condensed Matter **23**, 083001 (2011).

[63] E. Rabani, D. R. Reichman, P. L. Geissler, and L. E. Brus, *Drying-mediated self-assembly of nanoparticles*, Nature **426**, 271 (2003).

[64] P. Muller-Buschbaum, *Dewetting and pattern formation in thin polymer films as*

investigated in real and reciprocal space, Journal of Physics-Condensed Matter **15**, R1549 (2003).

[65] Y. Shirota and H. Kageyama, *Charge carrier transporting molecular materials and their applications in devices*, Chemical Reviews **107**, 953 (2007).

[66] B. J. Schwartz, *Conjugated polymers as molecular materials: How chain conformation and film morphology influence energy transfer and interchain interactions*, Annual Review of Physical Chemistry **54**, 141 (2003).

[67] M. Yorulmaz, S. Khatua, P. Zijlstra, A. Gaiduk, and M. Orrit, *Luminescence Quantum Yield of Single Gold Nanorods*, Nano Letters **12**, 4385 (2012).

[68] H. Petrova, J. P. Juste, I. Pastoriza-Santos, G. V. Hartland, L. M. Liz-Marzan, and P. Mulvaney, *On the temperature stability of gold nanorods: comparison between thermal and ultrafast laser-induced heating*, Physical Chemistry Chemical Physics **8**, 814 (2006).

[69] P. Zijlstra, J. W. M. Chon, and M. Gu, *White light scattering spectroscopy and electron microscopy of laser induced melting in single gold nanorods*, Physical Chemistry Chemical Physics **11**, 5915 (2009).

[70] R. Ishmukhametov, T. Hornung, D. Spetzler, and W. D. Frasch, *Direct observation of stepped proteolipid ring rotation in E. coli FoF1-ATP synthase*, Embo Journal **29**, 3911 (2010).

[71] P. Zijlstra and M. Orrit, *Single metal nanoparticles: optical detection, spectroscopy and applications*, Reports on Progress in Physics **74**, 106401 (2011).

[72] C. F. Bohren and D. R. Huffman, *Absorption and Scattering of Light by Small Particles* (Wiley, New York, 1998).

[73] S. Link, M. B. Mohamed, and M. A. El-Sayed, *Simulation of the optical absorption spectra of gold nanorods as a function of their aspect ratio and the effect of the medium dielectric constant*, Journal of Physical Chemistry B **103**, 3073 (1999).

[74] O. Schubert, J. Becker, L. Carbone, Y. Khalavka, T. Provalska, I. Zins, and C. Sonnichsen, *Mapping the polarization pattern of plasmon modes reveals nanoparticle symmetry*, Nano Letters **8**, 2345 (2008).

[75] T. Zuchner, A. V. Failla, A. Hartschuh, and A. J. Meixner, *A novel approach to detect and characterize the scattering patterns of single Au nanoparticles using confocal microscopy*, Journal of Microscopy-Oxford **229**, 337 (2008).

[76] T. Zuchner, A. V. Failla, M. Steiner, and A. J. Meixner, *Probing dielectric interfaces on the nanoscale with elastic scattering patterns of single gold nanorods*, Optics Express **16**, 14635 (2008).

[77] T. Klar, M. Perner, S. Grosse, G. von Plessen, W. Spirkl, and J. Feldmann,

Surface-plasmon resonances in single metallic nanoparticles, Physical Review Letters **80**, 4249 (1998).

[78] H. J. Chen, X. S. Kou, Z. Yang, W. H. Ni, and J. F. Wang, *Shape- and size-dependent refractive index sensitivity of gold nanoparticles*, Langmuir **24**, 5233 (2008).

[79] J. N. Anker, W. P. Hall, O. Lyandres, N. C. Shah, J. Zhao, and R. P. Van Duyne, *Biosensing with plasmonic nanosensors*, Nature Materials **7**, 442 (2008).

[80] K. M. Mayer, F. Hao, S. Lee, P. Nordlander, and J. H. Hafner, *A single molecule immunoassay by localized surface plasmon resonance*, Nanotechnology **21**, (2010).

[81] K. M. Mayer and J. H. Hafner, *Localized Surface Plasmon Resonance Sensors*, Chemical Reviews **111**, 3828 (2011).

[82] A. Gaiduk, M. Yorulmaz, P. V. Ruijgrok, and M. Orrit, *Room-Temperature Detection of a Single Molecule's Absorption by Photothermal Contrast*, Science **330**, 353 (2010).

[83] S. Berciaud, L. Cognet, P. Poulin, R. B. Weisman, and B. Lounis, *Absorption spectroscopy of individual single-walled carbon nanotubes*, Nano Letters **7**, 1203 (2007).

[84] P. R. Selvin and T. Ha, *Single Molecule Techniques: A Laboratory Manual* (CSHL Press, Cold Spring Harbor, New York, 2008).

[85] R. Zsigmondy and J. Alexander, *Colloids and the Ultramicroscope: A Manual of Colloid Chemistry and Ultramicroscopy* (J. Wiley, New York, 1909), (tr. by Jerome Alexander).

[86] K. Lindfors, T. Kalkbrenner, P. Stoller, and V. Sandoghdar, *Detection and spectroscopy of gold nanoparticles using supercontinuum white light confocal microscopy*, Physical Review Letters **93**, 037401 (2004).

[87] X. Hong, E. M. P. H. van Dijk, S. R. Hall, J. B. Gotte, N. F. van Hulst, and H. Gersen, *Background-Free Detection of Single 5 nm Nanoparticles through Interferometric Cross-Polarization Microscopy*, Nano Letters **11**, 541 (2011).

[88] P. Kukura, M. Celebrano, A. Renn, and V. Sandoghdar, *Imaging a Single Quantum Dot When It Is Dark*, Nano Letters **9**, 926 (2009).

[89] C. Sonnichsen, T. Franzl, T. Wilk, G. von Plessen, J. Feldmann, O. Wilson, and P. Mulvaney, *Drastic reduction of plasmon damping in gold nanorods*, Physical Review Letters **88**, 077402 (2002).

[90] A. Gaiduk, P. V. Ruijgrok, M. Yorulmaz, and M. Orrit, *Detection limits in photothermal microscopy*, Chemical Science **1**, 343 (2010).

[91] S. S. Chong, W. Min, and X. S. Xie, *Ground-State Depletion Microscopy: Detection Sensitivity of Single-Molecule Optical Absorption at Room Temperature*, Journal of Physical Chemistry Letters **1**, 3316 (2010).

[92] P. Kukura, M. Celebrano, A. Renn, and V. Sandoghdar, *Single-Molecule Sensitivity in Optical Absorption at Room Temperature*, Journal of Physical Chemistry Letters **1**, 3323 (2010).

[93] J. Hwang, M. M. Fejer, and W. E. Moerner, *Scanning interferometric microscopy for the detection of ultrasmall phase shifts in condensed matter*, Physical Review A **73**, 021802 (2006).

[94] W. Min, S. J. Lu, S. S. Chong, R. Roy, G. R. Holtom, and X. S. Xie, *Imaging chromophores with undetectable fluorescence by stimulated emission microscopy*, Nature **461**, 1105 (2009).

[95] S. Berciaud, D. Lasne, G. A. Blab, L. Cognet, and B. Lounis, *Photothermal heterodyne imaging of individual metallic nanoparticles: Theory versus experiment*, Physical Review B **73**, 045424 (2006).

[96] S. Berciaud, L. Cognet, and B. Lounis, *Photothermal absorption spectroscopy of individual semiconductor nanocrystals*, Nano Letters **5**, 2160 (2005).

[97] M. Tokeshi, M. Uchida, A. Hibara, T. Sawada, and T. Kitamori, *Determination of subyoctomole amounts of nonfluorescent molecules using a thermal lens microscope: Subsingle molecule determination*, Analytical Chemistry **73**, 2112 (2001).

[98] S. E. Bialkowski, *Photothermal Spectroscopy Methods for Chemical Analysis* (Wiley, New York, 1996).

[99] S. Berciaud, L. Cognet, and B. Lounis, *Luminescence decay and the absorption cross section of individual single-walled carbon nanotubes*, Physical Review Letters **101**, 077402 (2008).

[100] W. E. Moerner and L. Kador, *Optical-Detection and Spectroscopy of Single Molecules in a Solid*, Physical Review Letters **62**, 2535 (1989).

[101] L. Kador, T. Latychevskaia, A. Renn, and U. P. Wild, *Absorption spectroscopy on single molecules in solids*, Journal of Chemical Physics **111**, 8755 (1999).

[102] J. Y. P. Butter, B. Hecht, B. R. Crenshaw, and C. Weder, *Absorption and fluorescence of single molecules*, Journal of Chemical Physics **125**, 154710 (2006).

[103] I. Gerhardt, G. Wrigge, P. Bushev, G. Zumofen, M. Agio, R. Pfab, and V. Sandoghdar, *Strong extinction of a laser beam by a single molecule*, Physical Review Letters **98**, 033601 (2007).

[104] M. Celebrano, P. Kukura, A. Renn, and V. Sandoghdar, *Single-molecule imaging by optical absorption*, Nature Photonics **5**, 95 (2011).

[105] B. N. J. Persson, *Theory of rubber friction and contact mechanics*, Journal of Chemical Physics **115**, 3840 (2001).

[106] F. W. Delrio, M. P. De Boer, J. A. Knapp, E. D. Reedy, P. J. Clews, and M. L. Dunn, *The role of van der Waals forces in adhesion of micromachined surfaces*, Nature Materials **4**, 629 (2005).

[107] Y. F. Mo, K. T. Turner, and I. Szlufarska, *Friction laws at the nanoscale*, Nature **457**, 1116 (2009).

[108] R. Gonzalez, L. Caballero, J. Pavez, and F. Melo, *Adhesion, Stretching, and Electrical Charge Assessment of Dermatan Sulfate Molecules by Colloidal Probes*, Langmuir **28**, 9506 (2012).

[109] F. P. Bowden and D. Tabor, *The friction and Lubrication of Solids* (Clarendon, Oxford, 1950).

[110] J. A. Greenwood and J. B. P. Williamson, *Contact of Nominally Flat Surfaces*, Proceedings of the Royal Society of London Series A: Mathematical and Physical Sciences **295**, 300 (1966).

[111] A. Ovcharenko, G. Halperin, I. Etsion, and M. Varenberg, *A novel test rig for in situ and real time optical measurement of the contact area evolution during pre-sliding of a spherical contact*, Tribology Letters **23**, 55 (2006).

[112] B. A. Krick, J. R. Vail, B. N. J. Persson, and W. G. Sawyer, *Optical In Situ Micro Tribometer for Analysis of Real Contact Area for Contact Mechanics, Adhesion, and Sliding Experiments*, Tribology Letters **45**, 185 (2012).

[113] M. Kopycinska-Muller, R. H. Geiss, and D. C. Hurley, *Contact mechanics and tip shape in AFM-based nanomechanical measurements*, Ultramicroscopy **106**, 466 (2006).

[114] C. Girard, C. Joachim, and S. Gauthier, *The physics of the near-field*, Reports on Progress in Physics **63**, 893 (2000).

[115] S. A. Maier and H. A. Atwater, *Plasmonics: Localization and guiding of electromagnetic energy in metal/dielectric structures*, Journal of Applied Physics **98**, (2005).

[116] L. S. Jung, C. T. Campbell, T. M. Chinowsky, M. N. Mar, and S. S. Yee, *Quantitative interpretation of the response of surface plasmon resonance sensors to adsorbed films*, Langmuir **14**, 5636 (1998).

[117] B. Liedberg, I. Lundstrom, and E. Stenberg, *Principles of Biosensing with an Extended Coupling Matrix and Surface-Plasmon Resonance*, Sensors and Actuators B-Chemical **11**, 63 (1993).

[118] P. K. Jain, W. Y. Huang, and M. A. El-Sayed, *On the universal scaling behavior of the distance decay of plasmon coupling in metal nanoparticle pairs: A plasmon ruler*

equation, Nano Letters **7**, 2080 (2007).

[119] L. M. Tian, E. Chen, N. Gandra, A. Abbas, and S. Singamaneni, *Gold Nanorods as Plasmonic Nanotransducers: Distance-Dependent Refractive Index Sensitivity*, Langmuir **28**, 17435 (2012).

[120] N. Liu, M. Hentschel, T. Weiss, A. P. Alivisatos, and H. Giessen, *Three-Dimensional Plasmon Rulers*, Science **332**, 1407 (2011).

[121] C. Novo, A. M. Funston, I. Pastoriza-Santos, L. M. Liz-Marzan, and P. Mulvaney, *Influence of the medium refractive index on the optical properties of single gold triangular prisms on a substrate*, Journal of Physical Chemistry C **112**, 3 (2008).

[122] R. A. Keller, W. P. Ambrose, P. M. Goodwin, J. H. Jett, J. C. Martin, and M. Wu, *Single molecule fluorescence analysis in solution*, Applied Spectroscopy **50**, A12 (1996).

[123] G. Wrigge, J. Hwang, I. Gerhardt, G. Zumofen, and V. Sandoghdar, *Exploring the limits of single emitter detection in fluorescence and extinction*, Optics Express **16**, 17358 (2008).

[124] P. M. R. Paulo, A. Gaiduk, F. Kulzer, S. F. G. Krens, H. P. Spaink, T. Schmidt, and M. Orrit, *Photothermal Correlation Spectroscopy of Gold Nanoparticles in Solution*, Journal of Physical Chemistry C **113**, 11451 (2009).

[125] S. Link and M. A. El-Sayed, *Spectroscopic determination of the melting energy of a gold nanorod*, Journal of Chemical Physics **114**, 2362 (2001).

[126] T. Susdorf, A. K. Bansal, A. Penzkofer, S. L. Guo, and J. M. Shi, *Absorption and emission spectroscopic characterization of some azo dyes and a diamino-maleonitrile dye*, Chemical Physics **333**, 49 (2007).

[127] G. Wang, F. Gan, J. Wang, L. Yang, G. Wang, and Z. Xu, *Spectroscopic investigations of a novel push-pull azo compound embedded in rigid polymer*, Journal of Physics and Chemistry of Solids **63**, 501 (2002).

[128] A. Arbouet, D. Christofilos, N. Del Fatti, F. Vallee, J. R. Huntzinger, L. Arnaud, P. Billaud, and M. Broyer, *Direct measurement of the single-metal-cluster optical absorption*, Physical Review Letters **93**, 127401 (2004).

[129] V. V. Didenko and E. by, *Methods in Molecular Biology: Fluorescent Energy Transfer Nucleic Acid Probes: Designs and Protocols*, (2006).

[130] S. A. E. Marras, F. R. Kramer, and S. Tyagi, *Efficiencies of fluorescence resonance energy transfer and contact-mediated quenching in oligonucleotide probes*, Nucleic Acids Research **30**, e122 (2002).

[131] S. J. Lu, W. Min, S. S. Chong, G. R. Holtom, and X. S. Xie, *Label-free imaging of heme proteins with two-photon excited photothermal lens microscopy*, Applied

Physics Letters **96**, 113701 (2010).

[132] S. W. Stahl, E. M. Puchner, and H. E. Gaub, *Photothermal cantilever actuation for fast single-molecule force spectroscopy*, Review of Scientific Instruments **80**, 073702 (2009).

[133] X. H. Huang, S. Neretina, and M. A. El-Sayed, *Gold Nanorods: From Synthesis and Properties to Biological and Biomedical Applications*, Advanced Materials **21**, 4880 (2009).

[134] T. K. Sau, A. L. Rogach, F. Jackel, T. A. Klar, and J. Feldmann, *Properties and Applications of Colloidal Nonspherical Noble Metal Nanoparticles*, Advanced Materials **22**, 1805 (2010).

[135] G. V. Hartland, *Optical Studies of Dynamics in Noble Metal Nanostructures*, Chemical Reviews **111**, 3858 (2011).

[136] A. Ibanez, S. Maximov, A. Guin, C. Chaillout, and P. L. Baldeck, *Controlled nanocrystallization of organic molecules in sol-gel glasses*, Advanced Materials **10**, 1540 (1998).

[137] T. Asahi, T. Sugiyama, and H. Masuhara, *Laser Fabrication and Spectroscopy of Organic Nanoparticles*, Accounts of Chemical Research **41**, 1790 (2008).

[138] H. S. Peng, C. F. Wu, Y. F. Jiang, S. H. Huang, and J. McNeill, *Highly luminescent Eu3+ chelate nanoparticles prepared by a reprecipitation-encapsulation method*, Langmuir **23**, 1591 (2007).

[139] D. K. Bwambok, B. El-Zahab, S. K. Challa, M. Li, L. Chandler, G. A. Baker, and I. M. Warner, *Near-Infrared Fluorescent NanoGUMBOS for Biomedical Imaging*, ACS Nano **3**, 3854 (2009).

[140] S. Santra, J. S. Xu, K. M. Wang, and W. H. Tan, *Luminescent nanoparticle probes for bioimaging*, Journal of Nanoscience and Nanotechnology **4**, 590 (2004).

[141] P. Sharma, S. Brown, G. Walter, S. Santra, and B. Moudgil, *Nanoparticles for bioimaging*, Advances in Colloid and Interface Science **123**, 471 (2006).

[142] M. C. Cross and P. C. Hohenberg, *Pattern-Formation Outside of Equilibrium*, Reviews of Modern Physics **65**, 851 (1993).

[143] M. Suvakov and B. Tadic, *Modeling collective charge transport in nanoparticle assemblies*, Journal of Physics-Condensed Matter **22**, 163201 (2010).

[144] J. C. Crocker, *Nanomaterials: Golden handshake*, Nature **451**, 528 (2008).

[145] D. A. Vanden Bout, J. Kerimo, D. A. Higgins, and P. F. Barbara, *Near-field optical studies of thin-film mesostructured organic materials*, Accounts of Chemical Research **30**, 204 (1997).

[146] J. D. McNeill, D. B. O'Connor, and P. F. Barbara, *Imaging organic device function with near-field scanning optical microscopy*, Journal of Chemical Physics **112**, 7811 (2000).

[147] E. Ishow, A. Brosseau, G. Clavier, K. Nakatani, P. Tauc, C. Fiorini-Debuisschert, S. Neveu, O. Sandre, and A. Leaustic, *Multicolor Emission of Small Molecule-Based Amorphous Thin Films and Nanoparticles with a Single Excitation Wavelength*, Chemistry of Materials **20**, 6597 (2008).

[148] F. Wang, M. Y. Han, K. Y. Mya, Y. B. Wang, and Y. H. Lai, *Aggregation-driven growth of size-tunable organic nanoparticles using electronically altered conjugated polymers*, Journal of the American Chemical Society **127**, 10350 (2005).

[149] W. S. Chang, J. W. Ha, L. S. Slaughter, and S. Link, *Plasmonic nanorod absorbers as orientation sensors*, Proceedings of the National Academy of Sciences of the United States of America **107**, 2781 (2010).

[150] L. H. Xiao, Y. X. Qiao, Y. He, and E. S. Yeung, *Three Dimensional Orientational Imaging of Nanoparticles with Darkfield Microscopy*, Analytical Chemistry **82**, 5268 (2010).

[151] J. E. Pawley, *Handbook of Biological Confocal Microscopy* (Plenum, New York, 1995).

[152] B. Valeur, *Molecular Fluorescence: Principles and Applications* (Wiley-VCH Verlag, Berlin, Germany, 2002).

[153] A. Gaiduk, R. Kuhnemuth, S. Felekyan, M. Antonik, W. Becker, V. Kudryavtsev, C. Sandhagen, and C. A. M. Seidel, *Fluorescence detection with high time resolution: From optical microscopy to simultaneous force and fluorescence spectroscopy*, Microscopy Research and Technique **70**, 433 (2007).

[154] S. W. Hell, *Far-Field Optical Nanoscopy*, in Single Molecule Spectroscopy in Chemistry, Physics and Biology 365 (2009).

[155] A. Gaiduk, P. V. Ruijgrok, M. Yorulmaz, and M. Orrit, *Making gold nanoparticles fluorescent for simultaneous absorption and fluorescence detection on the single particle level*, Physical Chemistry Chemical Physics **13**, 149 (2011).

[156] A. Gaiduk, M. Yorulmaz, and M. Orrit, *Correlated Absorption and Photoluminescence of Single Gold Nanoparticles*, ChemPhysChem **12**, 1536 (2011).

[157] C. McNeill, *Imaging the Domain Structure of Organic Semiconductor Films*, Journal of Polymer Science Part B-Polymer Physics **49**, 909 (2011).

[158] R. K. Lammi and P. F. Barbara, *Influence of chain length on exciton migration to low-energy sites in single fluorene copolymers*, Photochemical and Photobiological Sciences **4**, 95 (2005).

[159] H. Z. Lin, Y. X. Tian, K. Zapadka, G. Persson, D. Thomsson, O. Mirzov, P. O. Larsson, J. Widengren, and I. G. Scheblykin, *Fate of Excitations in Conjugated Polymers: Single-Molecule Spectroscopy Reveals Nonemissive "Dark" Regions in MEH-PPV Individual Chains*, Nano Letters **9**, 4456 (2009).

[160] J. Yu, D. H. Hu, and P. F. Barbara, *Unmasking electronic energy transfer of conjugated polymers by suppression of O(2) quenching*, Science **289**, 1327 (2000).

[161] H. Z. Lin, S. R. Tabaei, D. Thomsson, O. Mirzov, P. O. Larsson, and I. G. Scheblykin, *Fluorescence blinking, exciton dynamics, and energy transfer domains in single conjugated polymer chains*, Journal of the American Chemical Society **130**, 7042 (2008).

[162] S. Masuo, T. Vosch, M. Cotlet, P. Tinnefeld, S. Habuchi, T. D. M. Bell, I. Oesterling, D. Beljonne, B. Champagne, K. Mullen, M. Sauer, J. Hofkens, and F. C. De Schryver, *Multichromophoric dendrimers as single-photon sources: A single-molecule study*, Journal of Physical Chemistry B **108**, 16686 (2004).

[163] S. Jordens, G. De Belder, M. Lor, G. Schweitzer, M. Van der Auweraer, T. Weil, A. Herrmann, U. M. Wiesler, K. Mullen, and F. C. De Schryver, *Generation dependent singlet-singlet annihilation within multichromophoric dendrimers studied by polychromatic transient absorption*, Photochemical and Photobiological Sciences **2**, 1118 (2003).

[164] F. C. De Schryver, T. Vosch, M. Cotlet, M. Van der Auweraer, K. Mullen, and J. Hofkens, *Energy dissipation in multichromophoric single dendrimers*, Accounts of Chemical Research **38**, 514 (2005).

[165] P. Tinnefeld, J. Hofkens, D. P. Herten, S. Masuo, T. Vosch, M. Cotlet, S. Habuchi, K. Mullen, F. C. De Schryver, and M. Sauer, *Higher-excited-state photophysical pathways in multichromophoric systems revealed by single-molecule fluorescence spectroscopy*, ChemPhysChem **5**, 1786 (2004).

[166] T. Christ, F. Kulzer, T. Weil, K. Mullen, T. Basche, H. Masuhara, and K. Satoshi, *in Nanophotonics: Intergrating Photochemistry, Optics, and Nano/Bio-Materials Studies, (Eds.: H. Masuhara, S. Kawata)* (Elsevier, Amsterdam, 2005).

[167] , See Electronic Supporting Information (ESI) available free of charge .

[168] E. Piovesan, L. De Boni, E. Ishow, and C. R. Mendonca, *Two-photon absorption properties of a novel class of triarylamine compounds*, Chemical Physics Letters **498**, 277 (2010).

[169] A. Stannard, C. P. Martin, E. Pauliac-Vaujour, P. Moriarty, and U. Thiele, *Dual-scale pattern formation in nanoparticle assemblies*, Journal of Physical Chemistry C **112**, 15195 (2008).

[170] B. Sandnes, H. A. Knudsen, K. J. Maloy, and E. G. Flekkoy, *Labyrinth patterns in confined granular-fluid systems*, Physical Review Letters **99**, 038001 (2007).

[171] G. L. Ge and L. Brus, *Evidence for spinodal phase separation in two-dimensional nanocrystal self-assembly*, Journal of Physical Chemistry B **104**, 9573 (2000).

[172] A. J. Archer, M. J. Robbins, and U. Thiele, *Dynamical density functional theory for the dewetting of evaporating thin films of nanoparticle suspensions exhibiting pattern formation*, Physical Review E **81**, 021602 (2010).

[173] C. Stowell and B. A. Korgel, *Self-assembled honeycomb networks of gold nanocrystals*, Nano Letters **1**, 595 (2001).

[174] C. J. Murphy, T. K. Sau, A. M. Gole, C. J. Orendorff, J. X. Gao, L. Gou, S. E. Hunyadi, and T. Li, *Anisotropic metal nanoparticles: Synthesis, assembly, and optical applications*, Journal of Physical Chemistry B **109**, 13857 (2005).

[175] Z. D. Wang, J. Q. Zhang, J. M. Ekman, P. J. A. Kenis, and Y. Lu, *DNA-Mediated Control of Metal Nanoparticle Shape: One-Pot Synthesis and Cellular Uptake of Highly Stable and Functional Gold Nanoflowers*, Nano Letters **10**, 1886 (2010).

[176] A. L. Tchebotareva, M. A. van Dijk, P. V. Ruijgrok, V. Fokkema, M. H. S. Hesselberth, M. Lippitz, and M. Orrit, *Acoustic and Optical Modes of Single Dumbbells of Gold Nanoparticles*, ChemPhysChem **10**, 111 (2009).

[177] E. Absil, G. Tessier, D. Fournier, M. Gross, and M. Atlan, *Full field imaging and spectroscopy of individual gold nanoparticles*, European Physical Journal-Applied Physics **43**, 155 (2008).

[178] A. V. Failla, H. Qian, H. Qian, A. Hartschuh, and A. J. Meixner, *Orientational imaging of subwavelength au particles with higher order laser modes*, Nano Letters **6**, 1374 (2006).

[179] V. Jacobsen, P. Stoller, C. Brunner, V. Vogel, and V. Sandoghdar, *Interferometric optical detection and tracking of very small gold nanoparticles at a water-glass interface*, Optics Express **14**, 405 (2006).

[180] E. Dulkeith, T. Niedereichholz, T. A. Klar, J. Feldmann, G. von Plessen, D. I. Gittins, K. S. Mayya, and F. Caruso, *Plasmon emission in photoexcited gold nanoparticles*, Physical Review B **70**, 205424 (2004).

[181] O. P. Varnavski, T. Goodson, M. B. Mohamed, and M. A. El-Sayed, *Femtosecond excitation dynamics in gold nanospheres and nanorods*, Physical Review B **72**, 235405 (2005).

[182] M. R. Beversluis, A. Bouhelier, and L. Novotny, *Continuum generation from single gold nanostructures through near-field mediated intraband transitions*, Physical Review B **68**, 115433 (2003).

[183] Z. K. Wu and R. C. Jin, *On the Ligand's Role in the Fluorescence of Gold Nanoclusters*, Nano Letters **10**, 2568 (2010).

[184] C. Zhou, C. Sun, M. X. Yu, Y. P. Qin, J. G. Wang, M. Kim, and J. Zheng, *Luminescent Gold Nanoparticles with Mixed Valence States Generated from Dissociation of Polymeric Au(I) Thiolates*, Journal of Physical Chemistry C **114**, 7727 (2010).

[185] N. Schaeffer, B. Tan, C. Dickinson, M. J. Rosseinsky, A. Laromaine, D. W. McComb, M. M. Stevens, Y. Q. Wang, L. Petit, C. Barentin, D. G. Spiller, A. I. Cooper, and R. Levy, *Fluorescent or not? Size-dependent fluorescence switching for polymer-stabilized gold clusters in the 1.1-1.7 nm size range*, Chemical Communications 3986 (2008).

[186] J. P. Wilcoxon, J. E. Martin, F. Parsapour, B. Wiedenman, and D. F. Kelley, *Photoluminescence from nanosize gold clusters*, Journal of Chemical Physics **108**, 9137 (1998).

[187] L. Cognet, S. Berciaud, D. Lasne, and B. Lounis, *Photothermal methods for single nonluminescent nano-objects*, Analytical Chemistry **80**, 2288 (2008).

[188] S. Berciaud, L. Cognet, P. Tamarat, and B. Lounis, *Observation of intrinsic size effects in the optical response of individual gold nanoparticles*, Nano Letters **5**, 515 (2005).

[189] R. Radnz, D. Rings, K. Kroy, and F. Cichos, *Hot Brownian Particles and Photothermal Correlation Spectroscopy*, Journal of Physical Chemistry A **113**, 1674 (2009).

[190] V. Octeau, L. Cognet, L. Duchesne, D. Lasne, N. Schaeffer, D. G. Fernig, and B. Lounis, *Photothermal Absorption Correlation Spectroscopy*, ACS Nano **3**, 345 (2009).

[191] E. Absil, G. Tessier, M. Gross, M. Atlan, N. Warnasooriya, S. Suck, M. Coppey-Moisan, and D. Fournier, *Photothermal heterodyne holography of gold nanoparticles*, Optics Express **18**, 780 (2010).

[192] X. Wu, T. Ming, X. Wang, P. N. Wang, J. F. Wang, and J. Y. Chen, *High-Photoluminescence-Yield Gold Nanocubes: For Cell Imaging and Photothermal Therapy*, ACS Nano **4**, 113 (2010).

[193] Z. Q. Peng, T. Walther, and K. Kleinermanns, *Photofragmentation of phase-transferred gold nanoparticles by intense pulsed laser light*, Journal of Physical Chemistry B **109**, 15735 (2005).

[194] G. V. Hartland, *Coherent excitation of vibrational modes in metallic nanoparticles*, Annual Review of Physical Chemistry **57**, 403 (2006).

[195] K. L. McGilvray, M. R. Decan, D. S. Wang, and J. C. Scaiano, *Facile photochem-*

ical synthesis of unprotected aqueous gold nanoparticles, Journal of the American Chemical Society **128**, 15980 (2006).

[196] M. Sakamoto, T. Tachikawa, M. Fujitsuka, and T. Majima, *Photoreactivity of As-Fabricated Au Clusters at the Single-Cluster Level*, Journal of the American Chemical Society **131**, 6 (2009).

[197] M. Sakamoto, T. Tachikawa, M. Fujitsuka, and T. Majima, *Photochemical Reactivity of Gold Clusters: Dependence on Size and Spin Multiplicity*, Langmuir **25**, 13888 (2009).

[198] J. Stehr, C. Hrelescu, R. A. Sperling, G. Raschke, M. Wunderlich, A. Nichtl, D. Heindl, K. Krzinger, W. J. Parak, T. A. Klar, and J. Feldmann, *Gold NanoStoves for microsecond DNA melting analysis*, Nano Letters **8**, 619 (2008).

[199] M. Reismann, J. C. Bretschneider, G. von Plessen, and U. Simon, *Reversible photothermal melting of DNA in DNA-gold-nanoparticle networks*, Small **4**, 607 (2008).

[200] A. S. Urban, M. Fedoruk, M. R. Horton, J. Radler, F. D. Stefani, and J. Feldmann, *Controlled Nanometric Phase Transitions of Phospholipid Membranes by Plasmonic Heating of Single Gold Nanoparticles*, Nano Letters **9**, 2903 (2009).

[201] R. A. Holser, *Thermal analysis of glycerol citrate/starch blends*, Journal of Applied Polymer Science **110**, 1498 (2008).

[202] A. M. Ruppert, J. D. Meeldijk, B. W. M. Kuipers, B. H. Erne, and B. M. Weckhuysen, *Glycerol etherification over highly active CaO-based materials: New mechanistic aspects and related colloidal particle formation*, Chemistry - A European Journal **14**, 2016 (2008).

[203] M. Yorulmaz, A. Kiraz, and A. L. Demirel, *Motion of Single Terrylene Molecules in Confined Channels of Poly(butadiene)-Poly(ethylene oxide) Diblock Copolymer*, Journal of Physical Chemistry B **113**, 9640 (2009).

[204] T. Li, Q. Li, Y. Xu, X. J. Chen, Q. F. Dai, H. Y. Liu, S. Lan, S. L. Tie, and L. J. Wu, *Three-Dimensional Orientation Sensors by Defocused Imaging of Gold Nanorods through an Ordinary Wide-Field Microscope*, ACS Nano **6**, 1268 (2012).

[205] N. J. Durr, T. Larson, D. K. Smith, B. A. Korgel, K. Sokolov, and A. Ben-Yakar, *Two-photon luminescence imaging of cancer cells using molecularly targeted gold nanorods*, Nano Letters **7**, 941 (2007).

[206] A. Tcherniak, S. Dominguez-Medina, W. S. Chang, P. Swanglap, L. S. Slaughter, C. F. Landes, and S. Link, *One-Photon Plasmon Luminescence and Its Application to Correlation Spectroscopy as a Probe for Rotational and Translational Dynamics of Gold Nanorods*, Journal of Physical Chemistry C **115**, 15938 (2011).

[207] H. F. Wang, T. B. Huff, D. A. Zweifel, W. He, P. S. Low, A. Wei, and J. X. Cheng, *In vitro and in vivo two-photon luminescence imaging of single gold nanorods*, Proceedings of the National Academy of Sciences of the United States of America **102**, 15752 (2005).

[208] A. Mooradian, *Photoluminescence of Metals*, Physical Review Letters **22**, 185 (1969).

[209] P. Apell, R. Monreal, and S. Lundqvist, *Photoluminescence of Noble-Metals*, Physica Scripta **38**, 174 (1988).

[210] G. T. Boyd, Z. H. Yu, and Y. R. Shen, *Photoinduced Luminescence from the Noble-Metals and Its Enhancement on Roughened Surfaces*, Physical Review B **33**, 7923 (1986).

[211] M. Kusunoki, *Theory of Photoluminescence in Metals*, Progress of Theoretical Physics **47**, 728 (1972).

[212] G. T. Boyd, T. Rasing, J. R. R. Leite, and Y. R. Shen, *Local-Field Enhancement on Rough Surfaces of Metals, Semimetals, and Semiconductors with the Use of Optical 2nd-Harmonic Generation*, Physical Review B **30**, 519 (1984).

[213] M. B. Mohamed, V. Volkov, S. Link, and M. A. El-Sayed, *The 'lightning' gold nanorods: fluorescence enhancement of over a million compared to the gold metal*, Chemical Physics Letters **317**, 517 (2000).

[214] B. Nikoobakht and M. A. El-Sayed, *Preparation and growth mechanism of gold nanorods (NRs) using seed-mediated growth method*, Chemistry of Materials **15**, 1957 (2003).

[215] P. B. Johnson and R. W. Christy, *Optical-Constants of Noble-Metals*, Physical Review B **6**, 4370 (1972).

[216] S. Inasawa, M. Sugiyama, and Y. Yamaguchi, *Laser-induced shape transformation of gold nanoparticles below the melting point: The effect of surface melting*, Journal of Physical Chemistry B **109**, 3104 (2005).

[217] A. Bouhelier, R. Bachelot, G. Lerondel, S. Kostcheev, P. Royer, and G. P. Wiederrecht, *Surface plasmon characteristics of tunable photoluminescence in single gold nanorods*, Physical Review Letters **95**, 267405 (2005).

[218] M. Z. Liu, P. Guyot-Sionnest, T. W. Lee, and S. K. Gray, *Optical properties of rod-like and bipyramidal gold nanoparticles from three-dimensional computations*, Physical Review B **76**, 235428 (2007).

[219] K. Imura, T. Nagahara, and H. Okamoto, *Plasmon mode imaging of single gold nanorods*, Journal of the American Chemical Society **126**, 12730 (2004).

[220] B. Bhushan, *Nanotribology and nanomechanics of MEMS/NEMS and*

BioMEMS/BioNEMS materials and devices, Microelectronic Engineering **84**, 387 (2007).

[221] B. Bhushan, J. N. Israelachvili, and U. Landman, *Nanotribology - Friction, Wear and Lubrication at the Atomic-Scale*, Nature **374**, 607 (1995).

[222] D. Berman, A. Erdemir, and A. V. Sumant, *Few layer graphene to reduce wear and friction on sliding steel surfaces*, Carbon **54**, 454 (2013).

[223] G. Amontons, *De la rsistance cause'e dans les machines*, Memoires de l'Acadmie des Sciences **1706**, 257 (1699).

[224] H. R. Hertz, *Ueber die Beruehrung elastischer Koerper (On Contact Between Elastic Bodies)*, Gesammelte Werke (Collected Works) **1**, 1895 (1882).

[225] J. F. Archard, *Elastic Deformation and the Laws of Friction*, Proceedings of the Royal Society of London Series a-Mathematical and Physical Sciences **243**, 190 (1957).

[226] B. Bhushan, *Contact mechanics of rough surfaces in tribology: multiple asperity contact*, Tribology Letters **4**, 1 (1998).

[227] B. N. J. Persson, *Contact mechanics for randomly rough surfaces*, Surface Science Reports **61**, 201 (2006).

[228] , University of Oslo, 2001.

[229] J. N. Israelachvili and G. E. Adams, *Measurement of Forces between 2 Mica Surfaces in Aqueous-Electrolyte Solutions in Range 0-100 Nm*, Journal of the Chemical Society-Faraday Transactions I **74**, 975 (1978).

[230] R. G. Horn and J. N. Israelachvili, *Direct Measurement of Structural Forces between 2 Surfaces in a Non-Polar Liquid*, Journal of Chemical Physics **75**, 1400 (1981).

[231] J. N. Israelachvili and P. M. Mcguiggan, *Forces between Surfaces in Liquids*, Science **241**, 795 (1988).

[232] J. N. Israelachvili, *Intermolecular and Surface Forces* (Academic Press, London, 1991).

[233] A. Schob and F. Cichos, *A modified surface forces apparatus for single molecule tracking*, Journal of Physical Chemistry B **110**, 4354 (2006).

[234] M. Dienwiebel, N. Pradeep, G. S. Verhoeven, H. W. Zandbergen, and J. W. M. Frenken, *Model experiments of superlubricity of graphite*, Surface Science **576**, 197 (2005).

[235] K. B. Jinesh and J. W. M. Frenken, *Capillary condensation in atomic scale friction: How water acts like a glue*, Physical Review Letters **96**, (2006).

[236] S. Y. Krylov and J. W. M. Frenken, *Atomic-scale friction experiments reconsidered in the light of rapid contact dynamics*, Physical Review B **80**, (2009).

[237] R. W. Carpick and M. Salmeron, *Scratching the surface: Fundamental investigations of tribology with atomic force microscopy*, Chemical Reviews **97**, 1163 (1997).

[238] G. Binnig, C. Gerber, E. Stoll, T. R. Albrecht, and C. F. Quate, *Atomic Resolution with Atomic Force Microscope*, Surface Science **189**, 1 (1987).

[239] P. Stempfle, O. Pantale, T. Djilali, R. K. Njiwa, X. Bourrat, and J. Takadoum, *Evaluation of the real contact area in three-body dry friction by micro-thermal analysis*, Tribology International **43**, 1794 (2010).

[240] D. Keller, *Reconstruction of Stm and Afm Images Distorted by Finite-Size Tips*, Surface Science **253**, 353 (1991).

[241] S. Y. Krylov, J. A. Dijksman, W. A. van Loo, and J. W. M. Frenken, *Stick-slip motion in spite of a slippery contact: Do we get what we see in atomic friction?*, Physical Review Letters **97**, (2006).

[242] C. W. Mccutchen, *Optical Systems for Observing Surface Topography by Frustrated Total Internal Reflection + by Interference*, Review of Scientific Instruments **35**, 1340 (1964).

[243] Y. Golan, N. A. Alcantar, T. L. Kuhl, and J. Israelachvili, *Generic substrate for the surface forces apparatus: Deposition and characterization of silicon nitride surfaces*, Langmuir **16**, 6955 (2000).

[244] L. Novotny and B. Hecht, *Principles of Nano-Optics* (Cambridge University Press, New York, 2006).

[245] X. Ben and H. S. Park, *Size Dependence of the Plasmon Ruler Equation for Two-Dimensional Metal Nanosphere Arrays*, Journal of Physical Chemistry C **115**, 15915 (2011).

[246] A. D. McFarland and R. P. Van Duyne, *Single silver nanoparticles as real-time optical sensors with zeptomole sensitivity*, Nano Letters **3**, 1057 (2003).

[247] A. J. Haes, S. L. Zou, G. C. Schatz, and R. P. Van Duyne, *Nanoscale optical biosensor: Short range distance dependence of the localized surface plasmon resonance of noble metal nanoparticles*, Journal of Physical Chemistry B **108**, 6961 (2004).

[248] I. Ament, J. Prasad, A. Henkel, S. Schmachtel, and C. Sonnichsen, *Single Unlabeled Protein Detection on Individual Plasmonic Nanoparticles*, Nano Letters **12**, 1092 (2012).

[249] P. Mulvaney, J. Perez-Juste, M. Giersig, L. M. Liz-Marzan, and C. Pecharroman, *Drastic surface plasmon mode shifts in gold nanorods due to electron charging*, Plasmonics **1**, 61 (2006).

[250] U. Hakanson, M. Agio, S. Kuhn, L. Rogobete, T. Kalkbrenner, and V. Sandoghdar, *Coupling of plasmonic nanoparticles to their environments in the context of van der Waals-Casimir interactions*, Physical Review B **77**, (2008).

[251] A. Grubisic, V. Schweikhard, T. A. Baker, and D. J. Nesbitt, *Coherent Multiphoton Photoelectron Emission from Single Au Nanorods: The Critical Role of Plasmonic Electric Near-Field Enhancement*, ACS Nano **7**, 87 (2013).

[252] B. Bhushan, *Adhesion and stiction: Mechanisms, measurement techniques, and methods for reduction*, Journal of Vacuum Science and Technology B **21**, 2262 (2003).

[253] B. C. Buchler, T. Kalkbrenner, C. Hettich, and V. Sandoghdar, *Measuring the quantum efficiency of the optical emission of single radiating dipoles using a scanning mirror*, Physical Review Letters **95**, (2005).

[254] K. H. Drexhage, *Influence of a Dielectric Interface on Fluorescence Decay Time*, Journal of Luminescence **1-2**, 693 (1970).

[255] H. Morawitz, *Self-Coupling of a Two-Level System by a Mirror*, Physical Review **187**, 1792 (1969).

[256] W. Lukosz and R. E. Kunz, *Light-Emission by Magnetic and Electric Dipoles Close to a Plane Interface.1. Total Radiated Power*, Journal of the Optical Society of America **67**, 1607 (1977).

[257] S. Marras, *Selection of fluorophore and quencher pairs for fluorescent nucleic acid hybridization probes, in Methods in Molecular Biology: fluorescent energy transfer nucleic acid probes: designs and protocols* (Humana Press Inc., Totowa, New Jersey, 2006).

[258] B. Kizel, *Practical molecular spectroscopy* (MFTI Publ., Moscow, 1998).

[259] L. A. Brey, G. B. Schuster, and H. G. Drickamer, *High-Pressure Studies of Effect of Viscosity on Fluorescence Efficiency in Crystal Violet and Auramine O*, Journal of Chemical Physics **67**, 2648 (1977).

[260] H. Zollinger, *Color Chemistry: Syntheses, Properties and Applications of Organic Dyes and Pigments* (VCH Verlagsgesellschaft, Weinheim, Germany, 1987).

Summary

The optical properties of nano-objects depend on their structure and composition. Therefore, it is essential to characterize the optical properties of nano-objects to explore their use in scientific or technological applications. In this thesis, we study the absorption, luminescence, and scattering of individual nano-objects including single molecules, organic dye nanoparticles and gold nanoparticles. We combine photothermal (absorption), luminescence, and scattering signals on a single-particle basis to gain fundamental insight into the radiative and nonradiative properties of the nano-objects.

In chapter 1, we present a brief overview of a variety of nano-objects, discussing their properties and giving some examples of their fundamental and technological applications. We also shortly introduce the optical methods to detect these nano-objects, discussing their advantages and disadvantages.

In chapter 2, we describe the technique of photothermal microscopy by which we can detect single nano-objects by their absorption at room temperature. The nano-objects produce heat upon their excitation with an intensity-modulated laser light within their absorption band and a time-dependent thermal lens is created around the nano-object. The corresponding refractive-index profile, a nanolens, is detected with a second laser that is tuned outside the absorption band of the nano-object. We utilize different ways (e.g. index matching, using a liquid with high photothermal strength, careful compensation of chromatic aberrations, etc.) to optimize the detection sensitivity of this photothermal microscopy technique. We use single gold nanospheres as a reference to estimate the absolute absorption cross sections. These gold nanoparticles provide good photostability and do not show saturation effects. Using this method, we first show that our detection limit lies at 3 nW dissipated power (in an integration time of 10 ms), which is of the order of the power dissipated by a single molecule at saturation. Secondly, we demon-

strate the detection of individual nonfluorescent molecules by their absorption at room temperature. Our study over 30 individual chromophores yields an average absorption cross-section of 4 $Å^2$ per molecule. This value is in satisfactory agreement with the isotropic value, 2.1 $Å^2$, deduced from the absorption spectrum of the dye in glycerol. The room-temperature detection of a single molecule by its absorption has been a challenge since the first observation of a single molecule by its fluorescence.

Combining photothermal contrast with measurements by fluorescence microscopy allows us to gain insight into the luminescence properties of nanoparticles, i.e., we are able to calculate the absolute quantum yield of single nano-objects. In chapter 3, we study the luminescence properties of spherically shaped organic dye nanoparticles which are prepared by reprecipitation of a triarylamine dye solution in acetone in vigorously stirred water. These nanoparticles exhibit a complex excitation-power-dependent luminescence quantum yield due to singlet-singlet or singlet-triplet annihilation, and their luminescence quantum yield can be as high as 10^{-2}. We also count the number of molecules in a single dye nanoparticle using luminescence and absorption signals. We find that there are $10^4 - 10^5$ molecules in a dye nanoparticle with a diameter of about 60 nm. The results of correlated optical and scanning probe measurements (AFM) are in good agreement with each other showing the potential use of correlated measurement for study and characterization of complex systems. Another interesting property of these dye nanoparticles is that they can form net-shaped and labyrinth-shaped patterns which are probably induced by dewetting of the dye nanoparticle suspension on the substrate during sample preparation. The patterns fromed from nanoparticles can find applications, for instance, in organic thin film transistor or solar cells.

We studied the one-photon luminescence properties of gold nanoparticles in chapter 4 (spheres) and 5 (rods). In contrast to organic dye nanoparticles, gold nanoparticles yield very stable optical signals providing good photoluminescence contrast. In chapter 4, we studied the effect of the particle volume on their luminescence quantum yield. We present simultaneous detection of luminescence and photothermal (absorption) signals of individual gold nanospheres with diameters ranging from 5 to 80 nm. We also correlate the size of the same individual nanospheres measured independently by AFM with their optical signals. Our results confirm that absorption and lumi-

nescence signals scale with the volume of the nanosphere. Their photoluminescence quantum yield is nearly independent of size and is about 3×10^{-7}. Because the gold nanospheres can be imaged by conventional fluorescence microscopy with good signal-to-noise ratios, they can be applied to studies that require stable optical signals.

In chapter 5, we investigate the effect of the aspect ratio of single gold nanorods on their luminescence quantum yield. We find that the quantum yield of single gold nanorods can be as high as $\sim 10^{-5}$. Compared to single gold nanospheres, we observe an increase of quantum yield by about an order of magnitude for particles with a plasmon resonance wavelenghts longer than 650 nm. In order to gain insight into the mechanism of luminescence from gold nanoparticles, we correlated scattering and luminescence spectra of individual nanorods with different plasmon resonances and we performed polarization sensitive measurements. We find that there are two components which contribute to the luminescence spectrum, one around 500 nm and one coinciding with the longitudinal plasmon band. Our study contributes to the understanding of luminescence from gold nanorods for their applications in biological and soft matter studies.

The study of chapter 6 concerns novel optical methods to study contact mechanics at interfaces of materials over a large area (several 10 μm^2). In detail, we exploit the sensitivity of the plasmon resonance of a gold nanoparticle to the nearby presence of a dielectric. We study the effect of the substrate-nanorod distance on the plasmon resonance of a gold nanorod. We built a setup that allows bringing two substrates closer to each other in steps of a few nanometers. For distances less than 400 nm, we observe a significant redshift of the plasmon resonance wavelength of the nanorod while decreasing the distance between the nanorod and the substrate; the observed changes are reversible. Although preliminary, these results point the way towards applying single gold nanorods as a tool to measure distances between dielectric interfaces on a nanometer scale with good control and high resolution.

Samenvatting

De optische eigenschappen van nano-objecten hangt af van hun structuur en samenstelling. Daarom is het belangrijk om eerst de optische eigenschappen van nano-objecten te karakteriseren om daarmee hun wetenschappelijke en technologische toepassingen te verkennen. In dit proefschrift bestuderen we de absorptie, luminescentie en de verstrooiing van fotonen door individuele nano-objecten waaronder moleculen, nanodeeltjes met organische kleurstoffen, en gouden nanodeeltjes. We combineren de fotothermische (absorptie), luminescentie en verstrooiings signalen van individuele deeltjes om zo inzicht te krijgen in stralings- en niet-stralingsprocessen van deze nano-objecten.

In hoofdstuk 1 geven we een kort overzicht van verscheidene nano-objecten waarin we hun eigenschappen en enkele fundamentele en technologische toepassingen bespreken. Ook behandelen we kort de optische methodes om deze nano-objecten te detecteren. We bespreken de voor- en nadelen van deze methodes.

In hoofdstuk 2 beschrijven we de fotothermische microscopie waarmee we individuele nano-objecten kunnen detecteren door middel van hun absorptie bij kamertemperatuur. Als gevolg van de excitatie met in intensiteit gemoduleerd laserlicht binnen hun absorptie band produceren de nano-objecten warmte; dit resulteert in een tijdsafhankelijke thermische lens rondom het nano-object. Het bijbehorende brekingsindex profiel, een nanolens, wordt gedetecteerd met behulp van een tweede laser met een golflengte buiten de absorptie band van het nano-object. We optimaliseren de detectie gevoeligheid van de fotothermische microscopie op verschillende manieren (bijvoorbeeld door het matchen van de brekingsindex, het gebruik van vloeistoffen met hoge fotothermische sterkte, het zorgvuldig compenseren van chromatische aberraties, etc.). We gebruiken individuele

gouden nano-bolletjes als referentie voor het afschatten van de absolute absorptie doorsnede. Deze gouden nano-deeltjes hebben een uitstekende fotostabiliteit en vertonen geen verzadigings verschijnselen. Met behulp van deze methode laten we eerst zien dat onze detectie limiet bij een gedissipeerd vermogen van 3 nW ligt (met een integratie tijd van 10 ms). Deze waarde is van dezelfde orde van grootte als de dissipatie door een enkel molecuul bij verzadiging. Ten tweede laten we zien dat we individuele niet-fluorescerende moleculen aan de hand van hun absorptie bij kamertemperatuur kunnen detecteren. In een studie van 30 individuele chromoforen vinden we een gemiddelde absorptie doorsnede van 4 $Å^2$ per molecuul. Deze waarde is in redelijke overeenstemming met de isotrope waarde van 2.1 $Å^2$, zoals afgeleid uit het absorptiespectrum van de kleurstof in glycerol. De detectie van een individueel molecuul aan de hand van zijn absorptie bij kamertemperatuur is een uitdaging geweest vanaf de eerste waarneming van een individueel molecuul door middel van zijn fluorescentie.

Door fotothermische microscopie met fluorescentie microscopie te combineren zijn we in staat inzicht te krijgen in de luminescentie eigenschappen van nanodeeltjes, met andere woorden, we kunnen het absolute kwantum rendement van een enkel nanodeeltje bepalen. In hoofdstuk 3 bestuderen we de luminescentie eigenschappen van bolvormige nanodeeltjes met een organische kleurstof die worden bereid door middel van reprecipitatie in water van een oplossing van een triarylamine kleurstof in aceton, onder grondig roeren. Dankzij singlet-singlet annihilatie vertonen deze nanodeeltjes een complex excitatie-vermogen-afhankelijke luminescentie kwantum rendement, wat op kan lopen tot wel 10^{-2}. Aan de hand van luminescentie en absorptie signalen bepalen we bovendien het aantal moleculen in een nanodeeltje met organische kleurstof. We vinden zo'n $10^4 - 10^5$ moleculen in een nanodeeltje met een diameter van ongeveer 60 nm. De resultaten van gecorreleerde optische en tast microscopie (AFM) zijn in goede overeenstemming met elkaar, wat de potentiele toepassing van gecorreleerde metingen toont voor het bestuderen en karakteriseren van complexe systemen. Een andere interessante eigenschap van deze nanodeeltjes met organische kleurstof is dat ze netvormige en labyrintvormige patronen kunnen vormen door het opdrogen ("dewetting") van de suspensie met de nanodeeltjes met kleurstof, tijdens de sample preparatie. De patronen van nanodeeltjes zouden toepassingen kunnen vinden, bijvoorbeeld in organische film transistors of zonnecellen.

In hoofstuk 4 (bolletjes) en hoofstuk 5 (staafjes) hebben we de één-foton-luminescentie eigenschappen van gouden nanodeeltjes onderzocht. In tegenstelling tot de nanodeeltjes met organische kleurstof vertonen de gouden nanodeeltjes zeer stabiele optische signalen, wat een goed fotoluminescentie contrast oplevert. In hoofdstuk 4 hebben we het effect van het volume van de gouden nanodeeltjes op het kwantum rendement van de luminescentie onderzocht. We tonen resultaten van gelijktijdige detectie van luminescentie en fotothermische (absorptie) signalen afkomstig van individuele gouden nanobolletjes met diameters variërend van 5 tot 80 nm.

Bovendien correleren we de afmetingen van het nanodeeltje, die we onafhankelijke gemeten hebben met een tast microscoop (AFM), aan de corresponderende optische signalen. Onze resultaten bevestigen dat de absorptie en luminescentie signalen schalen met het volume van het nanobolletje. Het kwantum rendement van hun fotoluminescentie is vrijwel onafhankelijk van het volume en bedraagt ongeveer 3×10^{-7}. Omdat gouden nanobolletjes met goede signaal-ruis verhouding kunnen worden afgebeeld met conventionele fluorescentie microscopie kunnen ze worden gebruikt in studies die stabiele optische signalen vereisen.

In hoofdstuk 5 onderzoeken we het effect van de aspect ratio van een individueel gouden nanostaafje op het kwantum rendement van zijn fotoluminescentie. We vinden kwantum rendementen die op kunnen lopen tot $\sim 10^{-5}$. Vergeleken met individuele nanobolletjes observeren we een toename van het kwantum rendement met ongeveer een orde van grootte voor nanostaafjes met een plasmon resonantie bij golflengtes langer dan 650 nm. Om inzicht te krijgen in het mechanisme achter de luminescentie van gouden nanodeeltjes, hebben we verstrooiingsspectra gecorreleerd aan luminescentiespectra van individuele nanodeeltjes met verschillende plasmon resonanties en hebben we polarisatie gevoelige meetingen uitgevoerd. We vinden twee componenten die bijdragen aan het luminescentiespectrum: een component bij een golflengte van 500 nm en een component die samenvalt met de longitudinale plasmon band. Onze studie draagt bij aan het begrip van luminescentie van gouden nanostaafjes en hun toepassingen in biologische studies, en studies aan zachte gecondenseerde materie.

Hoofdstuk 6 behandelt nieuwe optische methodes om de mechanica van contacten tussen oppervlakken op grote schaal (enkele tientallen vierkante micrometers). In het bijzonder gebruiken we de gevoeligheid van de plas-

mon resonantie van een gouden nanodeeltje voor de aanwezigheid van diëlektrische media in de nabijheid. We bestuderen het effect van de afstand tussen het substraat en het nanostaafje op de plasmon resonantie van een gouden nanostaafje. We construeren een opstelling die ons in staat stelt twee substraten in stapjes van enkele nanometers bij elkaar te brengen. Voor afstanden kleiner dan 400 nm observeren we een significante roodverschuiving van de plasmon resonantie bij afnemende afstand tussen het substraat en het gouden nanostaafje. De waargenomen veranderingen in de verschuiving van de plasmon resonantie zijn omkeerbaar. Deze voorlopige resultaten wijzen op de toepassing van individuele gouden nanostaafjes als instrument voor het meten van afstanden tussen diëlektrische media op nanometer schaal met goede controle en hoge resolutie.

Curriculum vitae

Mustafa Yorulmaz

Aug 26, 1984	Born in Nevşehir, Turkey
1998-2002	Secondary school, Selçuklu Anadolu Lisesi, Konya, Turkey
2002-2007	B.Sc. Physics, Bilkent University, Ankara, Turkey
2007-2009	M.Sc. Materials Science and Engineering, Koç University, İstanbul, Turkey
	Thesis: Single molecule tracing in confined geometries
	Advisor: Assoc. Prof. dr. A. Kiraz
2009-2013	Ph.D. research at Leiden University, Leiden, the Netherlands
	Thesis: Absorption, luminescence and scattering of single nano-objects
	Advisor: Prof. dr. M. A. G. J. Orrit Teaching assistant in Physics Research laboratory course (Natuurkundig Onderzoek)
2013-2014	Postdoctoral Fellow at Leiden University
	Advisor: Prof. dr. M. A. G. J. Orrit
2014-	Postdoctoral Fellow at Rice University
	Advisor: Asst. Prof. dr. S. Link

List of publications

- H. Yuan, S. Khatua, P. Zijlstra, **M. Yorulmaz**, M. Orrit, *Thousand-fold enhancement of single-molecule fluorescence near a single gold nanorod*, Angew. Chem. Int. Ed. **52**, 1217-1221 (2013).

- **M. Yorulmaz**, S. Khatua, P. Zijlstra, A. Gaiduk and M. Orrit, *Luminescence quantum yield of single gold nanorods*, Nano Lett. **12**, 4385-4391 (2012).

- A. Gaiduk, **M. Yorulmaz**, E. Ishow and M. Orrit, *Absorption, luminescence, and sizing of organic dye nanoparticles and of patterns formed upon dewetting*, ChemPhysChem **13**, 946-951 (2012).

- A. Gaiduk, **M. Yorulmaz** and M. Orrit, *Correlated absorption and photoluminescence of single gold nanoparticles*, ChemPhysChem **12**, 1536-1541 (2011).

- A. Gaiduk, P. V. Ruijgrok, **M. Yorulmaz** and M. Orrit, *Making gold nanoparticles fluorescent for simultaneous absorption and fluorescence detection on the single particle level*, Phys. Chem. Chem. Phys. **13**, 149-153 (2011).

- A. Gaiduk, **M. Yorulmaz**, P. V. Ruijgrok, and M. Orrit, *Room-temperature detection of a single molecule's absorption by photothermal contrast*, Science **330**, 353-356 (2010).

- A. Gaiduk, P. V. Ruijgrok, **M. Yorulmaz** and M. Orrit, *Detection limits in photothermal microscopy*, Chemical Science **1**, 343-350 (2010).

- A. Kiraz, S. C. Yorulmaz, **M. Yorulmaz**, and A. Sennaroglu, *Raman lasing near 650 nm from pure water microdroplets on a superhydrophobic surface*, Photonics and Nanostructures - Fundamentals and Applications **7**, 186-189 (2009).

- **M. Yorulmaz**, A. Kiraz, A. L. Demirel, *Motion of Single Terrylene Molecules in Confined Channels of Poly(butadiene)-Poly(ethylene oxide) Diblock Copolymer*, The Journal of Physical Chemistry B **113**, 9640-9643 (2009).

Acknowledgements

During the four years of my PhD study, I got a lot of support from many people. I would like to express my appreciation and gratitude to everyone who made my thesis possible.

First of all, I would like to thank my supervisor Prof. Michel Orrit for giving me the chance to be a member of the MoNOS group, at Leiden University. I especially thank him for insightful scientific discussions and valuable advice. I greatly appreciate his support, encouragement and guidance throughout my PhD study.

I would like to thank my copromotor Dr. Alexander Gaiduk for everything he has taught me, for all his support from both professional and personal points of view. He had a significant impact on my academic career. A special word of thanks to Dr. Peter Zijlstra and Dr. Saumyakanti Khatua for their enthusiasm and help.

It was very special to have technical support from the mechanical and electronics workshops. I want to specially thank Harmen van der Meer, who was very patient, careful and helpful in making the home-built setups used in this thesis. I also want to thank Arno van Amersfoort and René Overgauw. They were always there when I needed help for any failure of the electronics. I want to thank Jos Disselhorst for his quick solutions to problems I had in the lab.

I want to thank Henriette van Leeuwen who was always very helpful with all the administrative work. I also want to thank her for helping me to find my first place to live in Leiden. I also want to thank Rowena van der Reijden and Margareth van Hoorn-v.d. Poel for their endless help with the paperwork related to residence permit.

I want to thank Pedro Navarro for all the nice discussions, which always sparkled. I am grateful to Nico Verhart for the Dutch translation of the sum-

mary. I want to thank Martin van Son for the good organization of the chemical room. I also want to thank Haifeng Yuan, Paul Ruijgrok, Huib Blok, Maryam Hashemi Shabestari for useful discussions. I wish to express my gratitude to all members of MoNOS group, and to all my friends and colleagues at Leiden University for providing a friendly work environment, and for their support during my research.

A special thanks to my family. I want to thank them all for their permanent love, great support and patience. Their confidence in me has encouraged me to continue my career in science. Many thanks equally go to my parents-in-law, for their understanding and support.

I wish to express my dearest thanks to my wife Çiğdem, who has given all her support and understanding. My biggest gratitude is to her. I would like to thank Çiğdem for her endless love, understanding, patience, and encouragement. Our sweet daughter, Elif Sena, the softest point in my heart, has brought much happiness and joy into my life. I would like to dedicate this thesis to Çiğdem, Elif Sena, and my family.